

INCORPORATION OF TIME IN DATA ANALYSIS FOR SURFACE MINERALOGICAL MAPPING WITH MULTISPECTRAL REMOTE SENSING

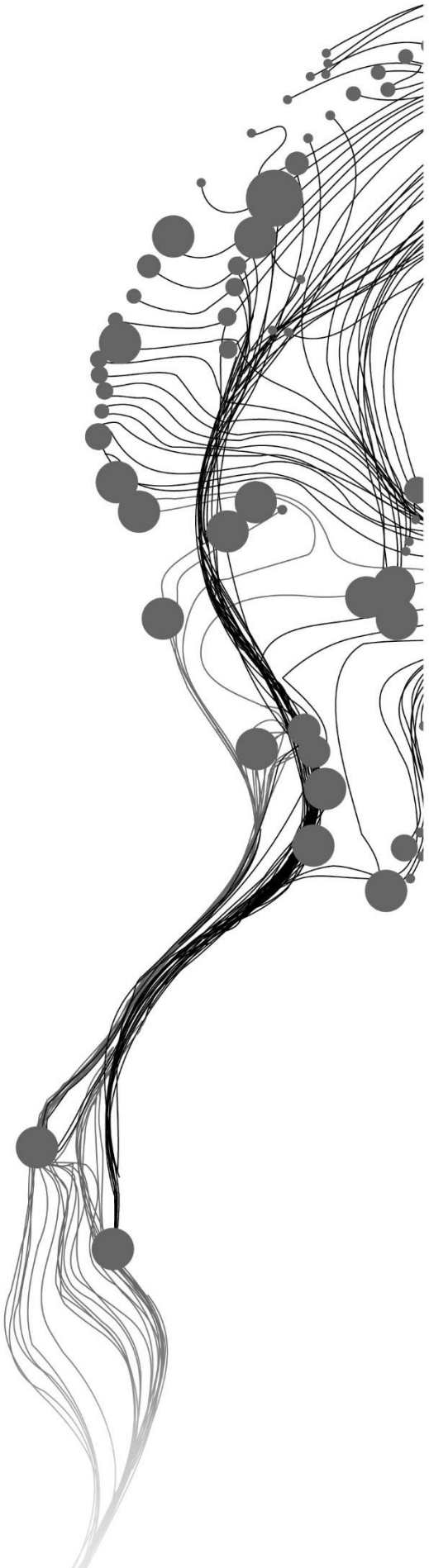
AKHIL SAMPATIRAO

July 2020

SUPERVISORS:

Dr. H.M.A van der Werff, ITC ESA

Dr. Ir. Janneke Ettema, ITC ESA



INCORPORATION OF TIME IN DATA ANALYSIS FOR SURFACE MINERALOGICAL MAPPING WITH MULTISPECTRAL REMOTE SENSING

AKHIL SAMPATIRAO

Enschede, The Netherlands,

June 2020

Thesis submitted to the Faculty of Geo-Information Science and Earth Observation of the University of Twente in partial fulfilment of the requirements for the degree of Master of Science in Geo-information Science and Earth Observation.

Specialization: Applied Remote Sensing for Earth Sciences

SUPERVISORS:

Dr. H.M.A van der Werff, ITC ESA

Dr. Ir. Janneke Ettema, ITC ESA

THESIS ASSESSMENT BOARD:

Prof. Victor Jetten (Chair)

Dr. Mike Buxton (External Examiner, Technical University of Delft)

DISCLAIMER

This document describes work undertaken as part of a programme of study at the Faculty of Geo-Information Science and Earth Observation of the University of Twente. All views and opinions expressed therein remain the sole responsibility of the author, and do not necessarily represent those of the Faculty.

ABSTRACT

Geological time is very different from the general time; changes in geology do not happen in a month or a year, unlike its surroundings. As a result, the applications of multi-temporal remote sensing in mineralogical mapping are minimal. Although geology does not change in short periods, its surroundings – vegetation cover, atmospheric and illumination conditions change rapidly with time. With these changes in surroundings happening, the question ‘Do remotely obtained spectra of geological objects – rocks, outcrops, soil surfaces, etc. change with time?’ raises.

Vegetation cover is considered one of the toughest challenges in Geological Remote Sensing (GRS), which is also the reason for most GRS studies to take place in desert-like areas. In most GRS studies, pixels rich in vegetation are masked out. Techniques such as spectral unmixing, principal component analysis, regression models, etc. were developed over the years to tackle the influence of vegetation cover on spectral signatures of geological objects. This research attempts to take on the challenge of vegetation cover by incorporating the paradigm of time.

The abilities of time in tackling vegetation cover in geological remote sensing using multi-temporal Sentinel-2 imagery are evaluated in this research. Changes in remotely sensed spectra of geological objects due to natural vegetation over a period of thirteen months were observed to understand the level of information that can be retrieved from pixels with mixtures of vegetation and geological objects. Forty Sentinel 2 level 2A images over Rodalquilar, southeast Spain, were analyzed using Google Earth Engine; pixels were selected for tracing changes over time, and classified into ‘pure geology,’ ‘mixed,’ and ‘vegetation’ pixels. Time-series analysis was then performed on spectra, band ratios, and reflectance values of individual bands of all the selected pixels.

Results from this research show that spectra of geological objects change with time; both pure geology and mixed pixels showed variations over time. Seasonal differences were observed in spectra and band ratios of mixed pixels; the trends were similar to that of the variation of vegetation in the region. Time helped in differentiating between signal due to different parts (vegetation, geology) in mixed pixels. Several possibilities of misinterpretations in the traditional GRS approach were observed. This research demonstrated the advantages of using multi-temporal remote sensing applications in surface mineralogical mapping and contributes to understanding the variations in remotely sensed spectra of geological objects over time.

ACKNOWLEDGEMENTS

I thank my supervisors, **Dr. Harald van der Werff**, and **Dr. Ir. Janneke Ettema**, for their guidance, suggestions, support throughout this research, and above all, this exciting topic. It has been a pleasure working under their supervision, and I've thoroughly enjoyed discussing this interesting research with them. I would especially like to thank my first supervisor, Harald, for mentoring me throughout my MSc. His willingness to help in every moment came of great help throughout my coursework.

I would also like to thank all my classmates (ARS 2018-2020) for intriguing discussions, group projects, and support throughout, especially Bruno, Lawrence, and Tadele, for taking out time and helping me deal with my lack of a geology background.

Special mentions to Student Affairs – ITC, SAB – ITC, for making my stay in the Netherlands better and comfortable. I would also like to thank my friends in the Netherlands, the Geomatter clan, for their enormous support and travel stories. Special thanks to all my coffee break friends; many discussions helped me shape my research in the initial stages, especially Bhargava and Manushi. Living in the Netherlands, far away from family and friends would not be the same without Sarah Ravenhorst, I express my sincere and heartfelt gratitude for her support and company. I would also like to thank all my friends back in India, especially Rajitha and Aditya, for being just a call away.

Lastly, if it weren't for my parents and family members, this would not be possible. I thank all my family members for their enormous support, guidance, and unconditional love.

TABLE OF CONTENTS

Abstract	5
Acknowledgements	6
List of figures	9
List of tables	11
1. Introduction	13
1.1. Research Problem	13
1.2. Research Objectives	15
1.2.1. Specific Objectives & Research Questions	15
1.3. Research Approach	16
1.4. Spectral Misbehavior	16
1.5. Study Area	17
1.5.1. Geological Significance	17
1.5.2. Vegetation	18
1.5.3. Climate	18
1.6. Related Work	19
2. Methodology	22
2.1. Processing Platform	22
2.2. Data	22
2.3. Image Selection	23
2.4. Data Preparation	23
2.5. Band Ratios	24
2.6. Analysis Tools	25
2.7. Pixel Selection	25
2.7.1. Vegetation Pixels	26
2.7.2. Geology Pixels	26
2.7.3. Pixel Definition	27
3. Results	28
3.1. Pixel Selection	28
3.2. Time Series	32
3.2.1. Time Series on Spectra	33
3.2.2. Time Series on Band Ratios	36
3.2.3. Time Series on individual bands	40
3.3. Influence of Shadow and Clouds	42
3.3.1. Shadow	42
3.3.2. Cloud cover	43
4. Discussion	45
5. Conclusions and recommendations	49
5.1. Recommendations	50
6. List of references	52
7. Appendix	56
7.1. Dataset	56
7.2. Pixel Selection	57
7.3. Time Series	60
7.4. Scripts	64
7.4.1. Image filtering & Selection	64
7.4.2. Extracting Spectra	65

7.4.3. Band ratios and band ratio statistics 66
7.4.4. Band ratio time-series charts 68
7.4.5. Time-lapse visualizations 69
7.4.6. 3-D Spectra 70

LIST OF FIGURES

Figure 1.1: True colour composite of Sentinel-2A MSI bands 4 (in red), 3 (in green), and 2 (in blue). The image is a subset of the study area around the mining town of Rodalquilar, Cabo de Gata, Spain..... 11

Figure 1.2: Vegetation in the study area; A is a Google Earth Image showing vegetation, B is a photograph from previous fieldwork (from ITC ESA’s archives), C, D, and, E are Google Street View images..... 18

Figure 1.3: Variations of maximum, minimum and average temperatures (left) and average rainfall amount and rainy days (right) throughout the year, 2019 (World Weather Online, 2020). 18

Figure 3.1: Shortlisted Regions after visually inspecting the study area. The image is a true color composite (bands B4 in red, B3 in green, and 2 in blue) from January 1, 2019. 18

Figure 3.2: Chart showing NDVI time series of the reference pixels. Blue (with diamonds as datapoints) being from a vegetation pixel, orange (with squares as datapoints) being from a pure geology pixel, and black (with triangles as datapoints) being from a mixed pixel. 183

Figure 3.3: NDVI time series curves for geo pixels 1 (top) and 14 (bottom) along with the reference pixels. The charts show a comparison with the time series of the reference pixels..... 18

Figure 3.4: Comparison of depth of absorption features from the vegetation and geology parts of the pixel. Blue (with diamonds as datapoints) curve shows the depth of feature due to vegetation and orange (with circles as datapoints) shows the depth of feature due to the geology part in the pixel..... 18

Figure 3.5: Spectral reflectance curves of vegetation 1 pixel from different months. A shows the spectra from spring, summer and autumn months (March to September 2019), B shows spectra from winter months, C and D are comparison of summer and winter spectra..... 18

Figure 3.6: Spectral reflectance curves of pure geology pixel 1 from different months. A shows the spectra from spring, summer and autumn months (March to September 2019), B shows spectra from winter months. C shows variations in spectra within one month (January 2019) and D shows one spectra each from all thirteen months..... 18

Figure 3.7: Spectral reflectance curves of mixed pixel 3 from different months. A shows the spectra from summer (April to July 2019), B shows spectra from winter months and C shows variations in spectra in the other months. D shows one spectra each from all thirteen months..... 18

Figure 3.8: Spectral reflectance curves of mixed pixel 1 from different months. A shows the spectra from summer (April to July 2019), B shows spectra from winter months and C shows spectra from the other months. D shows one spectra each from all thirteen months. 18

Figure 3.9: Band ratio time series of vegetation pixels for and extended dataset (Images from January 2018 to January 2020 were used). Blue curves (with diamonds as datapoints) shows the variation of band ratio values of vegetation pixel 1 and orange curves (with squares as data points) shows the variation of NDVI values of vegetation pixel 2. A shows NDVI time series, B shows SAVI time series, and C shows BR5 time series. 18

Figure 3.10: Time Series of band ratios from January 2019 to January 2020 (Day 1 to Day 391) of pure geology pixel 1. Blue curve (with diamonds as datapoints is time series of BR3 and orange curve (with squares as datapoints) is time series of BR5. BR value stands for band ratio value and x-axis is day number (0-391)..... 32

Figure 3.11: Time Series of band ratios from January 2019 to January 2020 (Day 1 to Day 391) of mixed pixel 3. Blue curve (with diamonds as datapoints is time series of BR3 and orange curve (with squares as datapoints) is time series of BR5. BR value stands of band ratio value and x-axis is day number (0-391).. 33

Figure 3.12: Time Series of band ratios from January 2019 to January 2020 (Day 1 to Day 391) of mixed pixel 1. Blue curve (with diamonds as datapoints is time series of BR3 and orange curve (with squares as datapoints) is time series of BR5. BR value stands of band ratio value and x-axis is day number (0-391).. 33

Figure 3.13: Time Series of band ratios from January 2019 to January 2020 (Day 1 to Day 391) of mixed pixel 2. Blue curve (with diamonds as datapoints is time series of BR3 and orange curve (with squares as datapoints) is time series of BR4. BR value stands of band ratio value and x-axis is day number (0-391).. 34

Figure 3.14: Variation of Bottom of Atmosphere Reflectance values of vegetation pixel 1 (A), pure geology pixel 1 (B), and mixed pixel 3 (C) from bands 5, 6, 7, 8 and 8A. All 40 images were used. Outliers (peaks & troughs) are due to cloudy images (February 20th, 2019 – day 51, June25th 2019 – day 176, and, January 1st, 2020 – day 366)..... 35

Figure 3.15: Image showing the location of geo pixel 21 in the study area. The highlighted area is a calcite mountain with shadows in the winter months. Yellow pointer shows the location of the pixel. Image is a false color composite from January 1st, 2019..... 36

Figure 3.16: False color composite visualizations of the calcite mountain with varying shadows. Yellow pointer shows the location of Geo Pixel 21. A is from January 11, 2019; B is from March 17, 2019; C is from October 13, 2019; D is from November 7, 2019..... 36

Figure 3.17: Variation in Spectra of Geo Pixel 21 due to shadows. Image shows low reflectance values in months with shadows. 37

Figure 3.18: Variation in spectra of geo pixel 3 due to cloud cover. Geo Pixel 3 is a pure geology pixel. The pixel was covered in shadow due to cloud. Spectra from all seasons were included for comparison. January 1st, 2020 (image number 366) image contained cloud cover. The spectra from January 1st, 2020 can be seen at the bottom..... 38

Figure3.19: Variation in spectra of geo pixel 4 due to cloud cover. Geo Pixel 4 is a mixed pixel. The pixel was covered in cloud cover. Spectra from all seasons were included for comparison. January 1st, 2020(image number 366) image contained cloud cover. The spectra from January 1st, 2020 can be seen at the top.... 38

Figure 4.1: Comparison of variation of absorption depth feature at 835 nm (BR3) for mixed pixel 1 (orange curve with circles as datapoints) and mixed pixel 3 (blue curve with diamonds as datapoints). 41

Figure 7.1: NDVI time series charts of the selected pixels along with the reference pixels. The charts show a comparison with the time series of the reference pixels. The orange curve (with data points as squares)

show the variation of NDVI for a pure geological pixel and the grey curve (with triangles as data points) show the variations of NDVI for a mixed pixel..... 53

Figure 7.2: NDVI time series charts of the selected pixels along with the reference pixels (continued). The charts show a comparison with the time series of the reference pixels. The orange curve (with data points as squares) show the variation of NDVI for a pure geological pixel and the grey curve (with triangles as data points) show the variations of NDVI for a mixed pixel. 54

Figure 7.3: Time Series of band ratios from January 2019 to January 2020 (Day 1 to Day 391) of geo pixel 3. BR3 (B7/B8) shows the variation of the absorption feature at 835nm (see figure 11) and BR5 (B8/B4) shows the variation of vegetation in the pixel. Blue curve (with diamonds as datapoints) is time series of BR3 and orange curve (with squares as datapoints) is time series of BR5. BR value stands of band ratio value.. 55

Figure 7.4: Variation of Bottom of Atmosphere Reflectance values of vegetation pixel 3 from bands 5, 6, 7, 8 and 8A. All 40 images were used. Outliers (some of the troughs) are due to cloudy images (February 20th, 2019–day 51, June 25th 2019 –day 176, and, January 1st, 2020–day 366).. 55

Figure 7.5: Spectra extracted from geo pixel 18. Orange and red (top two) are from summer months while blue, violet and black (bottom three) are from winter months. All images were cloud free..... 56

Figure 7.7: Time Series comparison of band 7 reflectance values for pure geology (geo pixel 3), mixed (geo pixel 7) and vegetation pixels. Blue curve (with diamonds as datapoints) is the variation of B7 reflectance values of the pure geology pixel, orange curve (with squares as datapoints) is for the mixed pixel, and silver curve (with triangles as datapoints) is for vegetation pixel. Outlier due to cloud cover was removed (day 366, January 1st, 2020) to compare the trends. 57

Figure 7.8: Time series of spectra from Geo Pixel 7. A representative spectra was chosen from each month from January 2019 to January 2020. All images were cloud free. 57

Figure 7.9: Time Series of band ratios from January 2019 to January 2020 (Day 1 to Day 391) of geo pixel 7. BR3 (B7/B8) shows the variation of the absorption feature at 835nm (see figure 13) and BR4 (B8/B8A) shows the variation of the absorption feature at 864nm..... 58

LIST OF TABLES

Table 1.1: List of relevant literature with their focus and findings.	15
Table 2.1: Characteristics of Sentinel – 2 MSI. Sentinel-2 MSI has 13 spectral bands ranging from VNIR to SWIR with varying spatial resolution from 10 to 60 meters (Huang et al., 2020; Nasuti & Carriero, 2015).	16
Table 2.2: List of band ratios used in the research with their modified formulae and output resolutions..	18
Table 2.3: List of target ranges of annual band ratio statistical values used to select geology pixels..	20
Table 3.1: List showing reference pixels and their locations. Pure Geology Pixel and Mixed Pixel were picked from one of the outcrops (region C in figure 1), and Vegetation pixel was chosen from the vegetated mountains (region A in figure 1)..	23
Table 3.2: The result of pixel definition along with each pixel's NDVI time series' second-degree trend equation. R is the rate of change of the curve's slope. R*10E7 was used as a coefficient to compare the curves. The sixth column (in italics) is the final classification of the pixels with ten pure and ten mixed pixels..	25
Table 3.3: List of pixels for which the time series results are shown in this section with their classes.	26
Table 7.1: Image Collection used in this research. Dates and Image ids of images used in this research. ..	51
Table 7.2: List of all the selected pixels with the annual band ratio statistical values..	58

1. INTRODUCTION

1.1. Research Problem

The search for mineral deposits has been a constant pursuit, right from the early civilizations. The growing population resulted in the increasing use of mineral resources over time. As these resources were essential for industrialization, the exploitable mineral resources turned into a significant metric in determining the economic prosperity of any region (Bhan & Krishnanunni, 1983). Mineral exploration methods have been ceaselessly developing with the advancement in science and technology. With scientific and technological progress in Surveying, Remote Sensing, and Geophysics, Geological mapping methods have evolved over the years. Remote Sensing has always played a crucial role in understanding geological & geomorphological correlations and patterns both at regional and global scales since its birth in the 19th century. Satellite and aerial imagery's unique perspective helps in understanding Earth's complex geological structures on a large scale (Oikonomidis & Mouratidis, 2009). The capabilities of Remote Sensing in geology has already been thoroughly discussed in various publications (Li et al., 2018; Al-Nahmi et al., 2017; Choi et al., 2017; van der Werff & van der Meer, 2015; Rowan et al., 2005, among others).

NASA launching Landsat-1 (named initially as ERTS-1 but later renamed as LANDSAT-1) in 1972 led to the initiation of Geological Remote Sensing (Porwal & González-Álvarez, 2019). Following the launch of Landsat-1, several other satellite missions took place. However, the Advanced Space-borne Thermal Emittance and Reflection Radiometer (ASTER) and hyperspectral Hyperion played a significant role in Geological Remote Sensing (Pearlman et al., 2003; Abrams, 2000; Abrams & Hook, 1998). Multispectral satellite imagery (especially ASTER and Landsat) combined with airborne hyperspectral imagery has always been used in Geological studies to map lithologies, surface mineralogy, and structures for over a decade now (van der Meer et al., 2014). However, with the failure of the ASTER – SWIR detector in 2008, ASTER's capabilities have been reduced substantially. Following this, the use of Sentinel-2 MSI in geological studies started increasing (Ge et al., 2018; van der Werff & van der Meer, 2015; van der Meer et al., 2014; Berger et al., 2012). With 13 bands in the visible and near-infrared (VNIR) to shortwave infrared (SWIR) range, the Sentinel-2 MSI provides data continuity of multispectral observations (specifically Landsat & SPOT) (Meyer et al., 2019; van der Werff & van der Meer, 2016). Also, Sentinel -2 having a high revisit time of 5 to 10 days (Nasuti & Carriero, 2015), unlike its predecessors, brings in a new perspective altogether in Geological Remote Sensing by allowing us to look in time (van der Werff et al., 2018a).

Despite the proven worth of satellite and aerial photography in geology, various factors limit the accuracy (Gupta, 2017). Atmospheric changes, vegetation, moisture, solar illumination, cloud cover, sun angle, time of acquisition, and path radiance are some factors affecting the quality of interpretations and thus make them inconclusive (Gupta, 2017). Atmospheric corrections deal with atmospheric scattering, haze, sun angle, and elevation to an extent (Moik, 1980). However, vegetation is one parameter that is neglected most of the time. Other than rocks lacking spectrally distinctive features, vegetation can be ranked as the most significant factor limiting the mapping abilities of Remote Sensing instruments applied to map geology (Carranza & Hale, 2002; Fraser & Green, 1987). Vegetation cover affects the mapping capabilities of lithologies using satellite and airborne instruments as vegetation obscures the spectral signatures of the underlying geological objects (Grebby et al., 2014). According to previous studies, it is reported that even 10 percent of green vegetation can obscure weak mineral absorption features in the shortwave infrared (Grebby et al., 2014; Crippen & Blom, 2001; Bierwirth et al., 1990; Ager & Milton, 1987; Siegal & Goetz, 1977). As a result, in most cases, geological remote sensing studies are carried out in desert-like arid areas with very sparse or no vegetation due to large-scale surface exposure of rock types (Grebby et al., 2014). Although vegetation, illumination conditions, atmospheric conditions, moisture content change rapidly with seasons, geology is one thing that does not change so quickly (in consideration with the geological time scale, Smith et al.,

(2007)). Geological Remote Sensing techniques are based on spectral data acquired from the sensors. This data is registered as energy reflected or emitted from the Earth's surface. The energy needs to be reflected or emitted from the objects of interest, i.e., rocks, sediments, outcrops, and soil (Gupta, 2017). Geological objects get outgrown by natural vegetation over time, which changes with seasons, and atmospheric conditions. These changes in natural vegetation result in continuously varying mixed spectral signatures. This variation in spectral characteristics makes it almost impossible for researchers to map geological features without the accuracy being affected (Grebby et al., 2014; Crippen & Blom, 2001; Bierwirth, 1990).

Image processing methods to enhance the manifestations of mineralized rocks and soils using reflectance spectra have been ineffective under conditions where there is vegetation. The traditional way of addressing this problem is to choose appropriate thresholds for the various predefined indices such as the Normalized Difference Vegetation Index (NDVI) or the Soil Adjusted Vegetation Index (SAVI) or the Enhanced Vegetation Index (EVI). For pixels rich in vegetation, these indices will be much higher than for pixels rich in rock. This method can be used to mask out vegetation. Although this is one of the widely used ways, the effects of dead plants cannot be dealt with using this approach as their spectra lack the red edge feature (Murphy & Wadge, 1994). Also, masking out pixels will result in loss of information as some of the mixed pixels (dominated by vegetation) might also be masked out. Various methods based on Principal Component Analysis, Spectral Unmixing, and use of linear regression models have been developed over the years to overcome the effect of vegetation on spectral signatures of the underlying lithological substrates (Haest et al., 2013; Rodger & Cudahy, 2009; Crippen & Blom, 2001; Bierwirth, 1990; Fraser & Green, 1987). Although a lot of research (mentioned above) has been carried out on overcoming the effects of vegetation, not a lot of attention has been paid on the variation of spectral signatures over a period of time due to vegetation.

Geological objects such as rocks, and mineral assemblages, not changing with time (in consideration with the geological time scale) but, their spectral signatures undergoing variations over time is the main idea behind this research. Incorporating the paradigm of time into the spectral analysis of known geological objects might help in identifying and understanding the parts of spectra, which are changing with time. Therefore this research is to observe and study the changes in the remotely sensed spectra of known geological objects caused by natural vegetation over a long period to understand the level of information that can be retrieved from the changing spectral signatures of the not so changing geologic objects.

1.2. Research Objectives

The objective of this research is to assess the viability of using the paradigm of time in the analysis of remotely sensed spectra for exploring the impact of natural vegetation cover on surface mineralogical mapping abilities using Sentinel-2 imagery.

1.2.1. Specific Objectives & Research Questions

- To understand the temporal behavior of spectra of rocks, mineral outcrops, and different types of natural vegetation species obtained from Sentinel 2 imagery.
 - ❖ What effect does changes in seasonality and growth cycle cause on spectral signatures of natural vegetation over time?
 - ❖ Do spectra of geological objects get affected over time? If yes, how and how much do they get affected?
 - ❖ How to optimally select or classify ground cover such that there are either pure or mixed pixels by using spectral indices?
- To identify the influence of natural vegetation on spectra of rocks, or mineral outcrops, obtained from Sentinel 2 imagery.
 - ❖ How do changes in natural vegetation spectra due to changes in seasonality and growth cycle relate to spectral changes of geological objects over time?
 - ❖ Is it possible to identify the parts of spectral signatures resulting from the geological objects that are not changing so quickly in comparison with natural vegetation?
- To suggest appropriate times of the year when the impact of vegetation on surface mineralogical mapping capabilities would be the least.
 - ❖ Can image spectra be used as a metric for image selection in surface mineralogical mapping applications?
 - ❖ How can existing satellite image selection methods for surface mineralogical mapping be improved?

1.3. Research Approach

The Classical Geological Remote Sensing (GRS) approach involves the use of image processing, spectral, and data analysis techniques on multispectral and hyperspectral imagery. Band ratioing techniques, decorrelation stretching, saturation enhancement, principal component analysis (PCA), spectral matching, and unmixing techniques are some of the commonly used methods (van der Meer et al., 2012). Spectroscopic measurements in the laboratory or spectral imageries are used to obtain spectral signatures for the lithologies. Straightforwardly coordinating image pixel spectra to the reflectance spectra of outcropping lithologies using automated image classification algorithms is one of the standard ways to deal with performing the rapid geological mapping (Rowan et al., 2005).

It takes thousands of years for changes in geology to happen (Smith et al., 2007). Unlike, vegetation, atmospheric conditions, and water, geology does not change with seasons. Therefore, multi-temporal Remote Sensing (RS) is not conventional in most GRS studies. However, some studies used multiple images to tackle cloud cover and atmospheric variations. For example, Hewson and Cudahy (2011), in their research, used eight multi-temporal ASTER images to examine the influence of the atmosphere and illumination conditions on geology products (Hewson & Cudahy, 2011). Their study was carried out over the Mt. Fitton area and indicates that solar elevation has a more significant impact than a tilt angle.

This research approaches vegetation cover, one of the most common problems in GRS (Grebby et al., 2014) by looking in time. Combining the concept of Multi-temporal Remote Sensing with techniques used in Classical GRS allows assessing vegetation's influence on remotely sensed spectral measurements. The focus of this research is to understand how the spectra of geology objects (mineral assemblages, outcrops, or soil) vary over time.

1.4. Spectral Misbehavior

Most study areas of GRS studies have complex topographies, both natural and humanmade (due to mining activities). With such topographies, there is a high possibility of small shadows, which result in a steep decrease in reflectance values. Also, when mining activities take place, there are chances for artificial objects to be sensed, which also affect the reflectance values. These reflectance values might, in turn, result in high band ratio values causing false positives.

The presence of an atmosphere is a significant issue in optical remote sensing as the electro-magnetic radiation has to pass through the atmosphere. The atmosphere influences the radiation from the ground to the sensor (Moik, 1980). Atmospheric correction algorithms are often used on remotely sensed imagery to deal with atmospheric haze, scattering, sun angle, and elevation (Moik, 1980). The performance of these atmospheric corrections depends both on the sensor and the method used. There are possibilities of the atmospheric correction failing, which influence the reflectance values and resulting in misinterpretations.

The presence of clouds, shadows, elevation differences, human activities, and inaccuracies in atmospheric correction methods cause spectral misbehavior. This abnormal behavior (reflectance values) might result in misinterpretations. Most of the factors causing such spectral misbehavior in pixels are dynamic. Therefore, by adding the dimension of time in the analysis, these mishaps could be avoided as such misbehavior does not occur at the same pixel in more than one image.

1.5. Study Area

The study area of this research is Rodalquilar, Cabo de Gata, Southeast Spain, located around 50km east of Almeria in Spain. The region famous for its gold mines is now a part of Cabo de Gata natural reserve. Mining in the Rodalquilar area started in the early 1800s and continued until 1966 (Arribas et al., 1995). Since the closure of the mines in 1966, the pits have been abandoned. Restoration of the natural landscape is being stimulated as the surrounding area - Cabo de Gata national park is now a protected area. The area covers geologically varied terrain, with marine limestones, hills, and slopes formed by profoundly altered volcanic tuffs containing sulfates and iron oxides and alluvial planes (van der Werff & van der Meer, 2016). Figure 1.1, a true color composite of Sentinel 2, shows the study area.

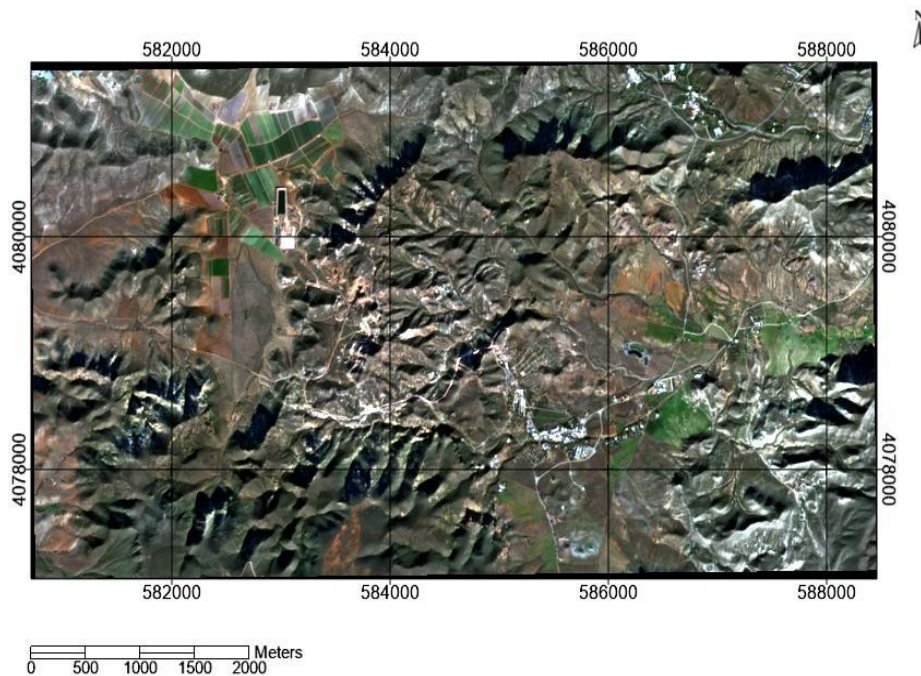


Figure 1.1: True colour composite of Sentinel-2A MSI bands 4 (in red), 3 (in green) and 2 (in blue). The image is a subset of the study area around the mining town of Rodalquilar, Cabo de Gata, Spain.

1.5.1. Geological Significance

Rodalquilar is a semi-arid region famous for its epithermal gold deposit (Rytuba, Arribas Jr., et al., 1990). This deposit is claimed to be Europe's first documented example of 'caldera-related epithermal Au mineralization' (Arribas et al., 1995). The geology, mineralization, and alteration in the area have been studied and well documented over the years (Arribas Cunningham, C. G., Rytuba, J. J., Rye, R. O., Kelly, W. C., Podwysoccki, M. H., McKee, E. H., Tosdal, 1995; Rytuba, Arribas, et al., 1990). Spectrally diagnostic minerals such as alunite, jarosite, calcite, and iron oxides are well exposed in this region, and several remote sensing studies were carried out in this area (Bedini, van der Meer, & van Ruitenbeek, 2009; van der Meer et al., 2014; van der Meer et al., 2012; van der Werff & van der Meer, 2016; amongst others).

This region was chosen as the study area of this research as 1) this area hosts spectrally distinctive minerals in the Sentinel – 2 wavelength regions; 2) availability of field data if required; 3) previous studies involving Sentinel – 2 MSI (van der Meer et al., 2014; van der Werff et al., 2018; van der Werff & van der Meer, 2015) were performed over this region.

1.5.2. Vegetation

Rodalquilar is a sparsely vegetated area with a semi-arid climate. The vegetation present in the area is mainly grass and shrubs. Figure 1.2 (A) is a google earth image showing the presence of vegetation. Photographs from previous field studies (figure 1.2 (B)) also highlight the presence of grass and shrubs in the area.

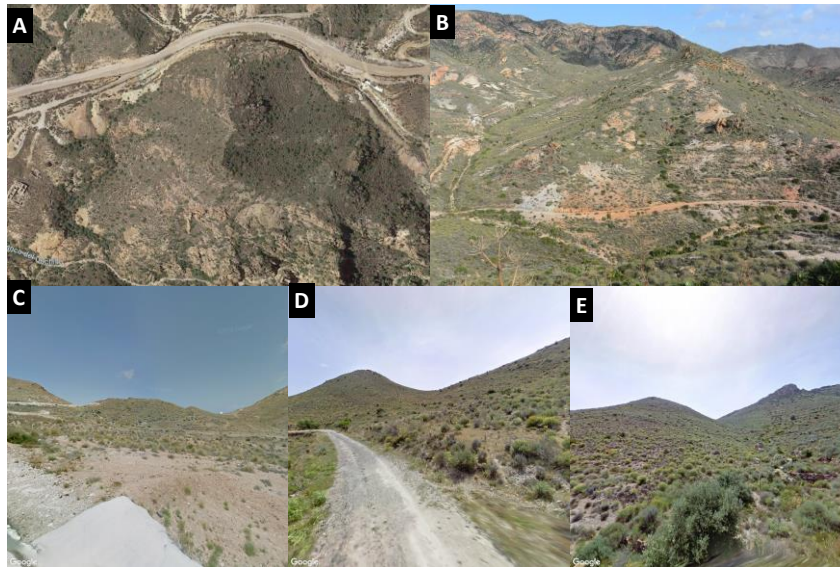


Figure 1.2: Vegetation in the study area. A is a Google Earth Image showing vegetation, B is a photograph from previous fieldwork (from ITC ESA’s archives), C, D, and E are Google Street View images.

1.5.3. Climate

In Rodalquilar, summers are hot, with mostly clear skies, and winters are cold and cloudy (Weather Spark, 2020). Generally, the average daily temperature varies between 8 and 30 degrees Celsius with an annual mean temperature of 19 degrees Celsius and a yearly rainfall of 38.5mm (see figure 1.3). Summers last from June to September, while winters last from November to March (Weather Spark, 2020). Figure 1.3 shows variations of maximum, minimum, and average temperatures (left) and average rainfall amount (right) throughout the year, 2019 (World Weather Online, 2020).

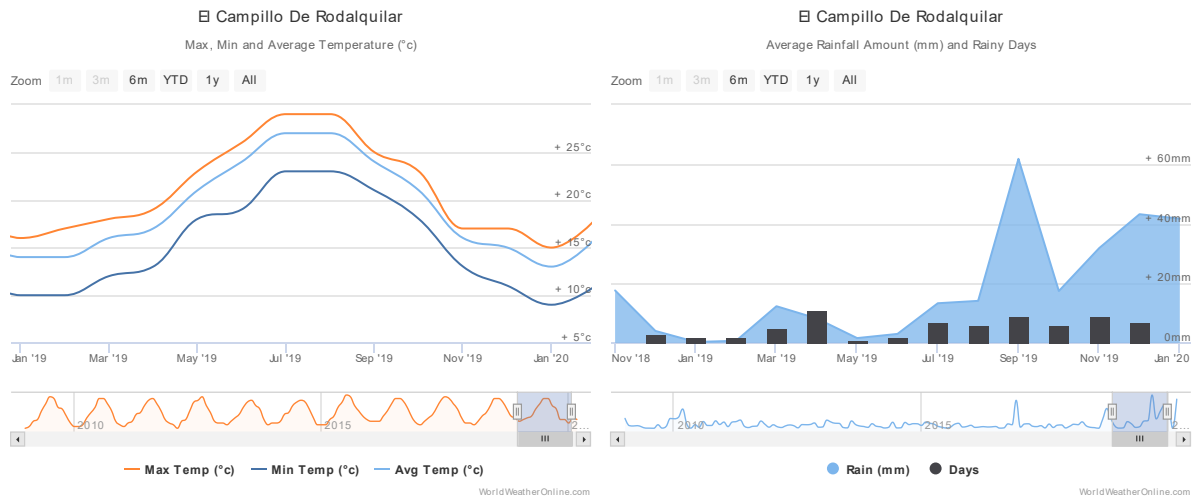


Figure 1.3: Variations of maximum, minimum and average temperatures (left) and average rainfall amount and rainy days (right) throughout the year, 2019 (World Weather Online, 2020). Data from the nearest weather station.

1.6. Related Work

The use of Sentinel 2 imagery in Geological Remote Sensing (GRS) is relatively new. Van der Meer et al. (2014) tested the potential of Sentinel 2 products for GRS. They simulated Sentinel 2 and ASTER images using airborne hyperspectral imagery from the HyMAP sensor. They compared the simulated Sentinel-2 products with the well-established ratio products from ASTER imagery (van der Meer et al., 2014). Van der Werff et al. (2015) demonstrated the capabilities of Sentinel 2 in mapping iron absorption features. They introduced a curve fitting technique for approximating the iron absorption feature using a simulated Sentinel 2 image. This research focused on the abilities of Sentinel 2 in mapping the 900nm iron absorption feature (van der Werff & van der Meer, 2015). Van der Werff et al. (2016) evaluated band ratio products relevant to geology and soil studies using imagery from the Sentinel 2 MSI instrument. They compared the results with Landsat 8 OLI and a simulated Sentinel-2A MSI dataset used by Van der Meer et al. (2014) in their study. Previous studies concluded that the Sentinel 2 MSI provides data continuity of multispectral observations with its 13 bands in the visible and near-infrared (VNIR) to shortwave infrared (SWIR) range (Meyer et al., 2019; van der Werff & van der Meer, 2016; van der Meer et al., 2014).

Multi-temporal remote sensing is not a commonly used approach in GRS, as changes in geology do not happen in days or months (in consideration with the geological time scale). Some GRS studies used multiple imageries to tackle problems such as cloud cover, illumination, and shadows (Shahriari, Honarmand, & Ranjbar, 2015), while some studies used various images to produce mosaiced products (Hewson & Cudahy, 2011). The use of imagery from multiple seasons in geological remote sensing (GRS) studies is relatively new. Van Der Werff et al. (2018) carried out a study to evaluate the relevance of the high revisit time of Sentinel 2 in Geological Remote Sensing. In this research, a multi-temporal analysis was performed with Sentinel 2 imagery. Results from this analysis show the variations in spectral indices with changing seasons, weather, and illumination conditions (van der Werff et al., 2018).

Spectral indices such as the Normalized Difference Vegetation Index (NDVI) or the Soil Adjusted Vegetation Index (SAVI) or the Enhanced Vegetation Index (EVI) (Weier & Herring, 2000) have always been used to tackle Vegetation in GRS. As mentioned in section 1.1, masking out pixels with high vegetation index values, using spectral unmixing techniques, principal component analysis amongst others, have been developed over the years to overcome the effect of vegetation on spectral signatures of the underlying geology objects (Haest et al., 2013; Rodger & Cudahy, 2009; Crippen & Blom, 2001; Bierwirth, 1990; Fraser & Green, 1987). Despite the attention on image processing techniques in overcoming the influence of vegetation, the role of time in tackling vegetation issues in GRS is yet to be explored.

Table 1 shows the list of literature relevant to this research, with their focus and findings. Studies - Van der Meer et al. (2014), Van der Werff et al. (2015), Van der Werff et al. (2016), and Van Der Werff et al. (2018) (mentioned in table 1 as 8, 5, 4, and 1) have been carried out at Rodalquilar, Southern Spain, which is also the study area of this research. This research, in a way, is a continuation of Van Der Werff et al. (2018) to explore the capabilities of the revisit time of Sentinel 2 in GRS studies.

Title	Authors and Year	Focus	Findings
“Potential of ESA's Sentinel-2 for geological applications.” (4) (1)	van der Meer et al. (2014)	Simulating Sentinel-2 products from Hyperspectral imagery and compare them with well-established ASTER band ratio data products.	Good correspondence between some of the ASTER and simulated Sentinel products.
“The Impact of Vegetation on Lithological Mapping Using Airborne Multispectral Data: A Case Study for the North Troodos Region, Cyprus.” (5) (2)	Grebby et al. (2014)	Comprehensively elucidating the impact of vegetation on lithological mapping using multispectral data.	“Vegetation abundance was found to be the primary control on the inability to classify large proportions of pixels in the imagery.”
“Comparison of multi-temporal ASTER images for hydrothermal alteration mapping using a fractal-aided SAM method.” (8) (3)	Shahriari et al., (2015)	To evaluate the effects of atmospheric correction and acquisition parameters on Spectral Angle Mapper (SAM) results.	Effect of Vegetation relatively low & SAM is independent of illumination conditions.
“Sentinel-2 for mapping iron absorption feature parameters.” (3) (4)	van der Werff & van der Meer (2015)	“Curve fitting technique for Sentinel 2 that approximates the iron absorption feature at a hyperspectral resolution.”	Wavelength position of maximum and absolute absorption depths for Iron minerals (Beryl, Bronzite, Goethite, Jarosite, and Hematite).

<p>“Sentinel-2A MSI and Landsat 8 OLI Provide Data Continuity for Geological Remote Sensing.” (2) (5)</p>	<p>van der Werff & van der Meer (2016)</p>	<p>This research focuses on Sentinel 2 band ratio products relevant to GRS and compares them with Landsat 8 products.</p>	<p>“Sentinel-2A MSI mission can provide data continuity for Landsat 8 OLI when studying mineralogy at the Earth surface.”</p>
<p>“Lithological classification using Sentinel-2A data in the Shibanjing ophiolite complex in Inner Mongolia, China.” (6) (6)</p>	<p>Ge, Cheng, Tang, Jing, & Gao (2018)</p>	<p>Assessing the ability of Sentinel 2A in performing a Lithological mapping using Machine learning methods.</p>	<p>Sentinel 2 produced results with relatively higher accuracy when compared to Landsat 8 OLI (by 5.08 %) and ASTER (by 2.5 %).</p>
<p>“A Review of Geological Applications of High-Spatial-Resolution Remote Sensing Data” (7)</p>	<p>Wu, Li, Chen, & Li (2018)</p>	<p>Need for multidisciplinary approaches in Remote Sensing for Geological applications.</p>	<p>Suggests the use of Deep Learning techniques combined with RS and Geophysical methods.</p>
<p>“Use what is there: what can sentinel-2 do for Geological Remote Sensing?” (1) (8)</p>	<p>van der Werff, Hewson, & van der Meer (2018)</p>	<p>Evaluating the high revisit time of Sentinel -2 for Geological Remote Sensing by performing a multi-temporal analysis in a hydro-thermally altered system in Southern Spain.</p>	<p>“Effect of seasonality, illumination, and weather on ground cover and the stability of spectral indices.”</p>
<p>“Land Cover Mapping in Cloud-Prone Tropical Areas Using Sentinel-2 Data: Integrating Spectral Features with NDVI Temporal Dynamics.” (9)</p>	<p>Huang et al. (2020)</p>	<p>Multi-feature classification method to integrate temporal statistical features with spectral and textural features to improve the land cover classification.</p>	<p>Results show that time-series statistical analysis performs well in mapping land cover and reducing misclassification in closely related land cover types.</p>

Table 1.1: List of relevant literature with their focus and findings.

2. METHODOLOGY

2.1. Processing Platform

Google Earth Engine was used as a platform for processing in this research. Google Earth Engine (GEE) is a cloud-based platform for geospatial analysis. GEE contains a 'multi-petabyte' catalog of satellite imagery and geospatial datasets (Hideki, 2018). It allows users to script tools and algorithms for 'planetary-scale analysis' (Hideki, 2018; Mutanga & Kumar, 2019). Analysis over large areas in time involves a huge number of images. GEE was specifically made for such analysis involving big data processing (Mutanga & Kumar, 2019). GEE was chosen as the platform for carrying out this research as it eliminated the time-consuming process of downloading the imagery, and also reduced the processing time.

2.2. Data

Multi-temporal imagery from the European Space Agency's Sentinel-2 mission was used in this research. The Sentinel-2 Multispectral Instrument (MSI) is a part of the European Union Copernicus program, which provides observations to support land management, agriculture, forestry, disaster control, humanitarian relief operations, risk mapping, and security concerns. The Sentinel-2 platform is a twin-orbit constellation (Sentinel-2A/B) with a revisit time of approximately five to ten days and extensive global coverage (Gatti et al., 2015). Table 2.1 shows the characteristics of Sentinel 2 imagery.

Band	Wavelength (nm)	Resolution (m)	Description
B1	443.9	60	Aerosols
B2	496.6	10	Blue
B3	560	10	Green
B4	664.5	10	Red
B5	703.9	20	Red Edge 1
B6	740.2	20	Red Edge 2
B7	782.5	20	Red Edge 3
B8	835.1	10	NIR
B8A	864.8	20	Red Edge 4
B9	945	60	Water Vapor
B11	1613.7	20	SWIR 1
B12	2202.4	20	SWIR 2

Table 2.1: Characteristics of Sentinel – 2 MSI. Sentinel-2 MSI has 13 spectral bands ranging from VNIR to SWIR with varying spatial resolution from 10 to 60 meters (Huang et al., 2020; Nasuti & Carriero, 2015).

The Copernicus Sentinel-2 mission aims at monitoring variability in land surface conditions (Berger et al., 2012). The mission was initially designed for land cover and other change-detection mappings. However, some of its products relevant to geology, demonstrated decent correspondence with the other multispectral satellite data (such as Landsat and ASTER) in a study conducted by Van der Meer et al. (2014). With Sentinel-2 providing data continuity for geological remote sensing (van der Meer et al., 2014; van der Werff & van der Meer, 2016) and a high revisit time (Nasuti & Carriero, 2015), it is an ideal data source for performing a time series analysis. Therefore, Sentinel-2 data was considered to be the most suitable data

source to carry out this research. List of images used with their image ID's attached in the appendix – section 7.1 (see table 7.1).

Sentinel 2 Imagery is available at two processing levels; level – 1C is the Top of Atmosphere (TOA) version, and level – 2A is the Bottom of Atmosphere (BOA) version. The level – 2A imagery is atmospherically corrected based on sen2cor (“Sen2Cor | STEP,” 2020) and is generated from the associated 1C images (Gatti et al., 2015). The Level-2A imagery includes a scene classification, additional bands such as the Quality Assessment (QA) bands for cloud masking, aerosol thickness, water vapor, snow, and cloud probability bands, amongst others. As no problems with the atmospheric correction of Sentinel 2 were mentioned by most initial studies (Clasen et al., 2015; Sibanda, Mutanga, & Rouget, 2015; van der Werff & van der Meer, 2016), no additional corrections were performed on this dataset.

The Sentinel-2, level 2A images were accessed via the Google Earth Engine Image Collection - "COPERNICUS/S2_SR". This Image collection contains images that were accessed via the European Space Agency's (ESA) Sentinel Scientific Data Hub (<https://scihub.copernicus.eu/>).

In addition to Sentinel 2 imagery, pictures from previous fieldworks (via ITC ESA archives), Google Earth imagery, and Street View were also used.

2.3. Image Selection

To understand the influence of vegetation on the spectra of geological objects, it is crucial to have imagery from all seasons as vegetation changes with seasons (Ye et al., 2019). A period of thirteen months was chosen from January 2019 to January 2020. The Sentinel-2 Level 2A image dataset in GEE contains 75 images in this timeframe. However, some of the images include a large amount of cloud cover. To filter these images, one of the metadata properties of Sentinel-2 imagery, the "Cloud Coverage Assessment," was used. The Image dataset was filtered by setting a threshold for Cloud Coverage Assessment at 10 percent (see section 7.4.1 for the script). The cloud coverage assessment is a property that indicates the percentage of the cloud for the complete image but not a particular region of interest within the image. This threshold resulted in the final dataset having 40 images. Despite filtering the dataset for images with less than 10 percent, there were images with cloud cover in the study area as the metadata property is based on the whole image.

2.4. Data Preparation

All images were spatially subset to the study area; the subset covers approximately 33.55 square kilometers. The region of interest was chosen to be similar to a previous study by van der Werff & van der Meer (2016), which includes potential areas of interest. Additionally, the image collection was spectrally subset to exclude the bands which were not required for this research. The final image collection consisted of only the optical bands ('B1', 'B2', 'B3', 'B4', 'B5', 'B6', 'B7', 'B8', 'B8A', 'B9', 'B11', 'B12') from all the 40 images. All the bands were left at their original spatial resolutions, as mentioned in table 2.1. However, in further processing, when products were computed from bands with different resolutions, the bands were resampled (on the fly) to the highest resolution using the nearest neighbor resampling technique.

2.5. Band Ratios

Band ratios were used to identify areas and pixels with geological objects or vegetation. The technique of using band ratios for observing spectral variations has been used for many years now (Abrams & Yamaguchi, 2019; van der Werff & van der Meer, 2016; van der Meer et al., 2014; Imbroane et al., 2007). Van der Werff & van der Meer, (2016) modified some of the commonly used band ratios for mapping mineral assemblages to match Sentinel-2 in their study. Iron Oxides ratio, Laterite ratio, Normalized Differential Vegetation Index (NDVI) (van der Werff & van der Meer, 2016), and Soil Adjusted Vegetation Index (SAVI) (Huete, 1988) were used in this research. Additionally, band ratios were defined based on spectral features observed in specific pixels. All the ratios used in this research are mentioned in table 2.2.

Name		Band Ratio	Modified ratio for resampling	Resolution
NDVI	NDVI	$(B8-B4)/(B8+B4)$	$(B8-B4)/(B8+B4)$	10m
SAVI	SAVI	$(B8-B4) * (1+L)/(B8+B4+L)$	$(B8B4) * (1+0.428)/(B8+B4+0.428)$	10m
Iron Oxides ratio	BR 1	$B4/B2$	$B4/B2$	10m
Laterite ratio	BR 2	$B11/B12$	$(B4*B11)/(B12*B4)$	10m
835 nm feature	BR 3	$B7/B8$	$(B4*B7)/(B8*B4)$	10m
864 nm feature	BR 4	$B8/B8A$	$(B4*B8)/(B8A*B4)$	10m
Vegetation Index	BR 5	$B8/B4$	$B8/B4$	10m

Table 2.2: List of band ratios used in the research with their modified formulae and output resolutions. NDVI, SAVI, BR1, BR2, and BR5 were adapted from van der Werff & van der Meer (2016); BR4 and BR5 were defined based on features observed in the geology pixels.

The normalized difference vegetation index (NDVI) is a normalized ratio of the NIR (near-infrared) and red bands. (Mašková, Zemek, & Květ, 2008; Padmanaban, Bhowmik, & Cabral, 2017). NDVI has been widely used in many geological remote sensing studies as a proxy for estimating vegetation (Gascon et al., 2014; Grebby et al., 2014; Traore, Çan, & N, 2018; F. D. Van der Meer et al., 2014). However, atmospheric changes and soil conditions affect NDVI (Mašková et al., 2008). With Rodalquilar being a semi-arid area with sparse vegetation, the possibility of soil affecting vegetation pixels is prominent. To tackle soil induced variations, Soil Adjusted Vegetation Index (SAVI) was also used in this research. SAVI is similar to NDVI in structure but has an additional factor correcting for soil brightness. (Almutairi, El, Belaid, & Musa, 2013; Huete, 1988; Qi, Chehbouni, Huete, Kerr, & Sorooshian, 1994). This band ratio was modified based on NDVI modified by van der Werff & van der Meer (2016) for Sentinel-2, as mentioned in table 2. For Sentinel-2, the soil adjustment factor (L) was defined to be 0.428 by the European Space Agency (“SAVI (Soil Adjusted Vegetation Index) | Sentinel-Hub custom scripts,” 2020).

As mentioned in table 2.1 (section 2.2), the spatial resolution of Sentinel-2 imagery varies from 10 meters to 60 meters, depending on the spectral band. In cases where bands of different resolutions were used, spatial resampling had to be done. In GEE, this is done on the fly using the Nearest Neighbor resampling technique by default (“Resampling and Reducing Resolution | Google Earth Engine,” 2020). The output resolution of the ratio product would be the resolution of the first band in the band ratio. For example, in the case of BR 2 (see table 2.2, and scripts in the appendix (section 7.4.3)), the ratio was modified by adding

B4 in both the denominator and nominator. This resulted in the output resolution to be in line with the other band ratio products, which is 10m.

2.6. Analysis Tools

Throughout the research, tools, and visualizations such as annual statistics of band ratio images, time series charts of band ratios, 2D and 3D spectral response curves, and time-lapses of image visualizations were used. These tools were used to explore the dataset and observe changes in the study area over time.

Annual band ratio statistics were computed for all the band ratios mentioned in section 3.5. The band ratios were added as a new band to each image present in the final image collection. Based on these band ratio variations over the period – January 2019 to January 2020, the mean and standard deviation were computed for each pixel. The result was an image with annual band ratio statistical values, namely mean and standard deviation of every pixel in the study area.

Band ratio time series charts were also produced for specific pixels, from classes such as water, natural vegetation, croplands, bare soil, outcrop, and shadow. The band ratio images which were added to the image collection as extra bands were used to produce these charts. The resulting chart was the variation over time of a particular band ratio from a specific pixel. These time series charts and annual band ratio statistic images not only provided a basic idea of what's happening over time in the region but also were used in the pixel selection. Also, visualizing them helped in understanding possible abnormalities due to elevation, shadows, human interference, amongst others. Additionally, time-series of individual bands were also produced for specific pixels.

Spectral response curves or spectral signatures (2D) were extracted for specific pixels from every image in the dataset. Additionally, the spectral signatures of various pixels were extracted to observe and understand the area during the data exploration phase. These curves were exported into Comma Separated Values (CSV) files and were then combined in one CSV file. The resulting CSV was used to create a 3D surface curve in Python, to get a quick overview of the variations over time. These 3D spectral signature curves also helped in the process of looking for the presence of cloud cover or shadow over the pixel. Time-lapses of image visualizations were also used as analysis tools in this research. Image visualizations such as true-color composites, false-color composites, and composites of band ratios were used in these time-lapses. These time-lapses provided an overview of the presence of cloud cover and shadows in the imagery. They also gave an overall idea of the region's changes over the period of 13 months in the earlier stages of the research.

2.7. Pixel Selection

Pixels were selected for time series analysis by combining visual inspection with time series of band ratios and annual band ratio statistics. The study area was visually inspected using google earth imagery, true-color composites from the Sentinel-2 image dataset (bands B4 in red, B3 in green, and 2 in blue), along with inputs from previous studies and fieldwork. Upon visual inspection, certain areas such as an outcrop, agriculture land or croplands, mountains with natural vegetation, mountains causing shadows, a parking lot with bare soil, and a lake were shortlisted as regions to inspect further. These regions were then analyzed further using time series of band ratios, and the statistics of band ratios.

2.7.1. Vegetation Pixels

The study area is sparsely vegetated with mostly shrubs and grass. The NDVI of these vegetation pixels was expected to be varying between 0.3 and 0.6 over the period. Therefore, pixels with a mean NDVI in the range of 0.3 and 0.6 were selected as probable vegetation pixels. The NDVI and SAVI time series charts of these pixels were then checked, and if they showed similar variations, the pixels were confirmed as vegetation pixels. With vegetation changing over time, a high standard deviation could be expected. However, with the vegetation in the region being very sparse, the standard deviation might not be as high as expected.

2.7.2. Geology Pixels

Pixels containing geological objects, i.e., rocks from outcrops, soil surfaces are Geology pixels. For selecting geology pixels, band ratios (BR1 and BR2) mentioned in table 2, along with the vegetation indices (NDVI and SAVI), were used. Geology objects do not change in one year, so the band ratios should be almost similar throughout the year. Since these pixels do not contain much vegetation and they do not undergo any changes within the period, the mean and standard deviation of the Vegetation Indices (NDVI and SAVI) of geology pixels should be low. After inspecting pixels in the region, thresholds (expected ranges) were set; the mean BR1 (iron oxide ratio) was expected to be around 2, and the mean BR2 (laterite ratio) was expected to be around 1.5 for geology pixels.

Geology pixels can either be pure or mixtures with vegetation or bare soil. Sentinel-2 imagery has a resolution of 10 to 60 meters (as mentioned in table 2.1), which makes mixed pixels a high possibility. With one of the objectives of this research being able to identify the influence of natural vegetation on remotely sensed spectra of geological objects, pixels with mixtures of geological objects and vegetation should also be selected. In the case of mixtures with vegetation, the vegetation indices were expected to have a slight increase in their standard deviation. As the vegetation part of the pixel changes over time, the band ratios of the pixels might also show variations over the year. The band ratio time-series charts were used to observe these variations. The vegetation indices of these pixels were expected to show a similar trend that of the vegetation pixels.

The selected geology pixels were expected to contain both pure and mixed pixels. Therefore, pixels with slightly higher Vegetation Indices (NDVI and SAVI) mean and standard deviation were also selected. Target ranges were set to ensure the selection of both mixed and pure geology pixels. Table 2.3 shows the target ranges for the annual band ratio statistical values. These target ranges were used only to select pixels. The selected pixels were classified 'pure' and 'mixed' using the Band Ratio time-series curves, in the next stage. Pixels with low Vegetation Indices (NDVI and SAVI) mean over the period along with low standard deviation were chosen as probable geology pixels. These pixels were then checked for variations in geology band ratios. If the mean of geology band ratio was high (around 2 for BR1, and 1.5 for BR2), and low standard deviation (1 for BR1, and 0.5 for BR2), the pixels were selected as geology pixels. Each pixel was also inspected visually using google earth and true-color composites before selection. Additionally, the band ratio variations of the surrounding pixels were also checked for false positives. List of band ratio statistical values for all pixels attached in the appendix – section 7.2 (see table 7.2)

2.7.3. Pixel Definition

The selected pixels included both mixed and pure pixels. To understand the influence of vegetation on geological objects, time series on both pure and mixed pixels are required. So, the chosen pixels had to be classified as either pure geology pixels or mixtures with vegetation. The band ratio time-series charts were used in this process of categorizing the pixels. Out of the selected pixels, a reference pixel was picked from each class. This was done based on the fact that vegetation changes over time, and geology does not. So, the band ratio time series of pure geology pixels would have a trend that is almost a straight line. On the other hand, the band ratio time series of mixtures with vegetation would have a trend similar to that of pure vegetation. The pixels which showed expected behavior were picked as reference pixels.

The time series of NDVI of all the pixels were subjected to trend fitting. Parabola like curves were expected for vegetation and mixed pixels. Therefore, second-order polynomial trendlines were used to fit all the time series charts. The trendlines were then used to do the classification. The rate of change of the slope (R) is the second derivative of the curve equation, gives an idea of how the curve is changing. R was calculated for each curve using the equations. The curves of pure geological pixels were expected to be almost a horizontal line, with the rate of change in slopes being nearly zero (1.60E-06). The curves of vegetation pixels were expected to be similar to that of a parabola with a vortex in the summer. Mixtures, on the other hand, were expected to have the same trend that of vegetation but with a flattened curve (empirically derived).

Combining the rate of change of slope with Band Ratio statistics and visual inspection, the selected geology pixels were classified into pure and mixed. The rate of change of slope of each pixel was then compared to the reference pixels to classify them. $R \times 10E07$ (to compare easily) was used as a coefficient. Since factors such as atmospheric changes, variations in soil moisture, etc., were not included in the classification, there were possibilities of misclassification. To validate the pixel classification, each pixel was again inspected visually and using the band ratio annual statistics. The process of trend fitting was repeated with SAVI time-series curves. Results from trend fitting of NDVI and SAVI curves were then compared, and the final decision on classification was taken.

Table 2.3: List of target ranges of annual band ratio statistical values used to select geology pixels.

Annual Band Ratio Statistical Value	Target Range
NDVI Mean	Below 0.2
NDVI Std Dev	0.01 to 0.04
SAVI Mean	0.00 to 0.13
SAVI Std Dev	0.01 to 0.03
BR 1 Mean	Around 2 (1.5 to 2.5)
BR 1 Std Dev	Low (below 1)
BR 2 Mean	Around 1.5
BR 2 Std Dev	Low (below 0.5)

3. RESULTS

Pixels from various classes were selected using visual inspection (of Google Earth and Sentinel 2 imagery) and temporal statistics of band ratios. Band ratios defined in previous studies and band ratios based on prominent features were used (see table 1.3). These pixels were classified into vegetation, pure geology, and mixed pixels based on their NDVI and SAVI time series curves. Time series on spectra and band ratios of the selected pixels (pixels from all three classes) was performed to observe and compare the variations. The results from pixel selection (section 3.1), time series (section 3.2), and observations in the presence of clouds and shadows (section 3.3) are described in this chapter.

3.1. Pixel Selection

The shortlisted areas of interest for picking pixels to trace over time are shown in figure 3.1. Probable areas for selecting pixels were shortlisted based on previous knowledge (target regions in previous studies), and visual inspection. The potential areas of interest in the study area were agriculture land which seemed to be dynamic (could be observed clearly with time-lapse of true-color composites) over the time period (area B in figure 3.1), outcrops (area C in figure 3.1), vegetated mountains (area A in figure 3.1), and evaporite mountains with prominent shadows (area D in figure 3.1). The agriculture land also contained an artificial water body, and so this region was chosen as a probable location for cropland and water pixels.

Two pixels were selected as representative pixels for natural vegetation in the study area. The two natural vegetation pixels were chosen from the region A- (vegetation pixel 1: $36^{\circ}50'56.8''\text{N}$ $2^{\circ}03'16.1''\text{W}$, vegetation pixel 2: $36^{\circ}50'57.3''\text{N}$ $2^{\circ}03'17.8''\text{W}$) (figure 3.1). The natural vegetation in the study area is very sparse with mostly grass and shrubs due to which, most vegetation pixels were mixtures with the underlying soil (see

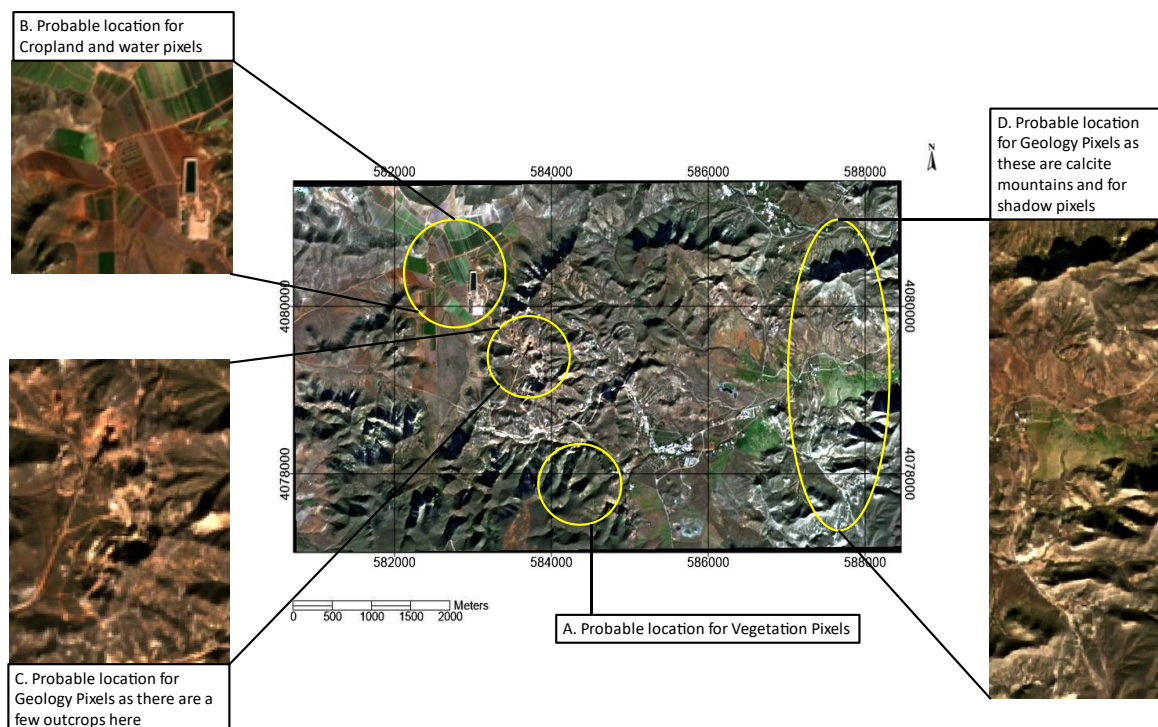


Figure 3.1: Shortlisted Regions after visually inspecting the study area. The image is a true color composite (bands B4 in red, B3 in green, and 2 in blue) from January 1, 2019. Region C contains visible outcrops, B contains croplands, D contains calcite mountains with pixels covered in shadow and A contains vegetated mountains.

figure 1.2). To make sure the selected natural vegetation pixels were representative, a cropland pixel was selected from region B (figure 3.1) for comparison. In total, these three pixels (two natural vegetation pixels and one cropland pixel) were chosen as vegetation pixels for the time series. The standard deviation of the NDVI of vegetation pixels was around 0.1, but a clear trend in the variation could be observed over the year (figure 3.2 shows the trend). With NDVI values decreasing from winter to summer and also increasing from summer to winter (symmetrically), the standard deviation of NDVI for vegetation pixels was not as high as expected (see table 7.2 in the appendix – section 7.2).

Twenty geology pixels were selected from regions C and D (figure 3.1) for the time series analysis. NDVI variation of all the pixels was observed, and reference pixels were picked based on their trends. Geo Pixel 20 was chosen as a reference for pure geology pixel as it's NDVI values remained low and almost constant. The NDVI time series of Geo Pixel 20 was nearly a straight line (with R of 1.60E-06) (figure 3.2), and the NDVI values were very low throughout the year. On the other hand, Geo Pixel 4 had NDVI values varying similarly to that of the vegetation. The NDVI values started around 0.3 in January 2019 and kept decreasing till June 2019. After this, they increased (towards 0.3) at the end of the year. Therefore, Geo Pixel 4 was chosen as a reference for mixtures with vegetation (mixed pixels). Table 3.1 shows the selected reference pixels and a description of their location.

Table 3.1: List showing reference pixels and their locations. Pure Geology Pixel and Mixed Pixel were picked from one of the outcrops (region C in figure 1), and Vegetation pixel was chosen from the vegetated mountains (region A in figure 1).

	Pixel	Reference for	Description of the location
1	Geo Pixel 20	Pure Geology Pixel	From one of the outcrops
2	Vegetation	Vegetation Pixel 1	From a mountain with sparse vegetation
3	Geo Pixel 4	Mixed Pixel	From one of the outcrops

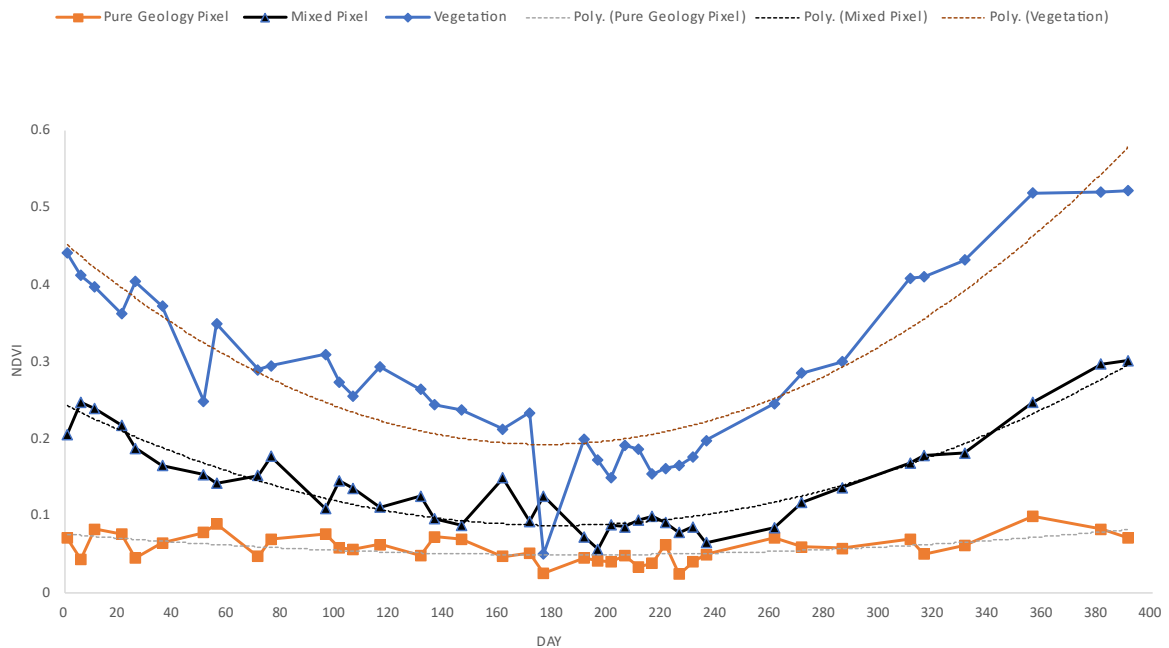


Figure 3.2: Chart showing NDVI time series of the reference pixels. Blue (with diamonds as datapoints) being from a Vegetation pixel, orange (with squares as datapoints) being from a pure geology pixel, and black (with triangles as datapoints) being from a mixed pixel. The dotted lines show the best fit second degree polynomial trend curves. The x-axis is the number of days in the chosen time frame of this research (Jan1 2019 to Jan 26, 2020) which is 391.

The classification of the selected pixels resulted in seven pure geology pixels and thirteen mixed pixels. After validating the classification, three pixels were found to be misclassified. Geo Pixels 9, 10, and 11 were misclassified as mixed pixels as the rate of change of slopes were very close. These misclassifications were corrected by including SAVI time series curves and visual inspection, which resulted in ten pure and ten mixed pixels for time series. Table 5 shows the results of pixel selection and classification, including the curve equations of the NDVI time series curves. Figures 3.3 shows NDVI time series curves (along with their second-degree trend curves) for geo pixels 1 and 14. NDVI time series curves of reference (mixed and pure geology) pixels were also included to compare the trends (similar time series curves for all the pixels are attached in the appendix – section 7.2 (figures 7.1 and 7.2 in appendix)).

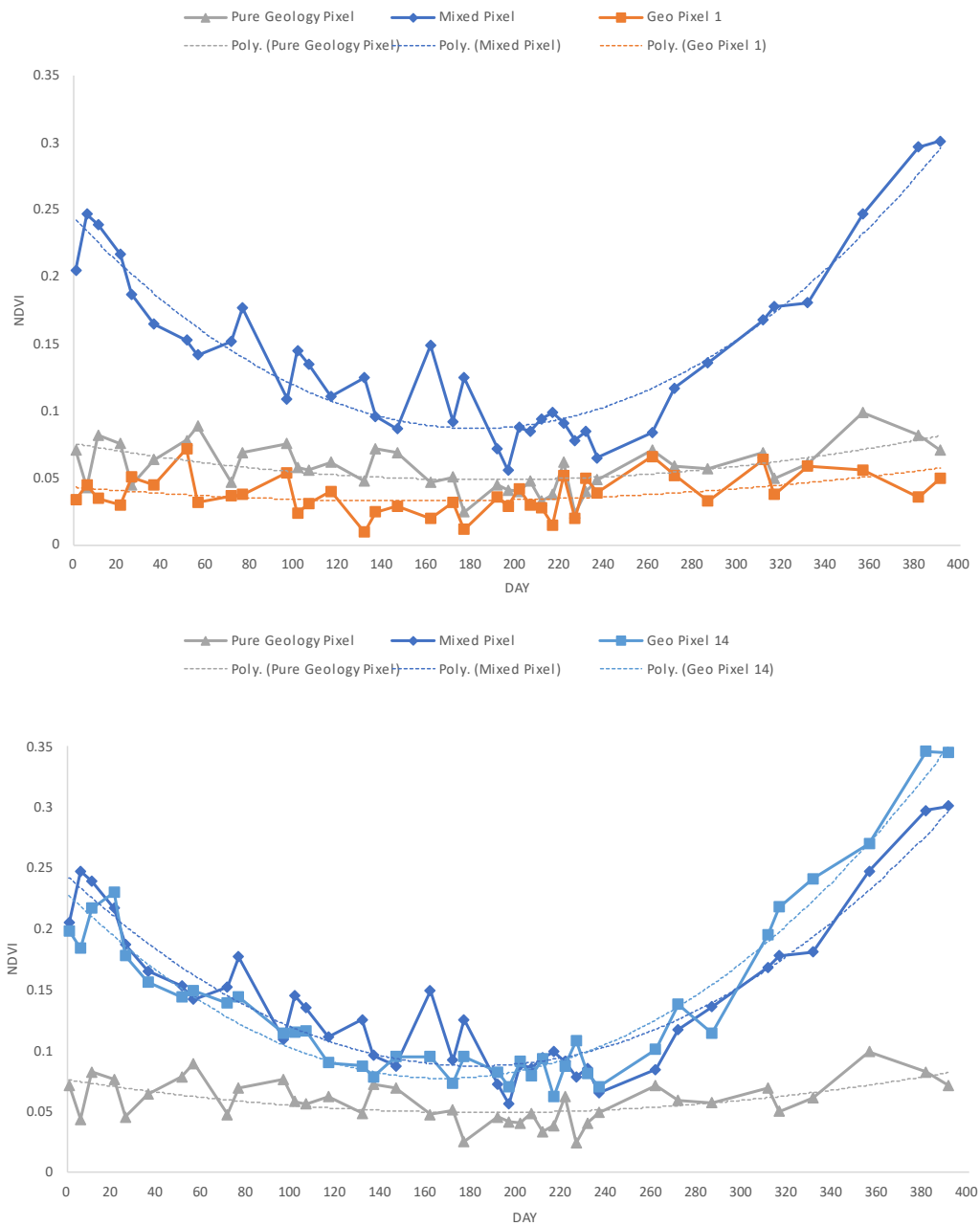


Figure 3.3: NDVI time series curves for geo pixels 1 (top) and 14 (bottom) along with the reference pixels. The charts show a comparison with the time series of the reference pixels. The orange curve (with data points as squares) shows the variation of NDVI for a pure geological pixel, and the grey curve (with triangles as data points) shows the variations of NDVI for a mixed pixel.

Pixel	Location	Curve equation of the trend	Rate of change of slope (R)	R*(10E7)	Classification Result	Final Classification
Geo Pixel 1	36°51'17.8"N 2°03'20.7"W	$y = 4E-07x^2 - 0.038x + 829.3$	8.00E-07	8	Pure	<i>Pure</i>
Geo Pixel 2	36°51'17.1"N 2°03'21.9"W	$y = 3E-07x^2 - 0.0281x + 612.85$	6.00E-07	6	Pure	<i>Pure</i>
Geo Pixel 3	36°51'16.8"N 2°03'21.2"W	$y = 2E-07x^2 - 0.0183x + 399.03$	4.00E-07	4	Pure	<i>Pure</i>
Geo Pixel 4	36°51'17.5"N 2°03'34.5"W	$y = 5E-06x^2 - 0.4151x + 9059.2$	1.00E-05	100	Reference for Mixed	<i>Mixed</i>
Geo Pixel 5	36°51'18.8"N 2°03'38.1"W	$y = 9E-07x^2 - 0.0746x + 1627.8$	1.80E-06	18	Pure	<i>Pure</i>
Geo Pixel 6	36°51'27.0"N 2°03'39.2"W	$y = 3E-06x^2 - 0.2886x + 6298.2$	6.00E-06	60	Mixed	<i>Mixed</i>
Geo Pixel 7	36°51'28.6"N 2°03'39.6"W	$y = 3E-06x^2 - 0.2319x + 5062.3$	6.00E-06	60	Mixed	<i>Mixed</i>
Geo Pixel 8	36°51'28.9"N 2°03'39.2"W	$y = 1E-06x^2 - 0.0832x + 1816$	2.00E-06	20	Pure	<i>Pure</i>
Geo Pixel 9	36°51'29.9"N 2°03'42.4"W	$y = 2E-06x^2 - 0.1798x + 3922.4$	4.00E-06	40	Mixed	<i>Pure</i>
Geo Pixel 10	36°51'30.5"N 2°03'41.6"W	$y = 2E-06x^2 - 0.2067x + 4510.6$	4.00E-06	40	Mixed	<i>Pure</i>
Geo Pixel 11	36°51'30.9"N 2°03'41.2"W	$y = 2E-06x^2 - 0.1387x + 3028.2$	4.00E-06	40	Mixed	<i>Pure</i>
Geo Pixel 12	36°51'31.5"N 2°03'37.9"W	$y = 2E-07x^2 - 0.0214x + 466.63$	4.00E-07	4	Pure	<i>Pure</i>
Geo Pixel 13	36°50'11.9"N 2°00'57.0"W	$y = 2E-06x^2 - 0.1582x + 3453$	4.00E-06	40	Mixed	<i>Mixed</i>
Geo Pixel 14	36°51'27.6"N 2°03'37.2"W	$y = 5E-06x^2 - 0.4751x + 10366$	1.00E-05	100	Mixed	<i>Mixed</i>
Geo Pixel 15	36°50'11.9"N 2°00'57.0"W	$y = 4E-06x^2 - 0.3582x + 7815.2$	8.00E-06	80	Mixed	<i>Mixed</i>
Geo Pixel 16	36°51'32.0"N 2°03'37.0"W	$y = 2E-06x^2 - 0.2123x + 4629.8$	4.00E-06	40	Mixed	<i>Mixed</i>
Geo Pixel 17	36°51'52.7"N 2°01'10.7"W	$y = 3E-06x^2 - 0.2765x + 6035$	6.00E-06	60	Mixed	<i>Mixed</i>
Geo Pixel 18	36°51'34.7"N 2°03'33.1"W	$y = 2E-06x^2 - 0.1569x + 3425.2$	4.00E-06	40	Mixed	<i>Mixed</i>
Geo Pixel 19	36°51'26.0"N 2°03'41.3"W	$y = 2E-06x^2 - 0.1551x + 3385.4$	4.00E-06	40	Mixed	<i>Mixed</i>
Geo Pixel 20	36°51'29.5"N 2°03'38.9"W	$y = 8E-07x^2 - 0.0681x + 1486.6$	1.60E-06	16	Reference for Pure	<i>Pure</i>

Table 3.2: The result of pixel definition along with each pixel's NDVI time series' second-degree trend equation. R is the rate of change of the curve's slope. R*10E7 was used as a coefficient to compare the curves. The sixth column (in italics) is the final classification of the pixels with ten pure and ten mixed pixels.

3.2. Time Series

The purpose of this research is to assess the role of time in geological remote sensing in exploring the impact of vegetation. Pixels were selected with target classes - vegetation and geology. Pixels containing geological objects, i.e., rocks from outcrops, soil surfaces are geology pixels. With the spatial resolution of 10-60m, mixtures were expected in geology pixels. The selected geology pixels were classified as 'pure' and 'mixed.' Vegetation in this area is very sparse with mostly grass and shrubs (see figure 1.2 in section 1.5), so most of the vegetation pixels are mixtures. The selected vegetation pixels were representative of the vegetation in the study area. The results from representative selected pixels are shown in this chapter. Table 3.3 shows the list of pixels. The pixels were renamed, and the new names (in italics in Table 3.3) will be used for the remainder of the thesis.

Original Pixel	Class	New Name
Vegetation pixel 1	Vegetation	<i>Vegetation 1</i>
Vegetation pixel 2	Vegetation	<i>Vegetation 2</i>
Geo Pixel 2	Pure geology	<i>Pure Geology 1</i>
Geo Pixel 3	Pure geology	<i>Pure Geology 2</i>
Geo Pixel 4	Mixture	<i>Mixed 1</i>
Geo Pixel 7	Mixture	<i>Mixed 2</i>
Geo Pixel 14	Mixture	<i>Mixed 3</i>
Geo Pixel 18	Mixture	<i>Mixed 4</i>

Table 3.3: List of pixels for which the time series results are shown in this section with their classes.

The time series was performed on spectra, band ratios, and reflectance values of individual bands pixels from all three classes. Vegetation undergoes changes in a short time, but geology does not change in short intervals. Therefore, spectra from vegetation pixels are expected to vary according to seasons and spectra from pure geology to remain similar throughout the thirteen months (January 2019 to January 2020). Mixed pixels, on the other hand, are expected to be influenced by the vegetation part in the pixel, and spectra are expected to show some seasonal variations. Figure 3.4 shows this expected difference between signals from vegetation and geology part in mixed pixels. The depth of the feature from the geology part remains almost constant (around 1.1, with slight variations), while the depth of the feature from the vegetation part keeps changing considerably. This research attempts to differentiate the signals coming from the parts in mixed pixels.

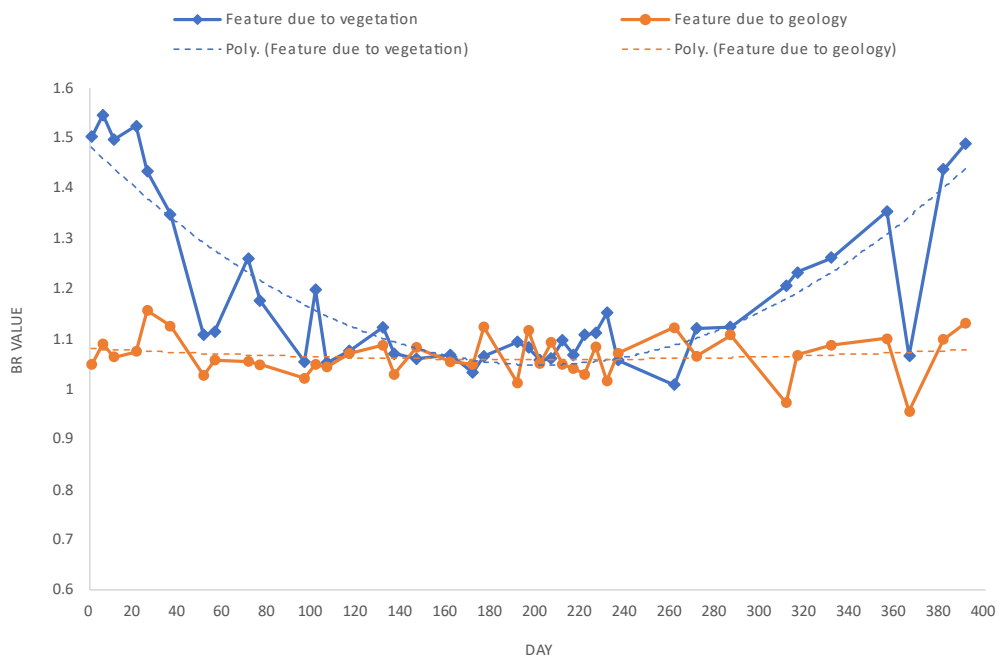


Figure 3.4: Comparison of depth of absorption features from the vegetation and geology parts of the pixel. Blue (with diamonds as datapoints) curve shows the depth of feature due to vegetation and orange (with circles as datapoints) shows the depth of feature due to the geology part in the pixel.

All time-series curves are based on the thirteen-months dataset (January 2019 to January 2020) except for the band ratio time series of vegetation pixels; for the band ratio of vegetation pixels, an extended period of two years is used, to make sure the variations in vegetation are annual and estimate the green peak for this study area.

3.2.1. Time Series on Spectra

Spectra from all the images were extracted for the selected pixels, and the variations over time were analyzed. Spectra from all the images were examined, but representative spectra from different seasons were chosen to display in the time series charts. Results from representative pixels (from the different classes) will be shown in this subsection.

For vegetation pixels, spectra from spring, summer, and autumn are relatively similar with relatively higher reflectance values in almost all bands. This difference is comparatively higher in the visible and red-edge bands. Figure 3.5 shows the spectra of vegetation pixel 1 for several months. Figure 3.5 B shows spectra from winter months, and 3.5 A shows spectra from spring, summer, and autumn. The comparison between summer and winter spectra can be seen in figure 3.5 C and D. The absorption feature depths at 496.6 nm (visible-blue region) and 664.5 nm (visible-red region) are relatively higher in winter (see figure 3.5 D). Overall, the spectra from 40 images (spread out from January 2019 to January 2020) fall into three clusters – a cluster with spectra from summer, a cluster with spectra from winter, and a cluster with spectra falling in between (see figure 3.5 C).

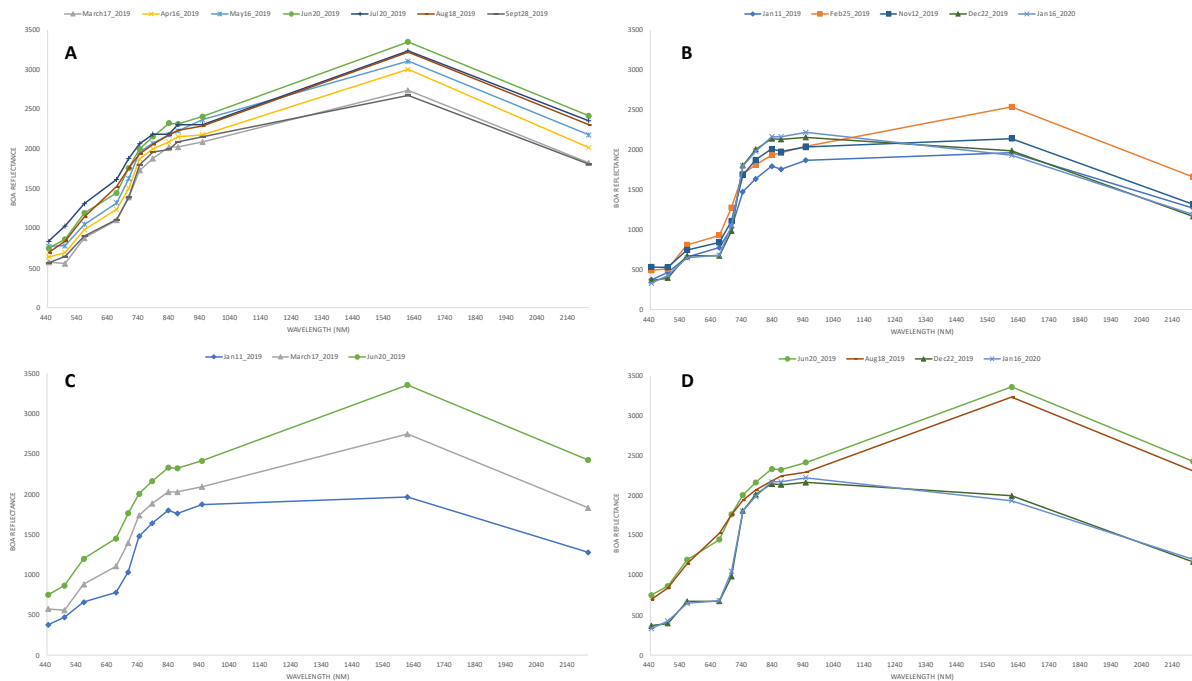


Figure 3.5: Spectral reflectance curves of vegetation 1 pixel from different months. A shows the spectra from spring, summer and autumn months (March to September 2019), B shows spectra from winter months, C and D are comparison of summer and winter spectra. All spectra have been extracted from cloud free images.

Geology does not change in thirteen months; however, various factors affect the spectra obtained from remotely sensed imagery. To study the variations in spectra of geology pixels, a time series was performed on spectra of pure geology pixels. The spectra of pure pixels appeared to vary over time; considerable variations could be seen in the 700 nm to 900 nm wavelength region (mostly red edge bands). Figure 3.6 shows the spectra of pure geology pixel 1 from various months. The spectral response curves of pure geology pixel 1 did not show any seasonal variation, and no clusters could be seen. Figure 3.6 B and A show spectra from winter and the rest of the seasons (March to September 2019) respectively, spectra from all

seasons are almost similar (with slight variations in the 700nm to 900nm wavelength region; see figure 3.6 A, B, and D). Within the 700 nm to 900 nm region, there were variations in features within a single month (figure 3.6 C). In January 2019, no two images had the same shape in 700 nm to 900 nm region (see figure 3.6 C). Figure 3.6 D shows the spectra of pure geology pixel 1 from all months, a feature at 945 nm can be seen in spectra from every month. The depth of this feature seems to be varying over time; the absorption feature is deeper in January 2019, and the depth keeps decreasing gradually till May 2019, after which the depth starts to increase gradually towards January 2020 (see figure 3.6 D). A peak at 1613.70 nm can also be seen in spectra from all months. Interestingly, the height of this peak varies directly proportional to the depth of the absorption feature at 945 nm; i.e., when the depth of the feature at 945 nm is the lowest in January 2019, the height of the peak is the maximum. Overall, similar behavior could be seen in other pure geology pixels (figure 7.3 in the appendix shows spectral variations over time of pure geology pixel 2).

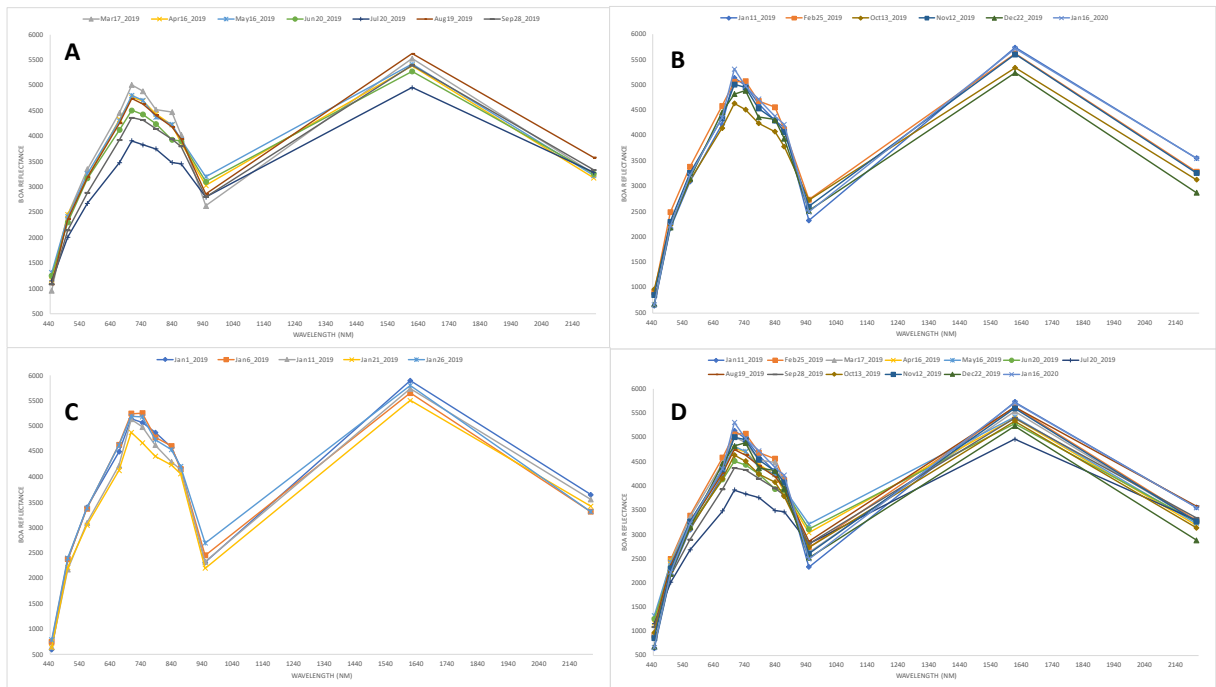


Figure 3.6: Spectral reflectance curves of pure geology pixel 1 from different months. A shows the spectra from spring, summer and autumn months (March to September 2019), B shows spectra from winter months. C shows variations in spectra within one month (January 2019) and D shows one spectra each from all thirteen months. All spectra have been extracted from cloud free images.

After the time series on spectra of vegetation and pure geology pixels, time series analysis was performed on spectra of mixed pixels. The purpose was to observe any seasonal changes in spectra and to link variations in spectra to the vegetation and geology parts of the mixed pixel. Spectra of mixed pixel 3 showed seasonal variations with three clusters (the clusters can be seen in figure 3.7 D; A, B, and C show these clusters individually). Spectra of mixed pixel 1 showed variations in spectra over time, but the variations were not prominently related to seasons. An absorption feature at 835 nm could be observed in spectra from all months for both these pixels (see D in figure 3.7 and D in figure 3.8). This feature is relatively deeper and prominent in comparison with the rest of the features for these pixels. For mixed pixel 3, the depth of this absorption feature kept varying over time; the feature is deeper in winter (see B in figure 3.7), very shallow in summer (see A in figure 3.7), and relatively deep in other months (see C in figure 3.7). For mixed pixel 1, the depth of the feature at 835 nm varied with time but not as prominent as mixed pixel 3. Slight variations in 700 nm to 900 nm can also be seen in the time series on the spectra of mixed pixels.

Most mixed pixels showed behavior similar to mixed pixel 3; three clusters of spectra could be observed. In some pixels (for example, mixed pixel 2 and mixed pixel 4; spectra from all months attached in appendix, see figure x), a prominent feature could be seen in all months with varying feature depths and a relatively smaller feature could be seen in spectra from summer images.

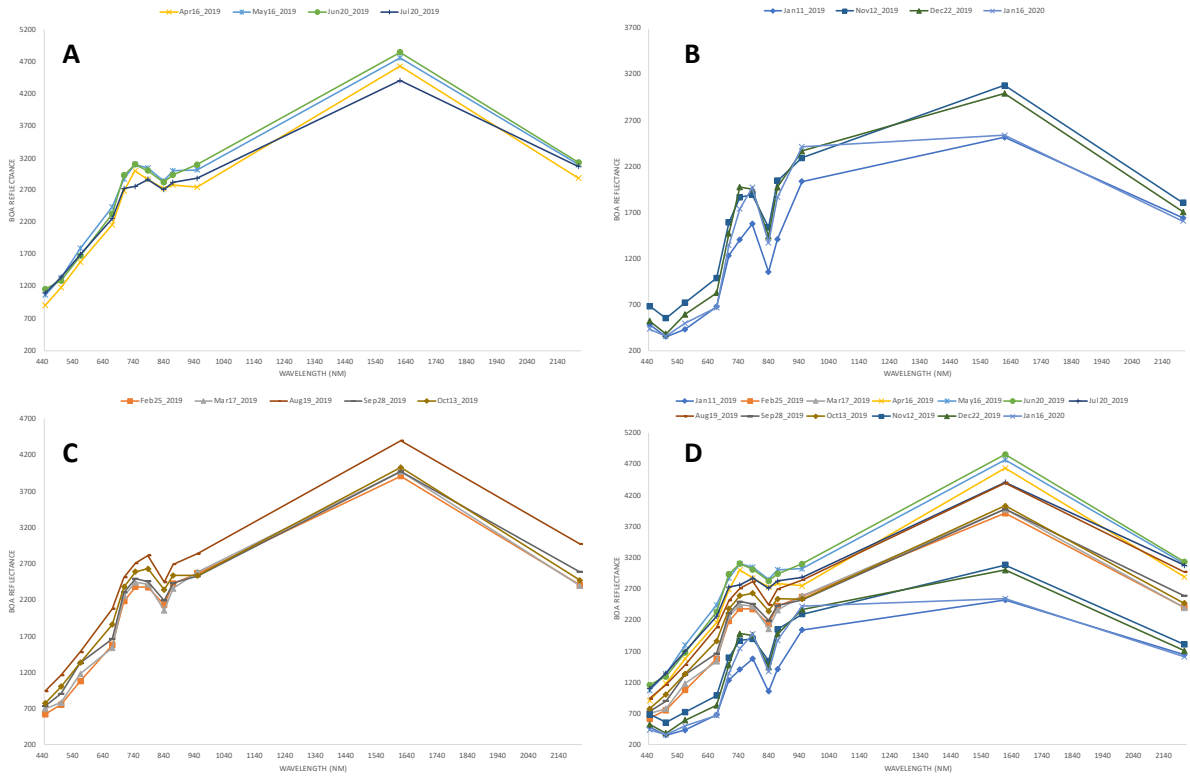


Figure 3.7: Spectral reflectance curves of mixed pixel 3 from different months. A shows the spectra from summer (April to July 2019), B shows spectra from winter months and C shows variations in spectra in the other months. D shows one spectra each from all thirteen months. All spectra have been extracted from cloud free images.

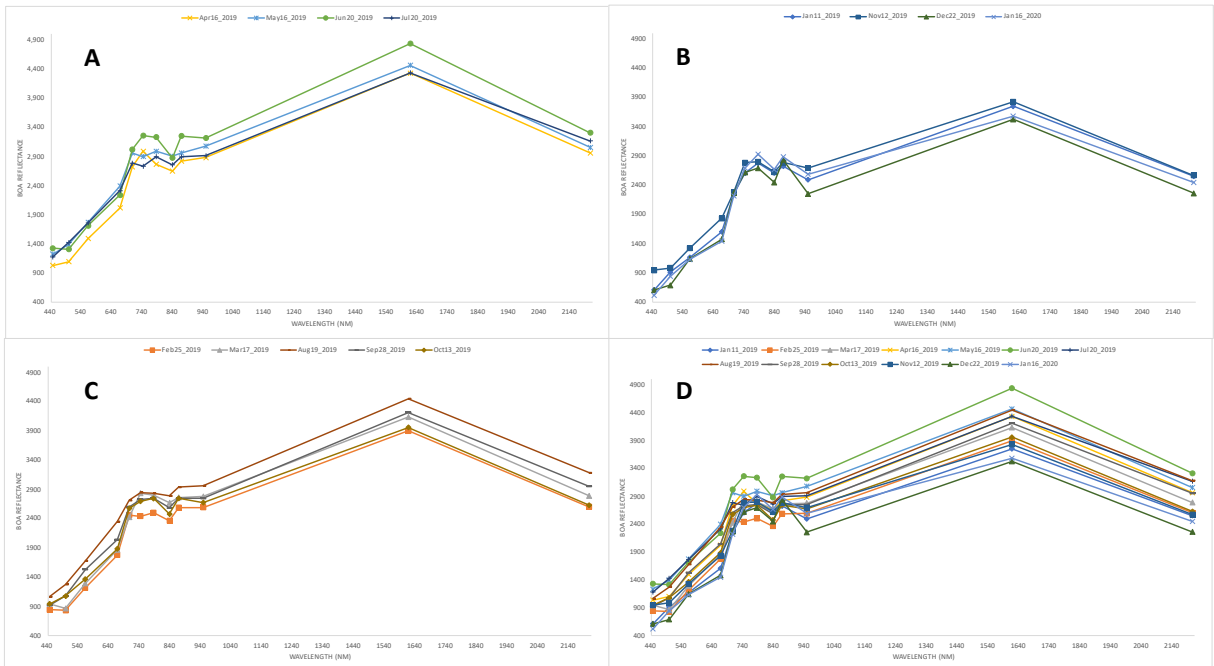


Figure 3.8: Spectral reflectance curves of mixed pixel 1 from different months. A shows the spectra from summer (April to July 2019), B shows spectra from winter months and C shows spectra from the other months. D shows one spectra each from all thirteen months. All spectra have been extracted from cloud free images.

3.2.2. Time Series on Band Ratios

Time series on band ratios (mentioned in table 2.2) were performed for all the selected pixels from all three classes – vegetation, pure geology, and mixed pixels. Results from some of the pixels will be shown in this section. For the vegetation pixels, an extended dataset from January 2018 to January 2020 was used with the date as the x-axis. For the rest pixels, the dataset with 40 images (January 2019 to January 2020) was used with the day (1-391) as the x-axis. Band ratios of pure geology pixels were expected to be (almost) constant over time, as geology does not change in short periods (thirteen months). Band ratios of vegetation and mixed pixels were expected to vary with seasons as the vegetation part of the pixel keeps varying with time.

Vegetation pixels had higher vegetation indices (NDVI, SAVI, and BR5) in winter and lower values in other seasons. NDVI and SAVI are normalized ratios, and the values vary between 0.6 to 0.2 (NDVI) and 0.5 to 0.1 (SAVI) for vegetation pixels. BR5 is a simple ratio involving B8 and B4, and its values vary between 3 and 1 (see table 2.2 for the formulae). As two years were included for vegetation pixels, fifth-order polynomial curves were used for fitting; for all the other time-series curves (with 13 months data), second-order polynomial curves were used.

The vegetation indices are the lowest in summer. Figure 3.9 shows the variation of NDVI (A), SAVI (B), and BR5 (C). Huge troughs could be observed in all three ratios (for example, on 1st January 2020), cloud cover causes these drops in band ratios, and these are outliers. Overall, all three band ratios vary similarly throughout the two years, with values high in winter and low in summer months.

For comparison with other band ratios, BR5 is used as a proxy for vegetation as values (of band ratios BR1, BR2, BR3, BR4, and BR5) lie in a similar range, and BR5 has a similar variation that of NDVI and SAVI.

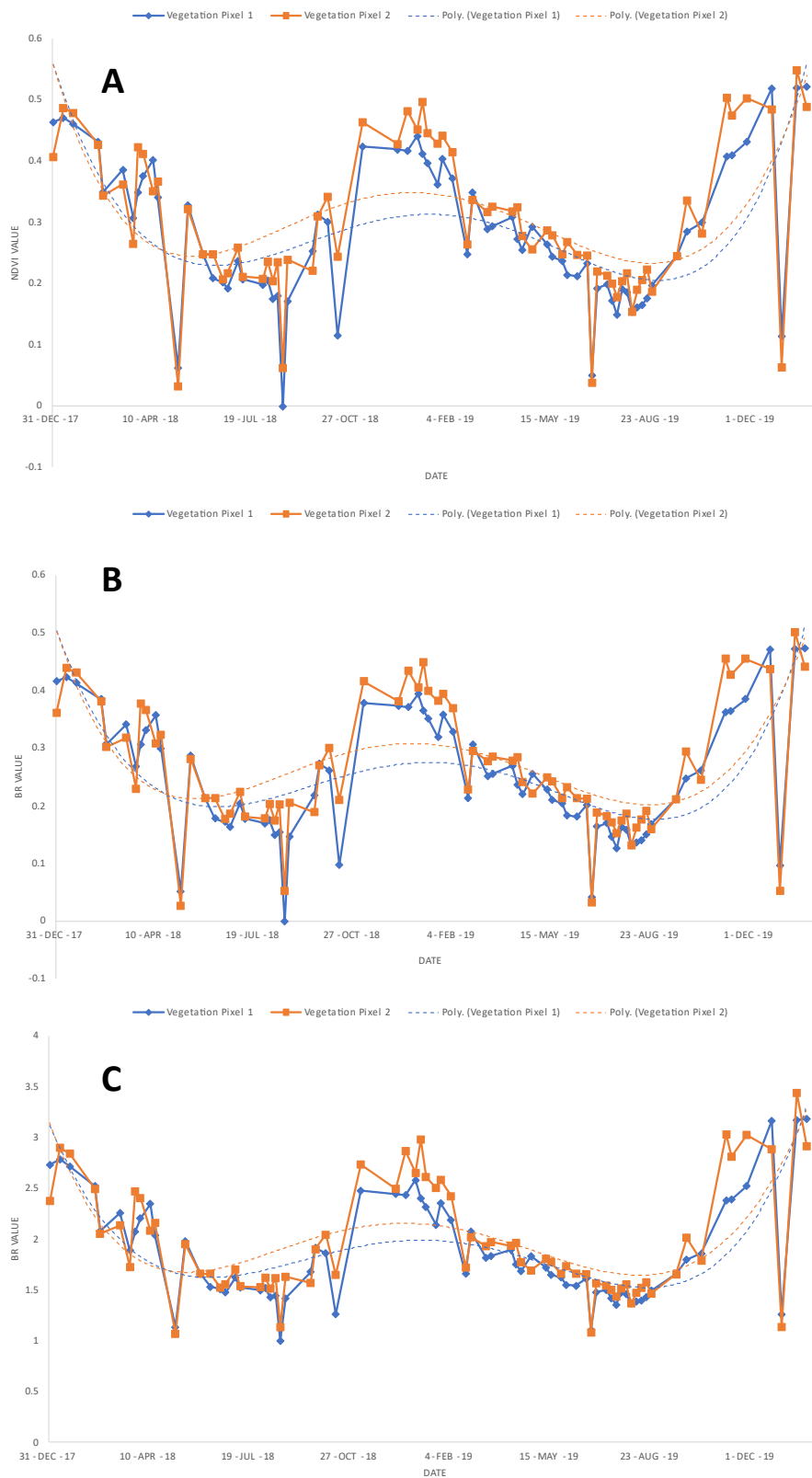


Figure 3.9: Band ratio time series of vegetation pixels for and extended dataset (Images from January 2018 to January 2020 were used). Blue curves (with diamonds as datapoints) shows the variation of band ratio values of vegetation pixel 1 and orange curves (with squares as data points) shows the variation of NDVI values of vegetation pixel 2. A shows NDVI time series, B shows SAVI time series, and C shows BR5 (B8/B4) time series.

Pure geology pixels had relatively similar band ratio values over time; all the band ratio values lie between 1.0 and 1.2 over the year with a few outliers due to cloud cover. No seasonal variations could be seen in the band ratio time series curves of the pure geology pixels. Time-series on spectra of all the selected geology pixels showed prominent features at 845 nm and 864 nm. To observe the variations in these features, band ratios BR3 (for 835 nm feature depth variation) and BR4 (for 864 nm feature depth variation) were defined. The time series on band ratios – BR3, BR4, and BR5 of pure geology pixel 1 is shown in figure 3.10. The band ratios were almost constant for pure geology pixel 1 (in the range of 1 to 1.1) throughout the image dataset. Specific outliers were observed on the days with cloud cover; for example, BR5 increases on 1st January – day 366 (see figure 3.10).

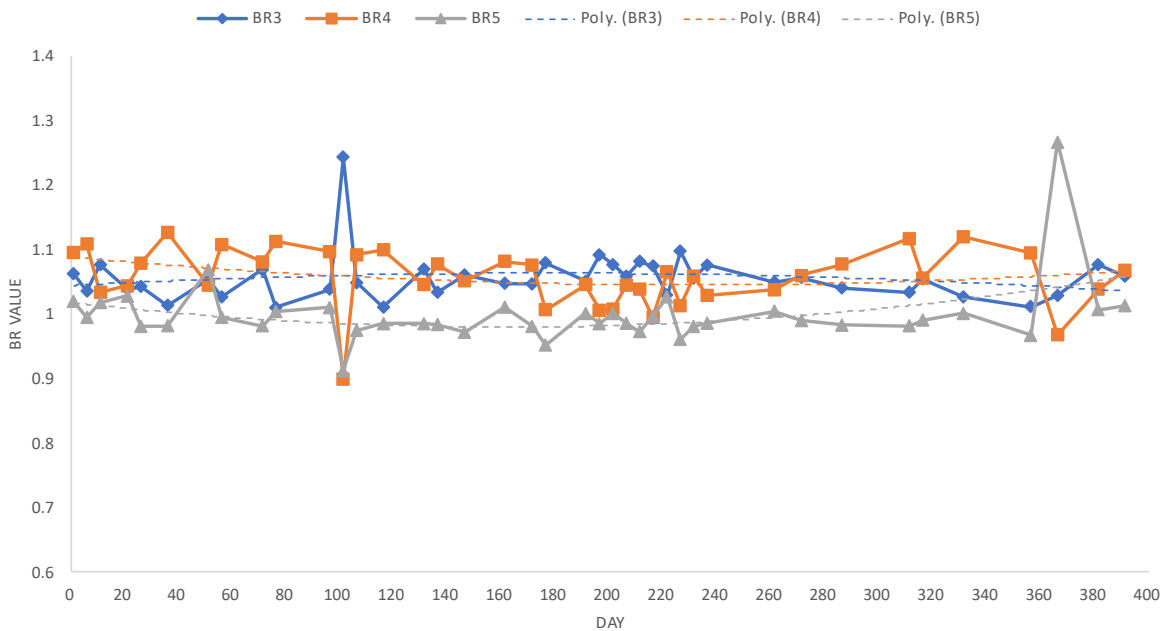


Figure 3.10: Time Series of band ratios from January 2019 to January 2020 (Day 1 to Day 391) of pure geology pixel 1. Blue curve (with diamonds as datapoints) is time series of BR3 (B7/B8), orange curve (with squares as datapoints) is time series of BR5 (B8/B4), and silver curve (with triangles as datapoints) is time series of BR4 (B8/B8A). BR value stands for band ratio value and x-axis is day number (0-391).

Band ratios of mixed pixels were expected to vary with seasons due to the vegetation part in the pixel. Band ratios BR3, BR4, and BR5, were used for the time series on mixed pixels to observe any relations between the feature depth variation and vegetation. Band ratios of the mixed pixels showed variations with seasons. For some pixels, the band ratio values were higher in winter, and they gradually decreased towards summer after which they gradually increased towards the next winter (figure 3.11); for some pixels, the variation was inverse with higher values in summer and low values in winter (figure 3.13).

For mixed pixel 3, the time series of band ratios shows a similarity in the variation of BR5 and BR3. Both BR3 and BR5 values are higher in winter and lowest in summer with a gradual decrease from winter to summer (January 2019 to July 2019) and a gradual increase from summer to the next winter (July 2019 to January 2020). Figure 3.11 shows the band ratio time series of mixed pixel 3. For mixed pixel 1, the time series of band ratios do not show a similarity in the variation of BR3 and BR5. BR3 values remained relatively constant (around 1.1) throughout the period (391 days), and BR5 values vary similarly to that of mixed pixel 3. Figure 3.12 shows the band ratio time series of mixed pixel 2.

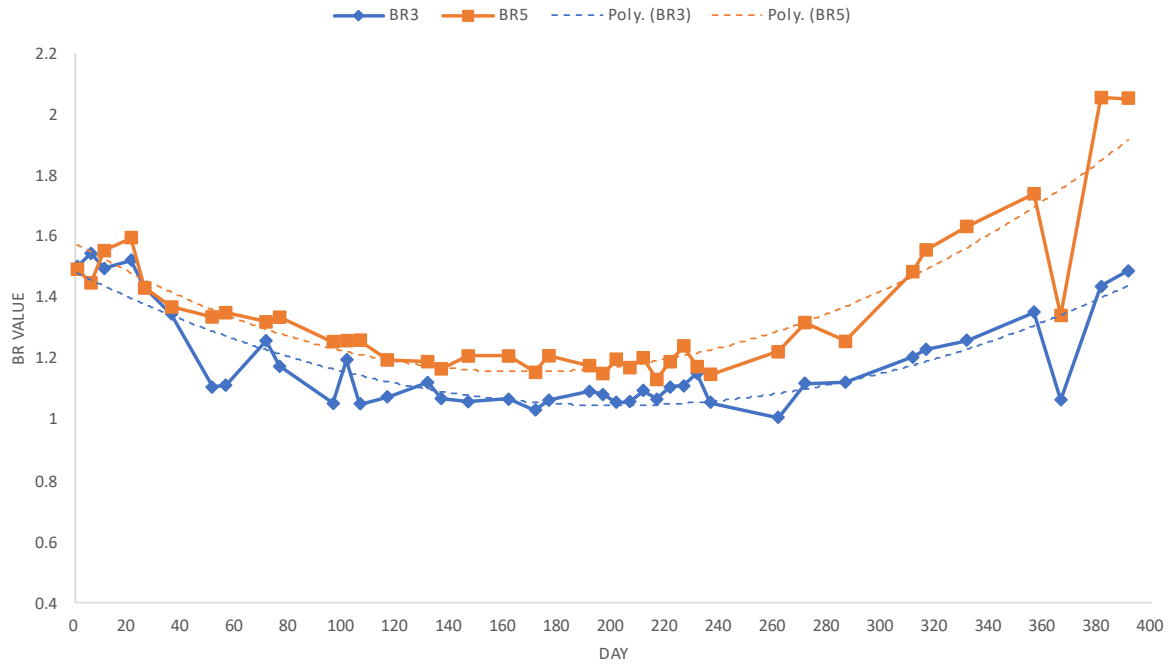


Figure 3.11: Time Series of band ratios from January 2019 to January 2020 (Day 1 to Day 391) of mixed pixel 3. Blue curve (with diamonds as datapoints) is time series of BR3 (B7/B8) and orange curve (with squares as datapoints) is time series of BR5 (B8/B4). BR value stands of band ratio value and x-axis is day number (0 -391).

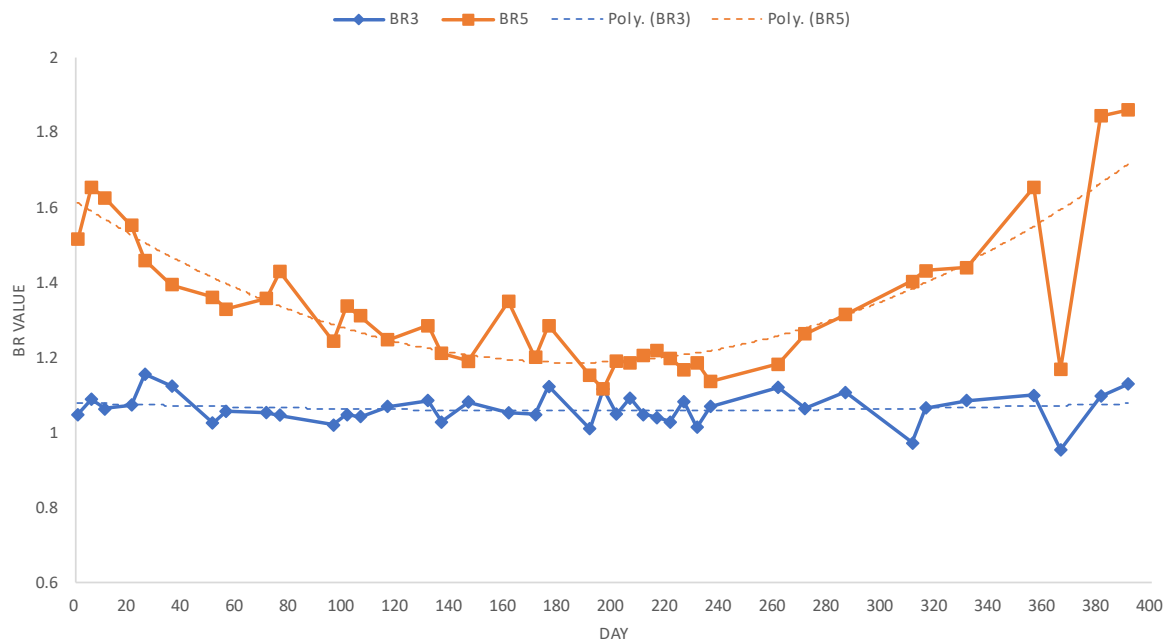


Figure 3.12: Time Series of band ratios from January 2019 to January 2020 (Day 1 to Day 391) of mixed pixel 1. Blue curve (with diamonds as datapoints) is time series of BR3 (B7/B8) and orange curve (with squares as datapoints) is time series of BR5 (B8/B4). BR value stands of band ratio value and x-axis is day number (0-391).

In mixed pixels, a feature was prominent in spectra from all months, and a relatively smaller feature could be seen only in summer months. Band ratio time series showed inversely related behavior of these features. Mixed pixel 2 is an example of this case, a feature at 835 nm was prominent in spectra from almost all months but a smaller feature at 864 nm could be observed in spectra extracted from summer images. In winter images, this feature was missing. Time series of band ratios – BR3, BR4 of mixed pixel 2 (figure 3.13) shows the feature(s) depth variation within the time period. When BR3 values are high (in winter), the values of BR4 are low, and when values of BR3 are low (in summer), the values of BR4 are high. The depth of the feature at 835 nm varies inversely to the depth of the feature at 864 nm (see figure 3.13).

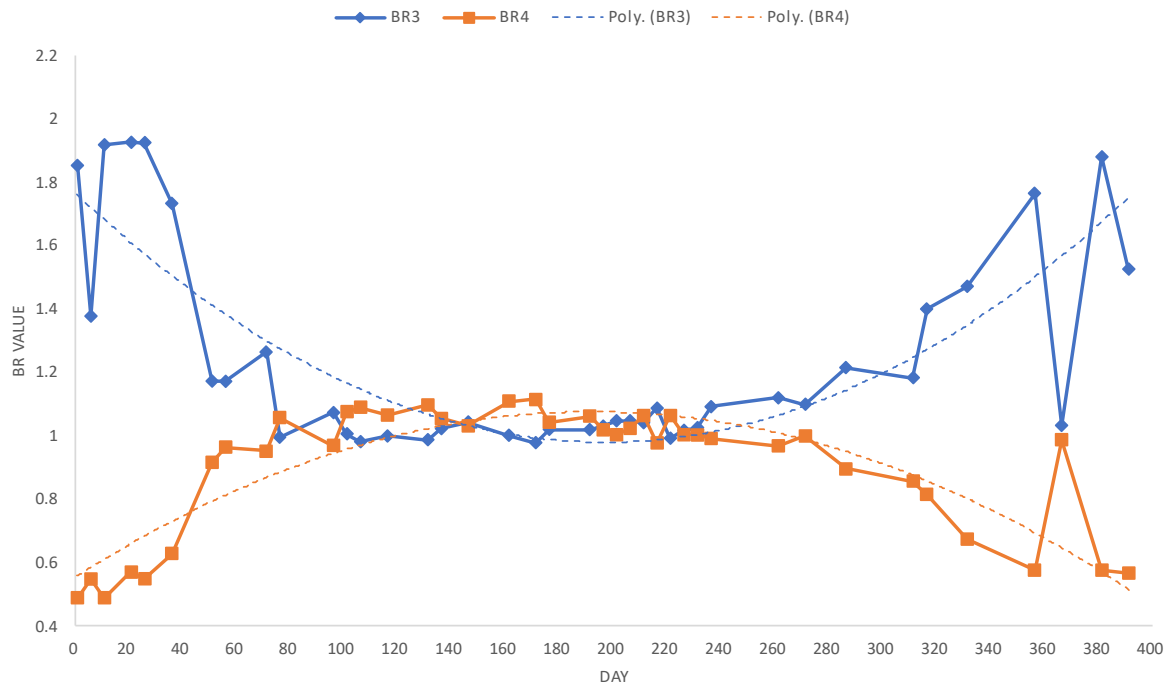


Figure 3.13: Time Series of band ratios from January 2019 to January 2020 (Day 1 to Day 391) of mixed pixel 2. Blue curve (with diamonds as datapoints) is time series of BR3 (B7/B8) and orange curve (with squares as datapoints) is time series of BR4 (B8/B8A). BR value stands of band ratio value and x-axis is day number (0-391).

3.2.3. Time Series on individual bands

Spectra of pure geology pixels showed variations in the 700 to 900 nm wavelength region. Time series on particular bands – B5 (703.9 nm), B6 (740.2 nm), B7 (782.5 nm), B8 (835.1 nm), and B8A (864.8 nm) was performed on vegetation, pure geology, and mixed pixels, to see if there is any relation between the trends. B5, B6, B7, B8A are red-edge bands, and B8 is a Near-Infrared band (see table 2.1 in 2.2). Figure 3.14 (A) shows the variation of the bottom of the atmosphere (BOA) reflectance values for vegetation pixel 1. The reflectance values continuously increase from January 2019 to July 2019, after which they slightly decrease for all the bands, but B5 has a higher contrast throughout the year. Figure 3.14 (B) shows the variation of BOA reflectance values for pure geology pixel 1. The reflectance values continuously decrease from January 2019 to July 2019, after which they slightly increase towards January 2020. There is a massive trough (sudden drop from 5000 to 2000) in the curves on 1st January 2020, which is due to cloud cover (see figure 3.14 (B)). For mixed pixels, the BOA reflectance values for individual bands are low in winter and increase towards summer after which they decrease again. Figure 3.14 (C) shows the variation of reflectance values

for mixed pixel 3. The values start relatively low between 1000 and 1500 in January 2019 and increase to 3000 in June 2019 and then fall back to 1000 – 1500. The reflectance values of pure geology pixels vary inversely to that of mixed and vegetation pixels. Vegetation and mixed pixels have a similar variation, with the vegetation pixel having a relatively flatter curve (see figure 3.14).

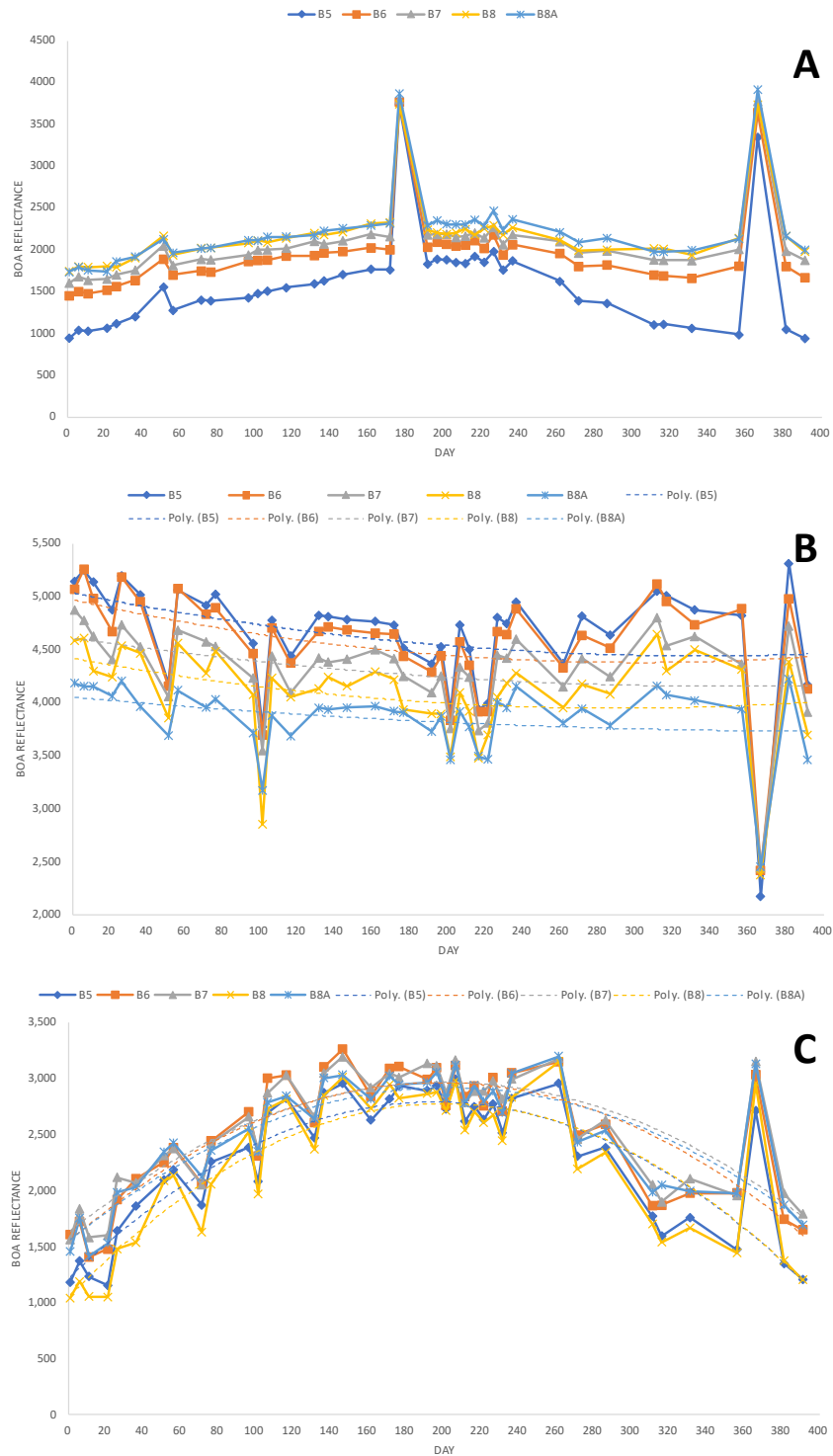


Figure 3.14: Variation of Bottom of Atmosphere Reflectance values of vegetation pixel 1 (A), pure geology pixel 1 (B), and mixed pixel 3 (C) from bands 5, 6, 7, 8 and 8A. All 40 images were used. Outliers (peaks & troughs) are due to cloudy images (February 20th, 2019 – day 51, June 25th 2019 – day 176, and, January 1st, 2020 – day 366).

3.3. Influence of Shadow and Clouds

Images with cloud and shadows were deliberately included in the dataset to see if retrieving signals from the underlying objects is possible by looking in time. One of the objectives of this research is to try to improve image selection methods for GRS studies. Generally, clouds and shadows are one of the significant criteria during the image selection process. In the process of trying to assess the possibilities of using spectra as a metric for selecting images, the influence of these criteria on spectra was studied.

3.3.1. Shadow

The presence of mountains in the study makes it a region prone to shadows. Time-lapse visualization of true-color imagery showed the presence of shadows in winter, which gradually decrease towards summer. A pixel with shadows was included to observe its effect on the spectra of the underlying object. The study area has evaporite mountains (see figure 3.15), where shadows occur due to elevation differences. Figure 3.16 shows the variation of shadows in the mountains, and the yellow pointer represents the pixel. Shadows can only be seen in the winter months for this particular area. Large shadows can be seen in January, and February, after which they reduce from March to October (see figure 3.16).

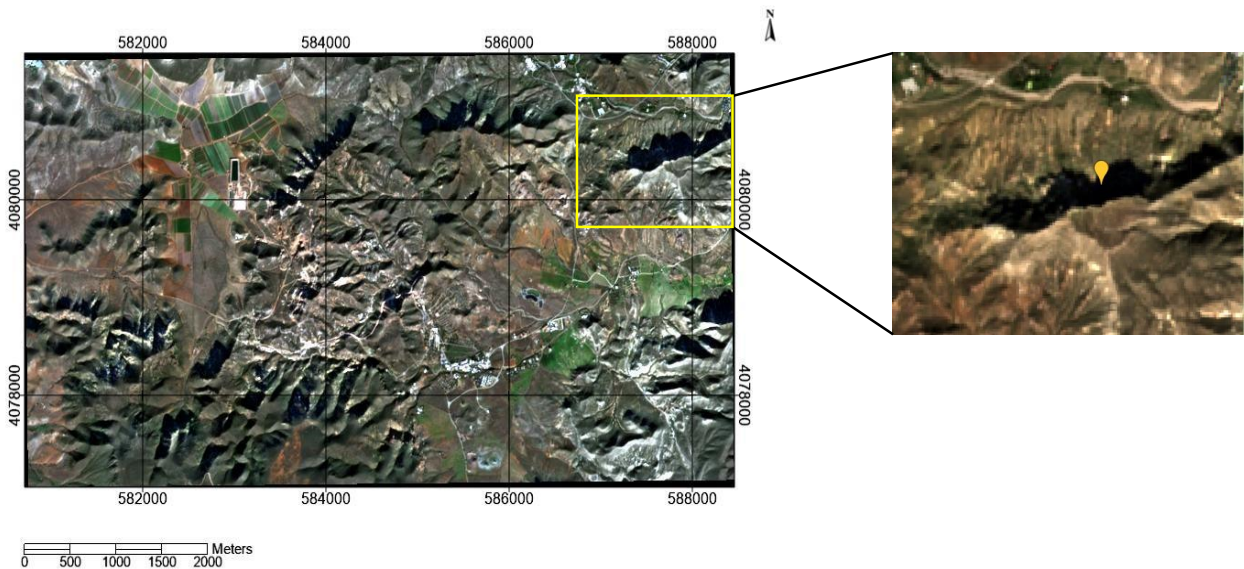


Figure 3.15: Image showing the location of geo pixel 21 in the study area. The highlighted area is an evaporite mountain with shadows in the winter months. Yellow pointer shows the location of the pixel. Image is a false color composite from January 1st, 2019.

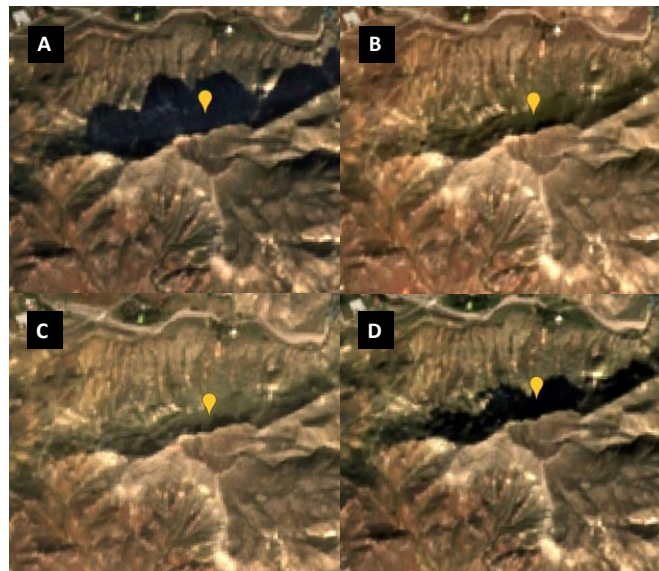


Figure 3.16: False color composite visualizations of the evaporite mountain with varying shadows. Yellow pointer shows the location of Geo Pixel 21. A is from January 11, 2019; B is from March 17, 2019; C is from October 13, 2019; D is from November 7, 2019.

The variation in spectra due to the presence of shadow can be seen in figure 3.17. In months when there is a shadow, low reflectance values can be seen in all the bands. Some of the features in the 700 nm to 900 nm wavelength range can still be observed (see figure 3.17).

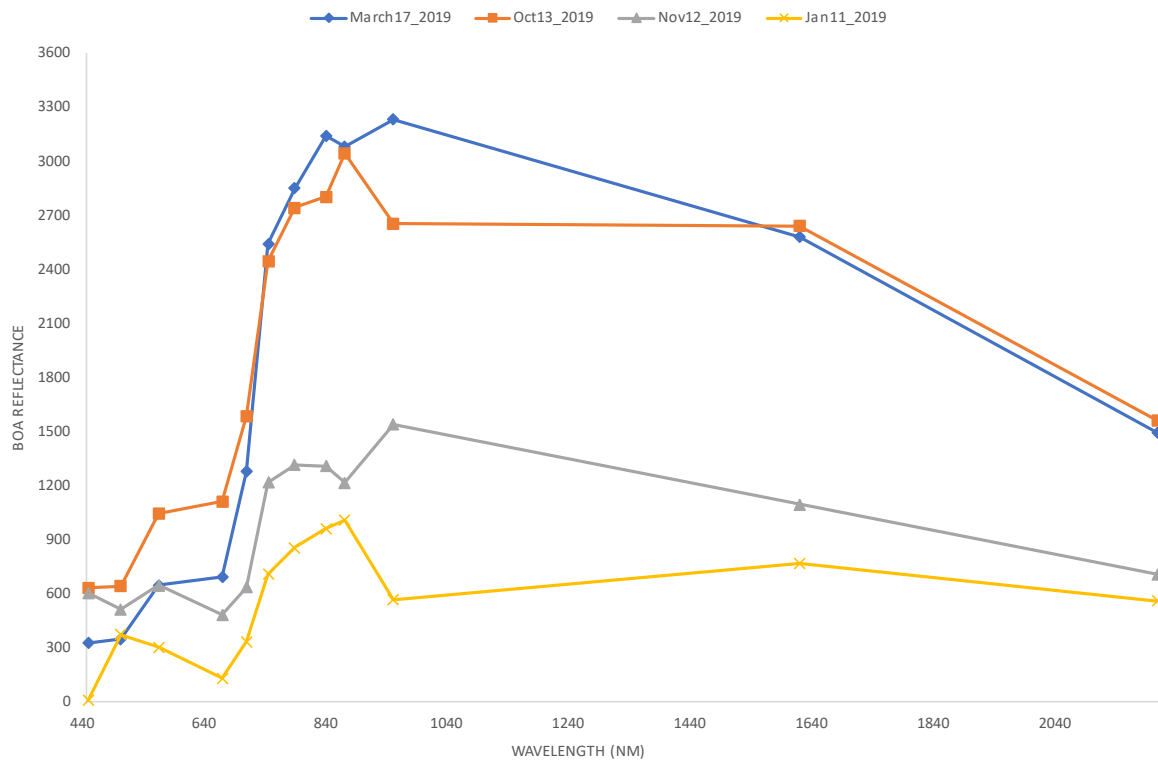


Figure 3.17: Variation in Spectra of Geo Pixel 21 due to shadows. Image shows low reflectance values in months with shadows.

3.3.2. Cloud cover

Images with cloud cover were included in the dataset to observe the effects of cloud on spectra of the underlying geology object. Spectra extracted from imagery with and without clouds of pure geo pixel 2 and mixed pixel 1 were compared. Winter months are cloudy in this study area; as a result, a lower number of cloud-free images in winter were available.

On 1st January 2020, most of the study area was covered in clouds. Mixed pixel 1 was covered in dense clouds, and pure geology pixel 2 was covered in shadow due to the cloud. Pure geology pixel 2 has similar spectra in all seasons (see figure 3.18). For this pixel, the reflectance values dropped drastically due to the presence of clouds when compared with spectra from other months. An absorption feature at 835 nm could be seen, which is not present in spectra from any other month. Mixed pixel 1 has a consistent absorption feature at 835 nm (see figure 3.19 or figure 3.8 for spectra from all months). Due to dense clouds, the reflectance values increased in comparison with spectra from other months. The feature which was consistent in all months at 835 nm is missing in the spectra extracted from the 1st January 2020 image.

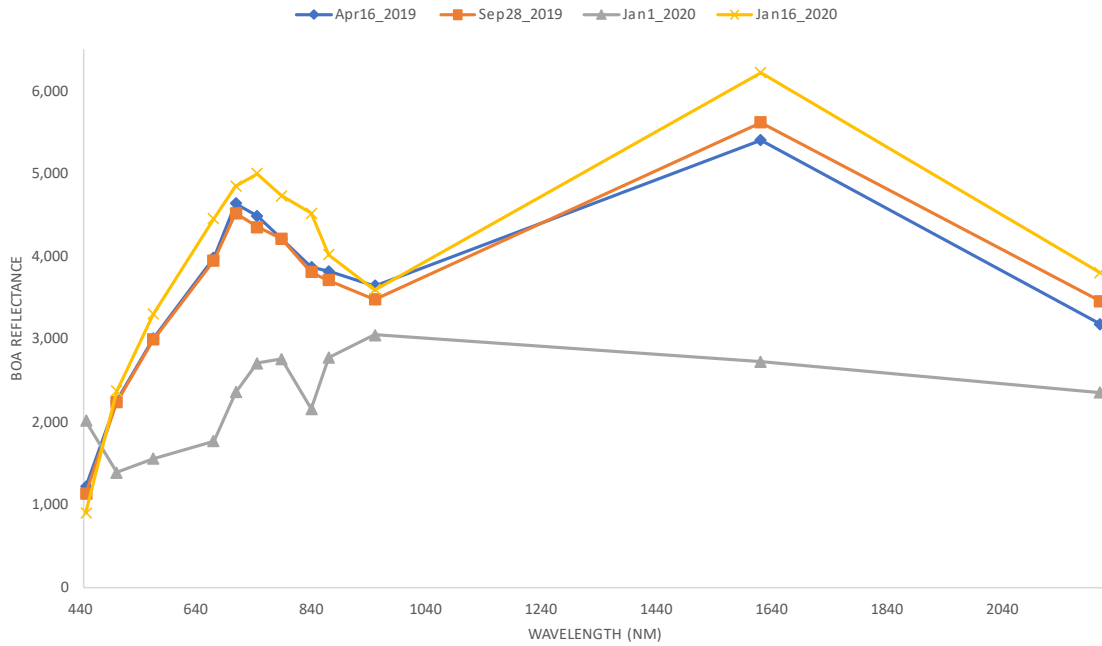


Figure 3.18: Variation in spectra of geo pixel 3 due to cloud cover. Geo Pixel 3 is a pure geology pixel. The pixel was covered in shadow due to cloud. Spectra from all seasons were included for comparison. January 1st, 2020 (image number 366) image contained cloud cover. The spectra from January 1st, 2020 can be seen at the bottom.

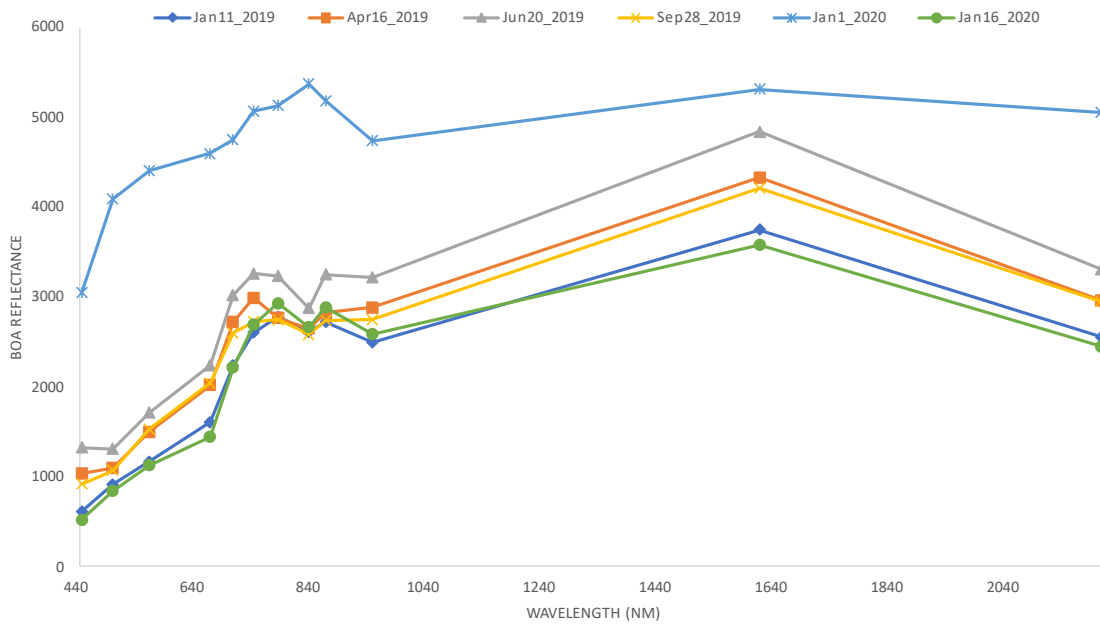


Figure 3.19: Variation in spectra of geo pixel 4 due to cloud cover. Geo Pixel 4 is a mixed pixel. The pixel was covered in cloud cover. Spectra from all seasons were included for comparison. January 1st, 2020 (image number 366) image contained cloud cover. The spectra from January 1st, 2020 can be seen at the top.

4. DISCUSSION

This research evaluates the abilities of using time component in tackling vegetation cover in geological remote sensing of Sentinel-2 imagery. Forty Sentinel-2 (level 2A) images over Rodalquilar from January 2019 to January 2020, covering all the seasons, were used in this research. The study area was visually inspected using Google Earth Imagery, true-color composites of Sentinel-2 imagery, and time-lapses based on true-color composites to determine potential areas of interest. Various pixels were then selected from the areas of interest using band ratios; these pixels were then classified into 'pure geology,' 'vegetation' and 'mixed' pixels. Time series analysis was performed on the spectra and band ratios of the selected pixels to observe how pixels from the different classes vary over time.

Vegetation changes over a year, but geology does not change in such short periods. Results from the time series on the selected pixels are in line with this fact. Spectra from vegetation pixels (figure 3.5) and mixed pixels (figure 3.7) show variations with seasons and cluster into three groups. Spectra from these two classes consisted of absorption features with varying depths; features were deeper in winter and shallow in summer. Vegetation features are more prominent in winter; band ratios used as proxies for vegetation – NDVI, SAVI, and BR5 also have higher values in winter (figure 3.9). The variation in depth of features in mixed pixels was in line with the variation in vegetation indices (NDVI, SAVI, and BR5). Spectra from pure geology pixels (figure 3.6) do not show any seasonal variations, and no clusters (such as spectra from winter forming a cluster, and spectra from summer forming another cluster) were seen. Pure geology pixels had absorption features consistently throughout the thirteen months. The depth of these features was relatively constant from January 2019 to 20th January.

In mixed pixels, prominent features were present, and the depths of these features varied throughout the 40 images. In some cases, a relatively smaller feature was present only in summer. Time series analysis was performed on band ratios, which determined the depth of these features. The time series shows that the depth of more prominent features (present in almost all images) decreased from winter to summer and then increased again from summer to winter. The depth of relatively shallower features increased from winter to summer and then decreased from summer to winter. This can be seen in the case of mixed pixel 2 (see figure 3.13). In some mixed pixels, there were features with relatively constant feature depths and no seasonal variations, similar to features from pure geology pixels. For example, mixed pixel 1 has a feature at 835 nm, which has a depth in the range of 0.9 - 1.1 (see figure 3.12).

Some images with clouds were left to be in the dataset deliberately to study the influence of cloud cover. The presence of clouds resulted in abnormal peaks and troughs in some of the time series charts; these outliers might have caused overfitting in some cases. Also, no cloud masking methods were used, as it might result in loss of information regarding the underlying object. Sentinel-2 level 2A imagery was used in this research, and no additional atmospheric corrections were performed.

Pixel Selection was performed based on band ratio statistics values, and visual inspection. Pixels were selected based on the fact that vegetation changes in short periods, but geology pixels do not change in such intervals and mixtures due to vegetation lie in between. The selected pixels were classified as pure and mixed geology pixels based on the trends of NDVI and SAVI. NDVI and SAVI values varied over time in small ranges, such as 0.1 to 0.2. The trends were also affected by the presence of a cloud, which resulted in overfitting. Therefore, the visual inspection also had to be included in the process of classifying the pixels.

The final classification decision was taken manually, combining band ratio variation curves, band ratio statistics, and visual inspection.

Generally, one would expect the vegetation to be greener in spring than in autumn or winter and, therefore, select images from other seasons to reduce the influence of vegetation for GRS studies. However, time series on vegetation pixels suggests a green peak in winter for this study area. The features in vegetation spectra are relatively deeper in spectra extracted from winter images. Vegetation indices (NDVI, SAVI, and BR5) also have a trend, where their values are high in winter and low in summer. The vegetation indices start high in January 2018 and decrease towards June – July 2018; they then increase towards December 2018. This trend is prevalent over the years. Figure 3.9 shows this trend for vegetation pixels – 1 and 2. Van Der Werff et al. (2018), in their study, carried out time-series on band ratios for rodalquilar (images from 2015 to 2017). Their research also shows similar results; the NDVI trends from 2015 to 2017 suggest winter as the green season (Van Der Werff et al., 2018b).

Geological objects such as rocks, outcrops, soil surfaces do not change so quickly in time. With the objects not changing in time, we expect their spectra also not to change. Time series on spectra of pure geology pixels shows variations in time. Although the spectra do not show any seasonal variations, changes in the 700 to 900 nm wavelength region can be seen (see figure 3.6). This wavelength region is one of the target regions in mineralogical mapping studies with Sentinel-2, as it is prone to features from iron-bearing minerals. With the spectra being sensed remotely, factors such as weather, illumination, and atmospheric conditions play a role. Figure 3.6 (C) shows the variation of spectra from pure pixel 1 in January; the dataset contained five images (1st, 6th, 11th, 21st, and 26th) from January and no two spectra from consecutive days had a similar shape in the 700 to 900 nm region. These slight variations might be due to different illumination or atmospheric conditions. Time series on individual bands from this region was performed, results show a trend where the reflectance values of all the bands (in this region) decrease from winter to summer and then increase from summer to winter (figure 3.14 (B)). This trend is in contrast with the trends of individual bands of vegetation and mixed pixels. For pure geology pixels, the values lie between 4000 and 5000, and a trend with values decreasing from winter to summer can be seen. In vegetation, the values lie between 1000 to 2000, and a trend with values increasing from winter to summer can be seen. In mixed pixels, the values vary between 1000 to 3000 with a trend similar to vegetation, but a relatively higher contrast. In summer, the reflectance values in pure geology pixels and mixed pixels lie in the range of 3000 to 3500. In mixed and vegetation pixels, variations are because when vegetation is in its peak, relatively lower radiation reaches the object beneath and vice versa. Therefore in mixed pixels, during summer, the reflectance values are relatively higher as they are being reflected from the objects beneath.

The objective of this research is to identify the influence of vegetation on the spectra of geology objects using the temporal dimension. Time series analysis of mixed pixels tackles this objective. The time series on mixed pixels showed the presence of prominent features (similar to pure geology pixels); some of these features kept varying with seasons, while some did not for some mixed pixels. For example, in mixed pixel 1, a feature at 835 nm could be observed (figure 3.8), and the depth of this feature remained almost constant throughout the year (figure 3.12). In mixed pixel 3, the same feature had varying depths (figure 3.7); a comparison of BR3 (feature depth at 835 nm) and BR5 (a proxy for vegetation) shows that they have similar trends. Both the band ratios have higher values in winter, and a decreasing trend from winter to summer (figure 3.11). Vegetation changes occur with seasons, and features due to vegetation also vary with seasons. Geology does not change with seasons, and its feature remains relatively similar throughout the year, which should result in a constant feature depth. Therefore features with varying absorption depth (such as the

feature at 835 nm in mixed pixel 3) are caused due to the vegetation part of the pixel and features with constant absorption depth (such as the feature at 835 nm in mixed pixel 1) are from the geology part of the pixel. A comparison of the absorption depth of features due to vegetation and geology parts in a mixed pixel is shown in figure 4.1. A clear contrast can be seen in the trends of the feature depth variation in the two pixels. This region (800-900nm) is known for features in iron-bearing minerals, and features due to vegetation (like in mixed pixel 3) will result in false positives in studies where time is not considered. In some mixed pixels (for example, mixed pixel 2), apart from a feature that was present in all seasons, an additional feature was spotted only in peak summer. The feature was relatively smaller in comparison with the feature present in all images. The depth of the absorption features varied inverse to each other (see figure 3.13). The depth of the feature at 835 nm (present in almost all images) has a trend similar to that of vegetation, i.e., higher values in winter and decreasing from winter to summer and then increasing from summer to winter again. The smaller feature's (at 864 nm) depth was higher in summer and lower in winter

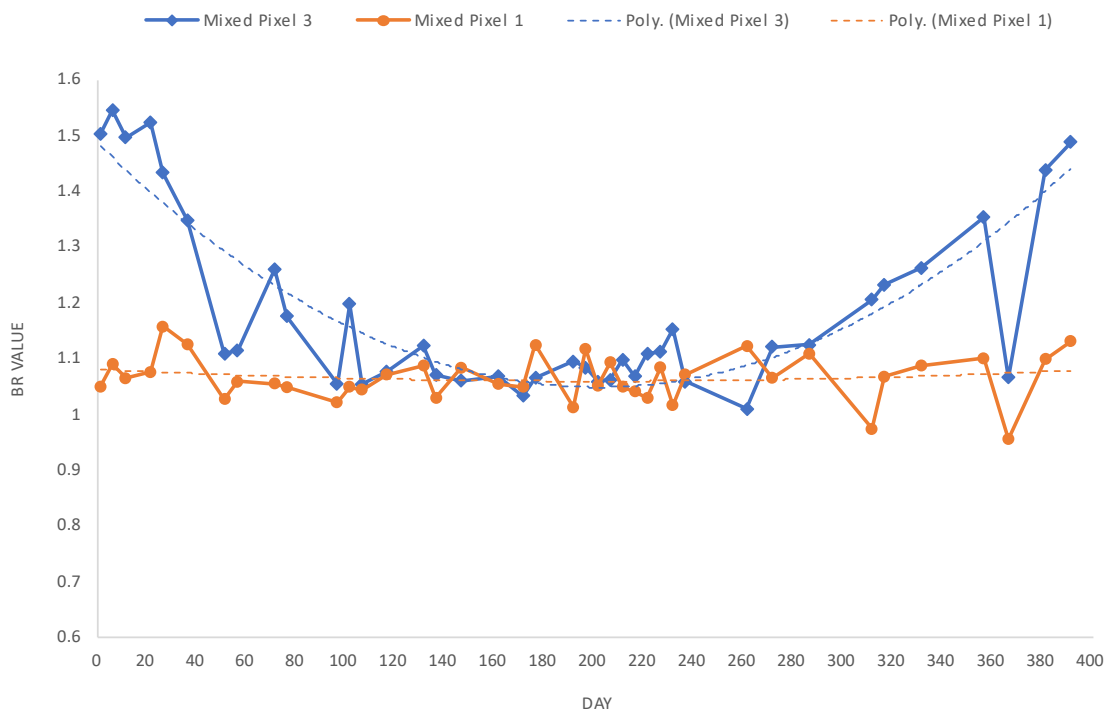


Figure 4.1: Comparison of variation of absorption depth feature at 835 nm (BR3) for mixed pixel 1 (orange curve with circles as datapoints) and mixed pixel 3 (blue curve with diamonds as datapoints). BR value stands for band ratio value.

(see figure 3.13). In this case, the feature from the vegetation part of the pixel might be influencing the relatively smaller feature. When vegetation is not the greenest in summer, this feature can be seen in spectra. In all the other seasons, the smaller feature seems to be missing as the feature at 835 nm dominates.

Overall, the influence of vegetation could be observed in the time series on mixtures with vegetation. The time series on spectra resulted in clusters for mixed pixels based on seasons. The band ratios followed a trend similar to vegetation; features due to vegetation could be identified. The time series on individual bands also resulted in similar trends for vegetation and mixed pixels. Although seasonal variations could be seen in most mixed pixels, spectra of some did not relatively change over time (for example, mixed pixel 1). The NDVI and SAVI mean of mixed pixel 1 was 0.141 and 0.12 respectively, and their time-series curves show seasonal variation. The spectra of this pixel did not cluster into groups (see figure 3.8). This might be

due to a lower fraction of vegetation part in the pixel; however, proportions in mixtures were not explored in this thesis. The variations in vegetation indices seem to be varying differently within mixed pixels, i.e., some pixels have trends closer to vegetation while some pixels have trends closer to geology pixels (for example Geo pixel 13 (closer to pure geology) vs. Geo Pixel 14 (closer to vegetation); see figure 7.2 in appendix section 7.2). It might be interesting to see if proportions in mixtures can be defined using band ratios.

Generally, in GRS studies, NDVI is used to mask out pixels; for example, in van der Werff & van der Meer, (2015) pixels with NDVI values outside the range 0.0 - 0.3 were masked out. During pixel selection, pixels with relatively lesser values (around 0.15) were selected as mixtures with vegetation. In most other studies, these pixels might be considered as bare pixels; however, the seasonal variation in NDVI values for these pixels seems to be in line with vegetation. These pixels being considered as bare or pure geology pixels might result in misinterpretation of vegetation features (in the 700 to 900 nm region) as features due to the presence of geology objects. In studies involving masking out vegetation pixels based on NDVI values, there are possibilities for mixed pixels (mixtures with vegetation) to be masked out; in other cases, mixtures are dealt with complicated spectral unmixing techniques (Bierwirth, 1990; Clasen et al., 2015). Time series analysis results show potential in dealing with mixtures using band ratios, and signals from different parts in mixed pixels could be identified.

Images with clouds and shadows were also included to observe their influence on the spectra of the underlying geology object. In this region, shadows and clouds are common in winter images (figure 3.16). The presence of shadows resulted in lower reflectance values; the features could still be spotted despite the presence of shadows (figure 3.17). The presence of cloud cover results in either high reflectance values (thick clouds) or low reflectance values (mostly due to the shadows from the cloud). With cloud cover, the features present in spectra from other months were missing. In both cases, thick clouds, thin and shadow due to clouds, the information seems to be lost. In all the band ratio products and time series products, the influence of clouds could be easily identified, as they result in abnormal peaks or troughs (see figures 3.9, 3.13, 3.14; day 366 (1st January 2020)). With clouds, the features seem to be missing completely; time series analysis does not help in retrieving information of the underlying object as the object is not being sensed.

The influence of weather, illumination, and atmospheric conditions, etc., was not considered in this research as the focus was on vegetation cover. It was assumed that atmospheric correction deals with the variation in atmospheric conditions to an extent. No atmospheric methods are perfect; however, studies involving Sentinel 2 imagery did not mention any problems with atmospheric corrections (Clasen et al., 2015; Sibanda et al., 2015; van der Werff & van der Meer, 2016). Some of the changes in the spectra of geological objects (for example, the variations in 700 to 900 nm region in pure geology pixels; see figure 3.6) might be due to change in weather conditions, as these variations occur faster than changes in vegetation. These variations could be observed within one month; in pure geology pixel 1, no two spectra from consecutive days had a similar shape in this region in January 2019 (see figure 3.6 D).

5. CONCLUSIONS AND RECOMMENDATIONS

This research observed the changes in remotely sensed spectra of geological objects caused by natural vegetation over a period of thirteen months to understand the level of information that can be retrieved from the changing spectral signatures of the not so changing objects. Pixels were selected from the classes – vegetation, pure geology, and mixed. Google Earth imagery, Sentinel-2 true color composites, band ratio statistics, and trends of vegetation indices were used to select and classify the pixels. Time series analysis was then performed on the selected pixels, to study the variations in their spectra, band ratios, and reflectance values of individual bands.

What effect do changes in seasonality and growth cycle have on spectral signatures of natural vegetation over time? The impact of seasonality on spectral signatures of natural vegetation seems to be varying with geographic location and climate zone. For Rodalquilar, vegetation is greener in winter and has a trend which reduces from winter to summer; natural vegetation is relatively greener in January, February, October, November, and December in this region. The values of vegetation indices are the lowest in June and July.

Do remotely-sensed spectra of geological objects change over time? Yes, spectra of geological objects (pure geology pixels) undergo variations over time. In most cases, the spectra from different days have consistent features and have slight variations in the 700 to 900 nm wavelength region. These changes are due to differences in atmospheric or illumination conditions.

How to optimally classify ground cover such that there are either pure or mixed pixels by using spectral indices? Band ratios can be used to select and classify pixels into pure and mixed geology pixels. Pure geology pixels do not undergo any changes in short intervals, but in mixed (with vegetation) pixels, the vegetation part keeps varying with time. Using band ratio time-series curves helps in differentiating between the pure and mixed pixels. Comparing the variation of spectral indices from geology pixels with that of natural vegetation helps in optimally classifying the geology pixels.

How do the spectra of mixed geological objects change in time? Is it possible to identify the signal resulting from the geological objects and vegetation parts present in the pixel? Changes in mixed pixels are mostly due to the presence of vegetation (weather, atmospheric and illumination conditions have a minor effect, for example, slight variations in the 700 to 900 nm region), as the geology part of the pixel does not change in short periods. Variations in spectra and band ratios of mixed pixels are similar to that of vegetation pixels. The trends in the variation of band ratios of mixed and vegetation pixels are identical. Identifying signals resulting from vegetation and geology parts of the mixed pixel is possible. Features (signal) from the vegetation part varies with time, and features due to geology do not change. If the variation in absorption feature depth is in line with the trends of vegetation indices, the feature is from the vegetation part of the pixel. Although, in most cases, the depth of features from geology does not change, in some cases, vegetation features overshadow the geology features. In any case, by visualizing the band ratio variation over time, the features and the influence of vegetation can be identified.

Can image spectra be used as a metric for image selection in surface mineralogical mapping applications? Generally, images for GRS studies are selected based on the presence of cloud cover and illumination conditions. Vegetation is assumed to be relatively less green in summer, and images from summer are preferred. Alternatively, spectra can be used as a metric in image selection. The variation of band ratios or spectral indices of natural vegetation pixels in the region would help in understanding the time of the year when the influence of vegetation is the least and when the effect of illumination is the least etc. There might

be cases where the impact of vegetation is relatively less in a partially cloudy image in comparison with a cloud-free image.

This research assessed the viability of using time in the analysis of remotely sensed spectra for exploring the impact of vegetation. Looking in time helps in identifying features due to vegetation in mixed pixels, and the influence of vegetation on geology objects in mixed pixels. Adding the paradigm of time into GRS has several advantages; results from this research show multiple possibilities of misinterpretations with GRS studies using one or two images. Although geology does not change in a month or a year, spectra from geology objects change with time; these changes occur due to the presence of vegetation, variations in weather, atmospheric, and illumination conditions. The presence of features due to vegetation and iron minerals in the same wavelength range (around 900nm) results in false positives in mixed pixels with relatively low vegetation indices; these pixels are considered bare or pure in many GRS studies which means, these false positives would be misinterpreted. Looking in time is the only way to get rid of such false positives and improve surface mineral mapping methods.

Traditional GRS approaches involve masking out pixels with high vegetation indices, during which mixtures with vegetation also are removed. Spectral unmixing techniques are used in dealing with mixtures, but these sophisticated methods have their limitations. Looking in time has the potential to deal with mixtures and identifying features with relatively simpler band ratioing techniques. GRS studies consider that spectra of geology objects do not vary with time, as geology does not change with time. However, variations in the atmosphere, weather changes, changes in shadows, vegetation, etc., result in changes of even pure geology spectra. Mixtures vary with time, depending on their constituting parts. Overall, multi-temporal remote sensing will improve surface mapping capabilities when combined with techniques used in GRS.

5.1. Recommendations

In most GRS studies, one or two images are selected from summer, where the influence of vegetation is expected to be the least. However, the pattern of vegetation greenness seems to be different for different regions. A time series on vegetation indices will provide a basic understanding of the trends of vegetation for the particular area, which would improve the selection of images.

In this research, several pixels were analyzed over time. During this process, many pixels with abnormally high (and low) reflectance values and band ratios were spotted. This misbehavior in spectra relates to many factors, such as – complex topography, presence of small shadows, human activities in the pixel, inaccuracies in atmospheric corrections, etc. In cases when a single image is used, these abnormal values do not stand out and appear to be normal. Looking in time helps in overcoming such misbehavior and avoiding possible misinterpretations.

Time series on mixed pixels suggests that differentiating between features from vegetation and geology parts of the mixture is possible by looking in time. The influence of vegetation in mixed pixels was observed to be high in winter and low in summer. With the traditional approach in Geological Remote Sensing, there is a possibility of misinterpreting the signal from the vegetation part as a signal from the geology object, as the wavelength region is prone to features from both classes. Using band ratio variation over time will remove the possibility of any such misinterpretation.

With the availability of frequent Sentinel-2 Imagery, looking in time in Geological Remote Sensing studies is possible. Accessing the imagery is also made easier with the advent of cloud and server-based technologies

(for example – Google Earth Engine). Looking in time will not only improve image selection but also help in dealing with mixed pixels. A hyperspectral satellite sensor (Copernicus Hyperspectral Imaging Mission for the Environment - CHIME) is expected to be launched by the European Space Agency in the future (mid-2020's) with characteristics such as spatial resolution and revisit-time in line with Sentinel-2 (Mueller, 2019). A successful launch of CHIME would make looking in time possible. Adding the dimension of time to GRS studies with hyperspectral imagery will improve the capabilities to observe and study the influence of vegetation on geology objects.

6. LIST OF REFERENCES

- Abrams, M. (2000). The Advanced Spaceborne Thermal Emission and Reflection Radiometer (ASTER): Data products for the high spatial resolution imager on NASA's Terra platform. *International Journal of Remote Sensing*, 21(5), 847–859. <https://doi.org/10.1080/014311600210326>
- Abrams, M., & Hook, S. J. (1998). I 10.4-12.5, 33(3), 692–699.
- Abrams, M., Tsu, H., Hulley, G., Iwao, K., Pieri, D., Cudahy, T., & Kargel, J. (2015). The Advanced Spaceborne Thermal Emission and Reflection Radiometer (ASTER) after fifteen years: Review of global products. *International Journal of Applied Earth Observation and Geoinformation*, 38, 292–301. <https://doi.org/10.1016/j.jag.2015.01.013>
- Abrams, M., & Yamaguchi, Y. (2019, June 1). Twenty years of ASTER contributions to lithologic mapping and mineral exploration. *Remote Sensing*. MDPI AG. <https://doi.org/10.3390/rs11111394>
- Ager, C. M., & Milton, N. M. (1987). Spectral reflectance of lichens and their effects on the reflectance of rock substrates. *GEOPHYSICS*, 52(7), 898–906. <https://doi.org/10.1190/1.1442360>
- Al-Nahmi, F., Saddiqi, O., Hilali, A., Rhinane, H., Baiddar, L., El Arabi, H., & Khanbari, K. (2017). Application of remote sensing in geological mapping, case study Al Maghrabah area - Hajjah region, Yemen. In *ISPRS Annals of the Photogrammetry, Remote Sensing and Spatial Information Sciences* (Vol. 4, pp. 63–71). Copernicus GmbH. <https://doi.org/10.5194/isprs-annals-IV-4-W4-63-2017>
- Almutairi, B., El, A., Belaid, M. A., & Musa, N. (2013). Comparative Study of SAVI and NDVI Vegetation Indices in Sulaibiya Area (Kuwait) Using Worldview Satellite Imagery. *International Journal of Geosciences and Geomatics*, 1(2), 50–53.
- Arribas Cunningham, C. G., Rytuba, J. J., Rye, R. O., Kelly, W. C., Podwyssocki, M. H., McKee, E. H., Tosdal, A. (1995). Geology, geochemistry, fluid inclusion, and isotope geochemistry of the Rodalquilar gold-alunite deposit, Spain. *Economic Geology*, 90–4, 795–, 795–822.
- Average Weather in Almería, Spain, Year Round - Weather Spark. (n.d.). Retrieved May 11, 2020, from <https://weatherspark.com/y/38216/Average-Weather-in-Almeria-Spain-Year-Round#Sections-Clouds>
- Bedini, E., van der Meer, F., & van Ruitenbeek, F. (2009). Use of HyMap imaging spectrometer data to map mineralogy in the Rodalquilar caldera, southeast Spain. *International Journal of Remote Sensing*, 30(2), 327–348. <https://doi.org/10.1080/01431160802282854>
- Berger, M., Moreno, J., Johannessen, J. A., Levelt, P. F., & Hanssen, R. F. (2012). ESA's Sentinel missions in support of Earth system science. *Remote Sensing of Environment*, 120, 84–90. <https://doi.org/10.1016/j.rse.2011.07.023>
- Bhan, S. K., & Krishnanunni, K. (n.d.). Applications of remote sensing techniques to geology. *Proceedings of the Indian Academy of Sciences Section C: Engineering Sciences*, 6(4), 297–311. <https://doi.org/10.1007/bf02881136>
- Bierwirth, P. N. (1990). Mineral mapping and vegetation removal via data-calibrated pixel unmixing, using multispectral images. *International Journal of Remote Sensing*, 11(11), 1999–2017. <https://doi.org/10.1080/01431169008955157>
- Carranza, E. J. M., & Hale, M. (2002). Mineral imaging with Landsat Thematic Mapper data for hydrothermal alteration mapping in heavily vegetated terrain. *International Journal of Remote Sensing*, 23(22), 4827–4852. <https://doi.org/10.1080/01431160110115014>
- Choi, S., Ryu, I. C., Götze, H. J., & Chae, Y. (2017). Spatial distribution of hydrocarbon reservoirs in the West Korea Bay Basin in the northern part of the Yellow Sea, estimated by 3-D gravity forward modeling. *Geophysical Journal International*, 208(1), 75–85. <https://doi.org/10.1093/gji/ggw369>
- Clasen, A., Somers, B., Pipkins, K., Tits, L., Segl, K., Brell, M., ... Förster, M. (2015). Spectral unmixing of forest crown components at close range, airborne and simulated Sentinel-2 and EnMAP spectral imaging scale. *Remote Sensing*, 7(11), 15361–15387. <https://doi.org/10.3390/rs71115361>
- Crippen, R. E., & Blom, R. G. (2001). Unveiling the lithology of vegetated terrains in remotely sensed imagery. *Photogrammetric Engineering and Remote Sensing*, 67(8), 935–943.
- El Campillo De Rodalquilar, Andalucía, Spain Weather Averages | Monthly Average High and Low Temperature | Average Precipitation and Rainfall days | World Weather Online. (n.d.). Retrieved May 11, 2020, from <https://www.worldweatheronline.com/el-campillo-de-rodalquilar-weather-averages/andalucia/es.aspx>
- Fraser, S. J., & Green, A. A. (1987). A software defoliant for geological analysis of band ratios. *International*

- Journal of Remote Sensing*, 8(3), 525–532. <https://doi.org/10.1080/01431168708948659>
- Gascon, F., Bouzinac, C., Thépaut, O., Jung, M., Francesconi, B., Louis, J., ... van der Meer, F. D. (2014). Sentinel-2A MSI and Landsat 8 OLI provide data continuity for geological remote sensing. *Remote Sensing*, 8(11), 10860–10887. <https://doi.org/10.3390/rs8110883>
- Gatti, A., Bertolini, A., & Carriero, F. (2015). *Sentinel-2 Products Specification Document Sentinel-2 Products Specification Document Written by Company Responsibility Date Signature*.
- Ge, W., Cheng, Q., Tang, Y., Jing, L., & Gao, C. (2018). Lithological classification using Sentinel-2A data in the Shibanjing ophiolite complex in Inner Mongolia, China. *Remote Sensing*, 10(4). <https://doi.org/10.3390/rs10040638>
- Google Earth Engine. (n.d.). Retrieved April 21, 2020, from <https://earthengine.google.com/>
- Grebby, S., Cunningham, D., Tansey, K., & Naden, J. (2014). The impact of vegetation on lithological mapping using airborne multispectral data: A case study for the north Troodos region, Cyprus. *Remote Sensing*, 6(11), 10860–10887. <https://doi.org/10.3390/rs61110860>
- Gupta, R. P. (2017). *Remote sensing geology: Third edition. Remote Sensing Geology: Third Edition*. Springer-Verlag Berlin Heidelberg. <https://doi.org/10.1007/978-3-662-55876-8>
- Haest, M., Cudahy, T., Rodger, A., Laukamp, C., Martens, E., & Caccetta, M. (2013). Unmixing the effects of vegetation in airborne hyperspectral mineral maps over the Rocklea Dome iron-rich palaeochannel system (Western Australia). *Remote Sensing of Environment*, 129, 17–31. <https://doi.org/10.1016/j.rse.2012.10.011>
- Hewson, R., & Cudahy, T. (2011). Land Remote Sensing and Global Environmental Change: NASA's Earth Observing System and the Science of ASTER and MODIS, 894. <https://doi.org/10.1007/978-1-4419-6749-7>
- Hideki Kobayashi. (2018). Geospatial Data Analysis on Google Earth Engine. *Journal of The Remote Sensing Society of Japan*, 38(2), 125–130. <https://doi.org/10.11440/rssj.38.125>
- Huang, C., Zhang, C., He, Y., Liu, Q., Li, H., Su, F., ... Bridhikitti, A. (2020). Land Cover Mapping in Cloud-Prone Tropical Areas Using Sentinel-2 Data: Integrating Spectral Features with Ndvi Temporal Dynamics. *Remote Sensing*, 12(7), 1163. <https://doi.org/10.3390/RS12071163>
- Huete, A. R. (1988). A soil-adjusted vegetation index (SAVI). *Remote Sensing of Environment*, 25(3), 295–309. [https://doi.org/10.1016/0034-4257\(88\)90106-X](https://doi.org/10.1016/0034-4257(88)90106-X)
- Imbroane, A., Melenti, C., & Gorgan, D. (2007). Mineral explorations by Landsat image ratios. *Proceedings - 9th International Symposium on Symbolic and Numeric Algorithms for Scientific Computing, SYNASC 2007*, (September), 335–340. <https://doi.org/10.1109/SYNASC.2007.52>
- Li, M., Zhou, X., Gammons, C. H., Khalil, M., & Speece, M. (2018). Aeromagnetic and spectral expressions of rare earth element deposits in the Gallinas Mountains area, Central New Mexico, USA. *Interpretation*, 6(4), T937–T949. <https://doi.org/10.1190/int-2017-0199.1>
- Mašková, Z., Zemek, F., & Květ, J. (2008). Normalized difference vegetation index (NDVI) in the management of mountain meadows. *Boreal Environment Research*, 13(5), 417–432.
- Meyer, L. H., Heurich, M., Beudert, B., Premier, J., & Pflugmacher, D. (2019). Comparison of Landsat-8 and Sentinel-2 data for estimation of leaf area index in temperate forests. *Remote Sensing*, 11(10), 1–16. <https://doi.org/10.3390/rs11101160>
- Moik, J. G. (1980). *Digital Processing of Remotely Sensed Images*. NASA SP-431.
- Mueller, A. (2019). Copernicus Hyperspectral Imaging Mission Requirements Document, 2019.
- Murphy, R. J., & Wadge, G. (1994). The effects of vegetation on the ability to map soils using imaging spectrometer data. *International Journal of Remote Sensing*, 15(1), 63–86. <https://doi.org/10.1080/01431169408954051>
- Mutanga, O., & Kumar, L. (2019). *Google earth engine applications. Remote Sensing* (Vol. 11). <https://doi.org/10.3390/rs11050591>
- Nasuti, C., & Carriero, F. (2015). *Sentinel-2 Products Specification Document Sentinel-2*. European Space Agency (ESA). https://sentinel.esa.int/documents/247904/349490/S2_MSI_Product_Specification.pdf
- Oikonomidis, D., & Mouratidis, A. (2009). Geological mapping by the use of multispectral and multitemporal satellite images, compared with GIS geological data. Case studies from the Macedonia area, Northern Greece, (July 2015). <https://doi.org/10.3233/978-1-60750-494-8-311311>
- Padmanaban, R., Bhowmik, A., & Cabral, P. (2017). A Remote Sensing Approach to Environmental Monitoring in a Reclaimed Mine Area. *ISPRS International Journal of Geo-Information*, 6(12), 401. <https://doi.org/10.3390/ijgi6120401>
- Pearlman, J. S., Barry, P. S., Segal, C. C., Shepanski, J., Beiso, D., & Carman, S. L. (2003). Hyperion, a space-based imaging spectrometer. *IEEE Transactions on Geoscience and Remote Sensing*, 41(6 PART I),

- 1160–1173. <https://doi.org/10.1109/TGRS.2003.815018>
- Porwal, A., & González-Álvarez, I. (2019). Introduction to special issue on geologic remote sensing. *Ore Geology Reviews*, 108(December), 1–7. <https://doi.org/10.1016/j.oregeorev.2019.05.004>
- Qi, J., Chehbouni, A., Huete, A. R., Kerr, Y. H. & Sorooshian, S. (1994). A modified soil adjusted vegetation index. *Remote Sensing of Environment*, 48(2), 119–126. [https://doi.org/10.1016/0034-4257\(94\)90134-1](https://doi.org/10.1016/0034-4257(94)90134-1)
- Resampling and Reducing Resolution | Google Earth Engine. (n.d.). Retrieved April 4, 2020, from <https://developers.google.com/earth-engine/resample>
- Rodger, A., & Cudahy, T. (2009). Vegetation corrected continuum depths at 2.20 μm : An approach for hyperspectral sensors. *Remote Sensing of Environment*, 113(10), 2243–2257. <https://doi.org/10.1016/j.rse.2009.06.011>
- Rowan, L. C., Mars, J. C., & Simpson, C. J. (2005). Lithologic mapping of the Mordor, NT, Australia ultramafic complex by using the Advanced Spaceborne Thermal Emission and Reflection Radiometer (ASTER). *Remote Sensing of Environment*, 99(1–2), 105–126. <https://doi.org/10.1016/j.rse.2004.11.021>
- Rytuba, J. J., Arribas, A., Jr., Cunningham, C. G., McKee, E. H., Podwysocki, M.H., Smith, J. G., Kelly, W. C., Arribas, A., 1990, Mineralized and unmineralized calderas in Spain; Part II, evolution of the Rodalquilar caldera complex and associated gold-alunite deposits. *Mineralium Deposita*, 25(1), S29–S35. <https://doi.org/10.1007/BF00205247>
- Sentinel-Hub (2020). SAVI (Soil Adjusted Vegetation Index) | Sentinel-Hub custom scripts. Retrieved June 12, 2020, from <https://custom-scripts.sentinel-hub.com/custom-scripts/sentinel-2/savi/#>
- ESA (2019). Sen2Cor | STEP. (2019). Retrieved October 24, 2019, from <http://step.esa.int/main/third-party-plugins-2/sen2cor/>
- Shahriari, H., Honarmand, M., & Ranjbar, H. (2015). Comparison of multi-temporal ASTER images for hydrothermal alteration mapping using a fractal-aided SAM method. *International Journal of Remote Sensing*, 36(5), 1271–1289. <https://doi.org/10.1080/01431161.2015.1011352>
- Sibanda, M., Mutanga, O., & Rouget, M. (2015). Examining the potential of Sentinel-2 MSI spectral resolution in quantifying above ground biomass across different fertilizer treatments. *ISPRS Journal of Photogrammetry and Remote Sensing*, 110(March 2018), 55–65. <https://doi.org/10.1016/j.isprsjprs.2015.10.005>
- Siegal, B. S., & Goetz, A. F. H. (1977). Effect of Vegetation on Rock and Soil Type Discrimination. *Photogrammetric Engineering and Remote Sensing*, 43(2), 191–196.
- Smith, W., Succession, F., & Darwin, C. (2007). Chapter 4 Major geological events fit into a timeline, beginning with the formation of the Earth.
- Traore, M., Çan, T., & N, S. T. E. K. İ. (2018). Use of remote sensing for mineral exploration, impact of vegetation cover on the Landsat 8 image : Case of the Southern part of Central African Republic, (Lillesand 2004), 2018.
- Van der Meer, F. D., van der Werff, H. M. A., & van Ruitenbeek, F. J. A. (2014). Potential of ESA's Sentinel-2 for geological applications. *Remote Sensing of Environment*, 148, 124–133. <https://doi.org/10.1016/j.rse.2014.03.022>
- Van der Meer, Freek D., van der Werff, H. M. A., van Ruitenbeek, F. J. A., Hecker, C. A., Bakker, W. H., Noomen, M. F., van der Meijde, M., Carranza, E. J. M., de Smeth, B. J., Woldai, T. (2012). Multi- and hyperspectral geologic remote sensing: A review. *International Journal of Applied Earth Observation and Geoinformation*, 14(1), 112–128. <https://doi.org/10.1016/j.jag.2011.08.002>
- Van der Werff, H., Hewson, R., & Van Der Meer, F. (2018a). Use what is there: What can sentinel-2 do for geological remote sensing? *International Geoscience and Remote Sensing Symposium (IGARSS), 2018-July*, 8359–8362. <https://doi.org/10.1109/IGARSS.2018.8519080>
- Van der Werff, H., & van der Meer, F. (2015). Sentinel-2 for mapping iron absorption feature parameters. *Remote Sensing*, 7(10), 12635–12653. <https://doi.org/10.3390/rs71012635>
- Van der Werff, H., & van der Meer, F. (2016). Sentinel-2A MSI and Landsat 8 OLI provide data continuity for geological remote sensing. *Remote Sensing*, 8(11). <https://doi.org/10.3390/rs8110883>
- Weier, J., and Herring, D. (2000, August 30). Measuring Vegetation (NDVI & EVI). Retrieved October 27, 2019, from <https://earthobservatory.nasa.gov/features/MeasuringVegetation>
- Wu, C., Li, X., Chen, W., & Li, X. (2018). A Review of Geological Applications of High-spatial- resolution Remote Sensing Data (November). <https://doi.org/10.20944/preprints201811.0162.v1>
- Yamaguchi, Y., Kahle, A. B., Tsu, H., Kawakami, T., & Pniel, M. (1998). Overview of advanced spaceborne thermal emission and reflection radiometer (ASTER). *IEEE Transactions on Geoscience and*

Remote Sensing, 36(4), 1062–1071. <https://doi.org/10.1109/36.700991>
Ye, Z. X., Cheng, W. M., Zhao, Z. Q., Guo, J. Y., Ding, H., & Wang, N. (2019). Interannual and seasonal vegetation changes and influencing factors in the extra-high mountainous areas of southern Tibet. *Remote Sensing*, 11(11), 1–20. <https://doi.org/10.3390/rs11111392>

7. APPENDIX

7.1. Dataset

Number	Day	Date	Image ID
1	1	01 Jan 2019	COPERNICUS/S2_SR/20190101T105439_20190101T105645_T30SWF
2	6	06 Jan 2019	COPERNICUS/S2_SR/20190106T105431_20190106T105433_T30SWF
3	11	11 Jan 2019	COPERNICUS/S2_SR/20190111T105419_20190111T105807_T30SWF
4	21	21 Jan 2019	COPERNICUS/S2_SR/20190121T105349_20190121T105535_T30SWF
5	26	26 Jan 2019	COPERNICUS/S2_SR/20190126T105321_20190126T105420_T30SWF
6	36	05 Feb 2019	COPERNICUS/S2_SR/20190205T105231_20190205T105330_T30SWF
7	51	20 Feb 2019	COPERNICUS/S2_SR/20190220T105059_20190220T110016_T30SWF
8	56	25 Feb 2019	COPERNICUS/S2_SR/20190225T105021_20190225T105315_T30SWF
9	71	12 March 2019	COPERNICUS/S2_SR/20190312T105119_20190312T105121_T30SWF
10	76	17 March 2019	COPERNICUS/S2_SR/20190317T105021_20190317T105035_T30SWF
11	96	06 April 2019	COPERNICUS/S2_SR/20190406T105031_20190406T110005_T30SWF
12	101	11 April 2019	COPERNICUS/S2_SR/20190411T105029_20190411T105100_T30SWF
13	106	16 April 2019	COPERNICUS/S2_SR/20190416T105031_20190416T105927_T30SWF
14	116	26 April 2019	COPERNICUS/S2_SR/20190426T105031_20190426T105613_T30SWF
15	131	11 May 2019	COPERNICUS/S2_SR/20190511T105039_20190511T105205_T30SWF
16	136	16 May 2019	COPERNICUS/S2_SR/20190516T105031_20190516T105030_T30SWF
17	146	26 May 2019	COPERNICUS/S2_SR/20190526T105031_20190526T105519_T30SWF
18	161	10 June 2019	COPERNICUS/S2_SR/20190610T105039_20190610T105331_T30SWF
19	171	20 June 2019	COPERNICUS/S2_SR/20190620T105039_20190620T105906_T30SWF
20	176	25 June 2019	COPERNICUS/S2_SR/20190625T105031_20190625T105346_T30SWF
21	191	10 July 2019	COPERNICUS/S2_SR/20190710T105039_20190710T105335_T30SWF
22	196	15 July 2019	COPERNICUS/S2_SR/20190715T105031_20190715T110027_T30SWF
23	201	20 July 2019	COPERNICUS/S2_SR/20190720T105039_20190720T105755_T30SWF
24	206	25 July 2019	COPERNICUS/S2_SR/20190725T105031_20190725T105702_T30SWF
25	211	30 July 2019	COPERNICUS/S2_SR/20190730T105039_20190730T105502_T30SWF
26	216	04 August 2019	COPERNICUS/S2_SR/20190804T105031_20190804T105722_T30SWF
27	221	09 August 2019	COPERNICUS/S2_SR/20190809T105039_20190809T105327_T30SWF
28	226	14 August 2019	COPERNICUS/S2_SR/20190814T105031_20190814T110022_T30SWF
29	231	19 August 2019	COPERNICUS/S2_SR/20190819T105029_20190819T105901_T30SWF
30	236	24 August 2019	COPERNICUS/S2_SR/20190824T105031_20190824T105344_T30SWF
31	261	18 Sept 2019	COPERNICUS/S2_SR/20190918T105029_20190918T110002_T30SWF
32	271	28 Sept 2019	COPERNICUS/S2_SR/20190928T105029_20190928T105421_T30SWF
33	286	13 Oct 2019	COPERNICUS/S2_SR/20191013T105031_20191013T105439_T30SWF
34	311	07 Nov 2019	COPERNICUS/S2_SR/20191107T105139_20191107T105655_T30SWF
35	316	12 Nov 2019	COPERNICUS/S2_SR/20191112T105301_20191112T105437_T30SWF
36	331	27 Nov 2019	COPERNICUS/S2_SR/20191127T105309_20191127T105433_T30SWF
37	356	22 Dec 2019	COPERNICUS/S2_SR/20191222T105441_20191222T105443_T30SWF
38	366	01 Jan 2020	COPERNICUS/S2_SR/20200101T105441_20200101T105437_T30SWF
39	381	16 Jan 2020	COPERNICUS/S2_SR/20200116T105309_20200116T105941_T30SWF
40	381	26 Jan 2020	COPERNICUS/S2_SR/20200126T105229_20200126T105911_T30SWF

Table 7.1: Image Collection used in this research. Dates and Image ids of images used in this research.

7.2. Pixel Selection

Table 7.2: List of all the selected pixels with the annual band ratio statistical values.

Name	NDVI Mean	NDVI Std Dev	SAVI Mean	SAVI Std Dev	GBR 1 Mean	GMR 1 Std Dev	GBR 2 Mean	GBR 2 Std Dev
GO 1	0.040	0.02	0.033	0.017	1.81	0.14	1.60	0.09
GO 2	-0.0012	0.022	-0.0009	0.018	1.818	0.12	1.63	0.098
GO 3	-0.0085	0.019	-0.0069	0.016	1.785	0.123	1.63	0.104
GO 4	0.141	0.06	0.120	0.054	1.84	0.206	1.43	0.08
GO 5	0.024	0.019	0.020	0.0158	1.7	0.135	1.5	0.10
GO 6	0.1	0.066	0.08	0.57	2.07	0.33	1.57	0.093
GO 7	0.071	0.044	0.059	0.037	3.00	3.65	1.78	0.22
GO 8	0.049	0.37	0.04	0.03	2.41	0.727	1.78	0.22
GO 9	0.077	0.0344	0.065	0.029	2.15	0.232	1.6	0.098
GO 10	0.078	0.034	0.0659	0.029	2.32	0.299	1.64	0.1124
GO 11	0.078	0.027	0.0658	0.023	2.25	0.270	1.60	0.084
GO 12	0.053	0.0146	0.044	0.0122	2.06	0.23	1.69	0.129
GO 13	0.076	0.029	0.064	0.0244	1.64	0.054	1.244	0.047
GO 14	0.14	0.0708	0.11	0.0624	1.833	0.204	1.55	0.099
GO 15	0.1379	0.06	0.1169	0.0526	2.003	0.462	1.584	0.106
GO 16	0.110	0.037	0.092	0.032	2.07	0.259	1.615	0.118
GO 17	0.155	0.043	0.1320	0.037	1.55	0.0863	1.31	0.057
GO 18	0.159	0.0618	0.136	0.0541	2.06	0.33	1.48	0.09
GO 19	0.11	0.044	0.095	0.038	1.83	0.17	1.529	0.09
GO 20	0.060	0.020	0.050	0.017	2.21	0.25	1.61	0.0944

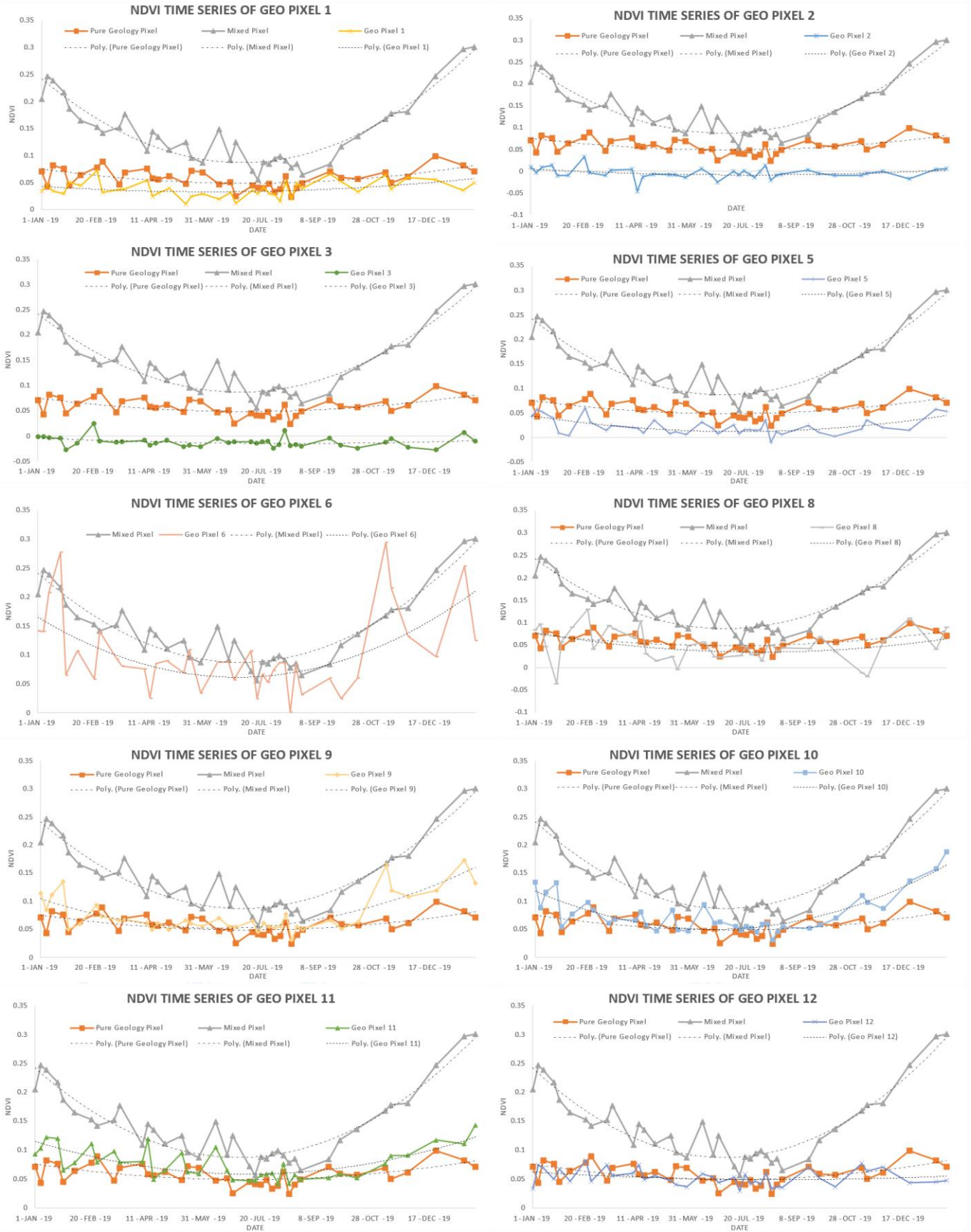


Figure 7.1: NDVI time-series charts of the selected pixels along with the reference pixels. The charts show a comparison with the time-series of the reference pixels. The orange curve (with data points as squares) show the variation of NDVI for a pure geological pixel and the grey curve (with triangles as data points) show the variations of NDVI for a mixed pixel.

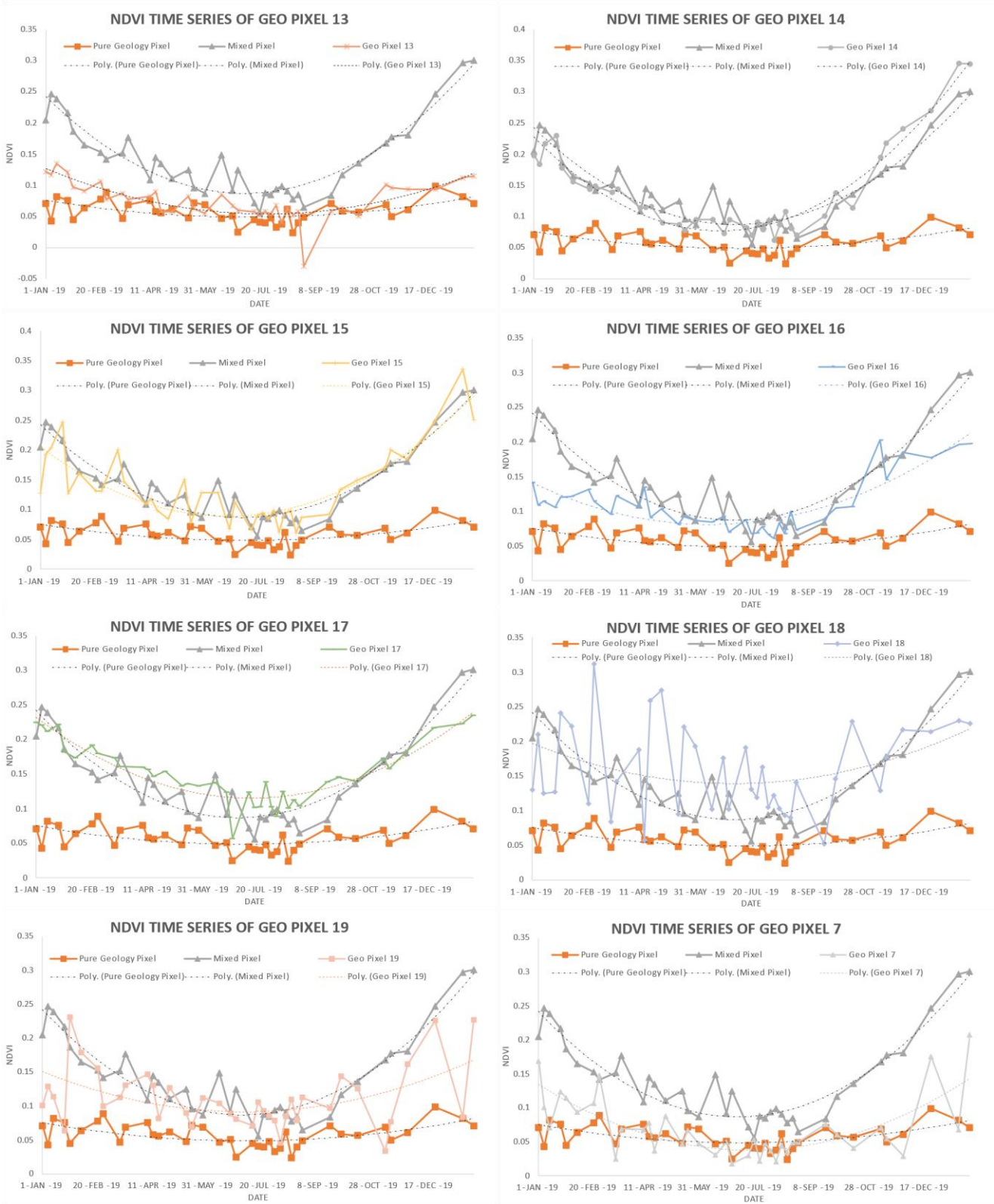


Figure 7.2: NDVI time-series charts of the selected pixels along with the reference pixels (continued). The charts show a comparison with the time series of the reference pixels. The orange curve (with data points as squares) show the variation of NDVI for a pure geological pixel and the grey curve (with triangles as data points) show the variations of NDVI for a mixed pixel.

7.3. Time Series

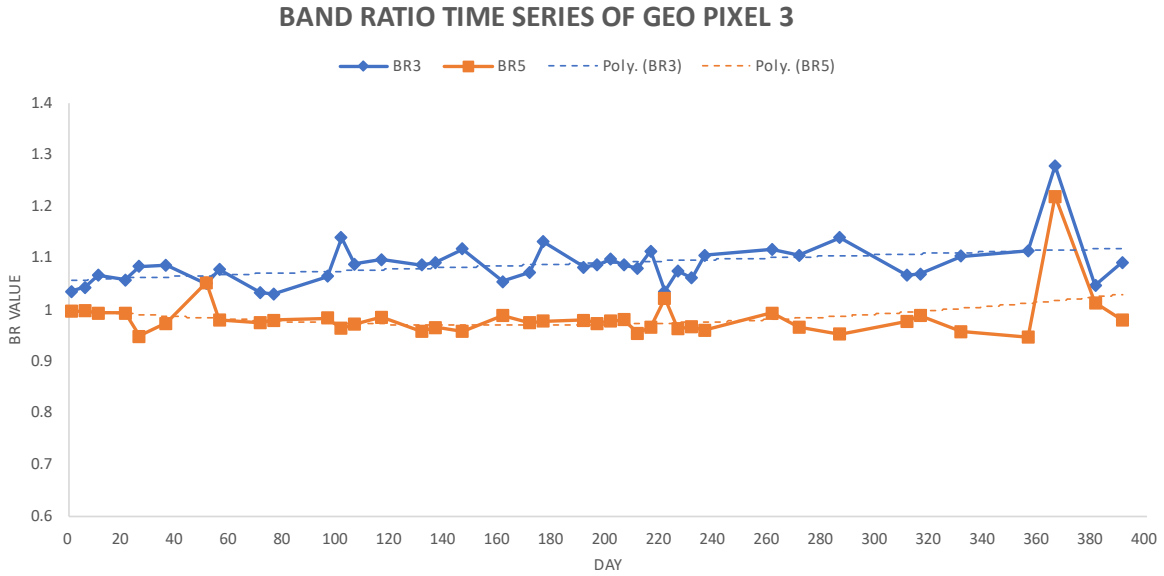


Figure 7.3: Time Series of band ratios from January 2019 to January 2020 (Day 1 to Day 391) of geo pixel 3. BR3 (B7/B8) shows the variation of the absorption feature at 835nm (see figure 11) and BR5 (B8/B4) shows the variation of vegetation in the pixel. Blue curve (with diamonds as datapoints) is time series of BR3 and orange curve (with squares as datapoints) is time series of BR5. BR value stands of band ratio value.

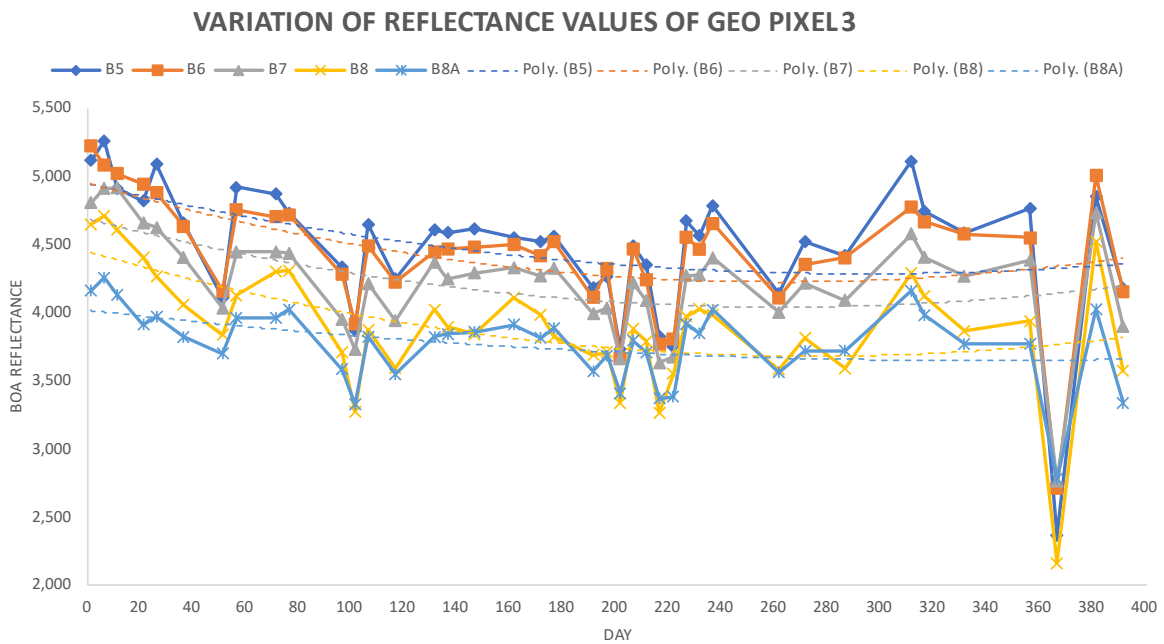


Figure 7.4: Variation of Bottom of Atmosphere Reflectance values of vegetation pixel 3 from bands 5, 6, 7, 8 and 8A. All 40 images were used. Outliers (some of the troughs) are due to cloudy images (February 20th, 2019 – day 51, June25th 2019 – day 176, and, January 1st, 2020 – day 366).

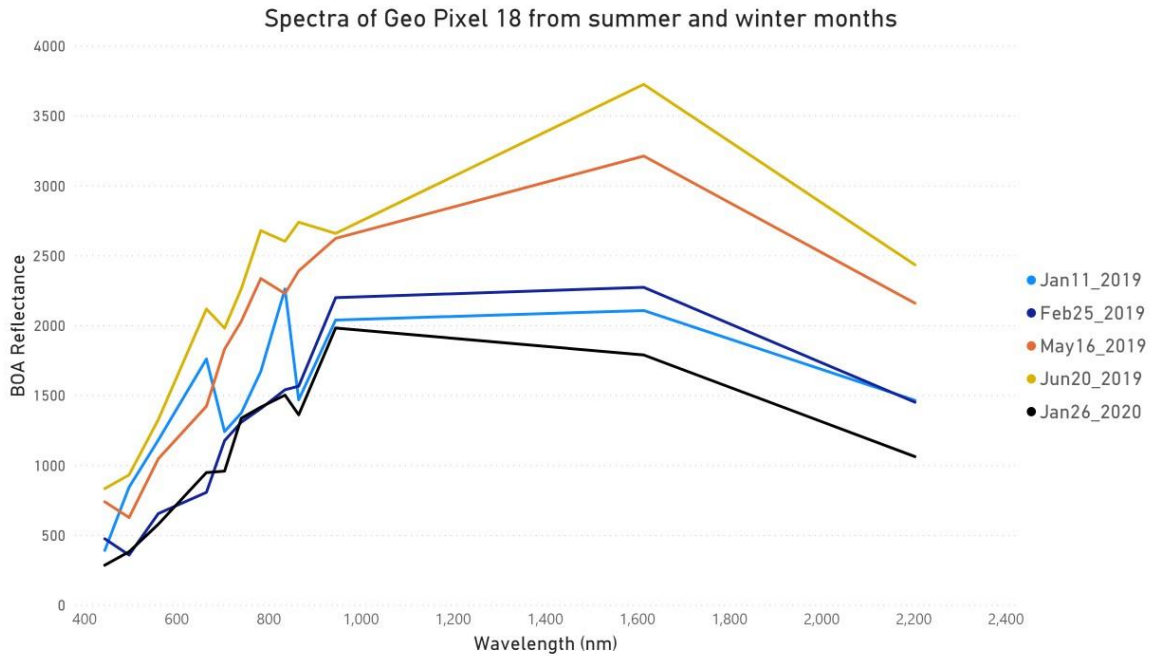


Figure 7.5: Spectra extracted from geo pixel 18. Orange and red (top two) are from summer months while blue, violet, and black (bottom three) are from winter months. All images were cloud free.

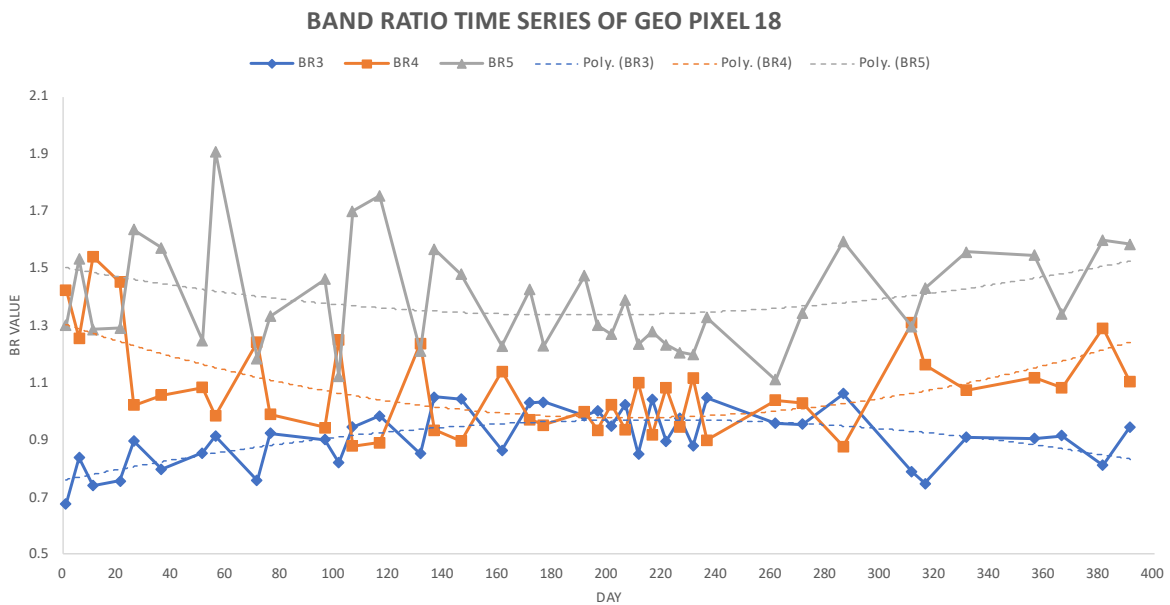


Figure 7.6: Time Series of band ratios from January 2019 to January 2020 (Day 1 to Day 391) of geo pixel 18. BR3 (B7/B8) shows the variation of the absorption feature at 835nm (see figure 18) and BR4 (B8/B8A) shows the variation of the absorption feature at 864nm. Blue curve (with diamond as datapoints) is time series of BR3, orange curve (with squares as datapoints) is time series of BR4 and silver curve (with triangles as datapoints) is the time series of BR5 (B8/B4). BR value stands of band ratio value.

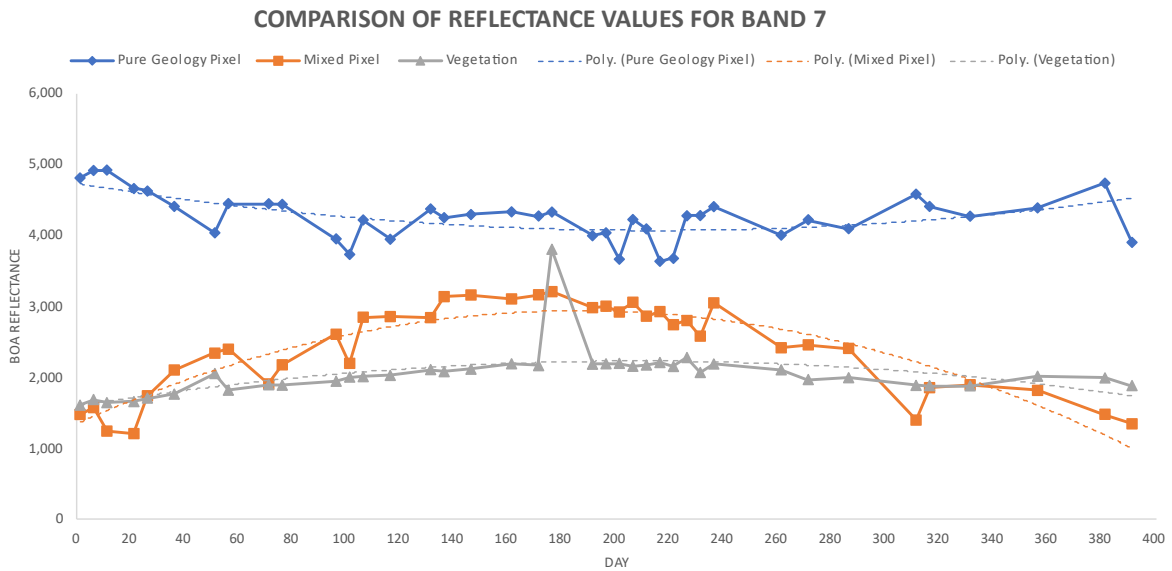


Figure 7.7: Time Series comparison of band 7 reflectance values for pure geology (geo pixel 3), mixed (geo pixel 7) and vegetation pixels. Blue curve (with diamonds as datapoints) is the variation of B7 reflectance values of the pure geology pixel, orange curve (with squares as datapoints) is for the mixed pixel, and silver curve (with triangles as datapoints) is for vegetation pixel. Outlier due to cloud cover was removed (day 366, January 1st, 2020) to compare the trends.

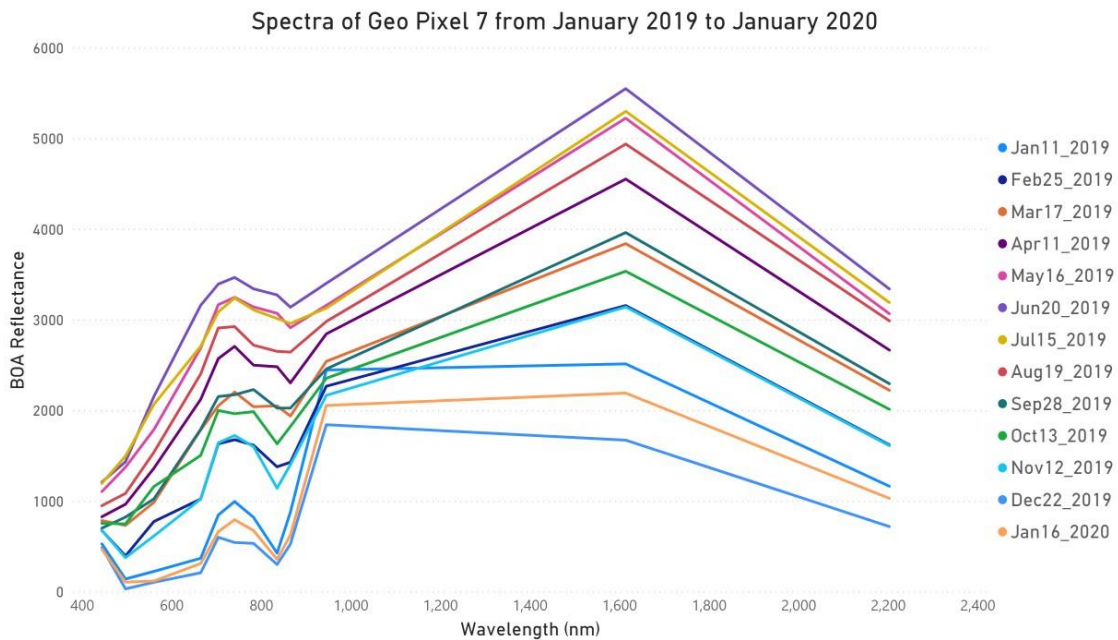


Figure 7.8: Time series of spectra from Geo Pixel 7. A representative spectra was chosen from each month from January 2019 to January 2020. All images were cloud free. Seasonal variation in spectra can be seen in the figure. The spectra clusters into three groups with summer months towards the top, winter months towards the bottom and spring and autumn months in between. The depth of the feature at 835nm also seems to be varying in the three clusters.

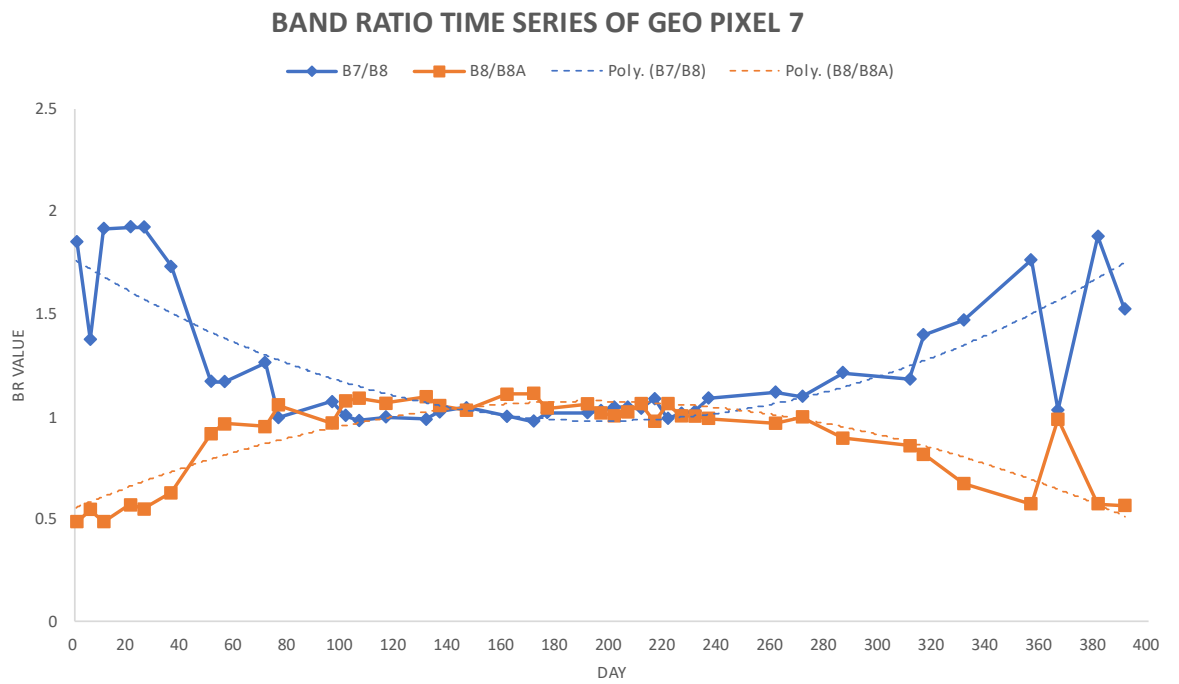


Figure 7.9: Time Series of band ratios from January 2019 to January 2020 (Day 1 to Day 391) of geo pixel 7. BR3 (B7/B8) shows the variation of the absorption feature at 835nm (see figure 13) and BR4 (B8/B8A) shows the variation of the absorption feature at 864nm. Blue curve (with diamonds as datapoints) is time series of BR3 and orange curve (with squares as datapoints) is time series of BR4. BR value stands of band ratio value.

7.4. Scripts

This section contains parts of the scripts used in this research. Since the complete scripts are very long, only the main parts will be displayed. During this research, tools to extract spectra from images from specific pixels, compute band ratios for an image collection, compute statistics of band ratio variations over time, create a time series of band ratios (and individual bands) from specific pixels, extract spectra from a pixel over time, create a visualization to observe changes over time as time lapses, export data, and products, etc., were produced.

7.4.1. Image filtering & Selection

As mentioned in data preparation, images were filtered for cloud cover. The following part of the code shows the process of filtering the images. A date filter was created for each month and then combined into one. Variables for each month were defined because they were used to control images with clouds. In cases where images turned out to be cloudy (in the study area), dates could be adjusted manually to remove such images, instead of altering the cloud cover percentage value.

```
// sent2 is the Image Collection ("COPERNICUS/S2_SR")
//Creating variables for dates to be used in filtering the image collection;
var jan_date_2019 = ee.Filter.date('2019-01-01', '2019-01-31');
var feb_date_2019 = ee.Filter.date('2019-02-01', '2019-02-28');
var mar_date_2019 = ee.Filter.date('2019-03-01', '2019-03-31');
var apr_date_2019 = ee.Filter.date('2019-04-01', '2019-04-30');
var may_date_2019 = ee.Filter.date('2019-05-01', '2019-05-31');
var jun_date_2019 = ee.Filter.date('2019-06-01', '2019-06-30');
var jul_date_2019 = ee.Filter.date('2019-07-01', '2019-07-31');
var aug_date_2019 = ee.Filter.date('2019-08-01', '2019-08-31');
var sept_date_2019 = ee.Filter.date('2019-09-01', '2019-09-30');
var oct_date_2019 = ee.Filter.date('2019-10-01', '2019-10-31');
var nov_date_2019 = ee.Filter.date('2019-11-01', '2019-11-30');
var dec_date_2019 = ee.Filter.date('2019-12-01', '2019-12-31');
var jan_date_2020 = ee.Filter.date('2020-01-01', '2020-01-31');
//defining the date filter; from Jan 2019 to Jan 2020
var datefilter
=ee.Filter.or(jan_date_2019,feb_date_2019,mar_date_2019,apr_date_2019,may_date_2019,jun_date_2019,jul_date_2019,
aug_date_2019,sept_date_2019,oct_date_2019, nov_date_2019, dec_date_2019,jan_date_2020);
//filtering and printing the image collection
var img2019 =
sent2.filter(datefilter).filterBounds(studyarea).filter(ee.Filter.lt('CLOUD_COVERAGE_ASSESSMENT',10));
print(img2019); //returns 40 images (list of these images with Image IDs and dates mentioned in table 7.1
```

7.4.2. Extracting Spectra

To extract spectra, each image was defined as a separate variable, after which they were subset spatially and spectrally. The band numbers were converted into wavelength values, and then the spectral plot was created for all the required pixels. The following code is an example that shows the extraction of spectra from three pixels from the 1st January 2019 image. This piece of script is from the code, which extracts spectra from more than 20 pixels from all the 40 images.

```
// sent2 is the Image Collection ("COPERNICUS/S2_SR")
//1st Image 01-01-19
var jan19_01 = ee.Image("COPERNICUS/S2_SR/20190101T105439_20190101T105645_T30SWF");
//Clipping it to study area
var cjan19_01 = jan19_01.clip(rodalquilar); //rodalquilar is a polygon which covers the extent of the required study area
//Spectrally subsetting the image
var scjan19_01 = cjan19_01.select('B1','B2','B3','B4','B5','B6','B7','B8','B8A','B9','B11','B12');
Map.addLayer(scjan19_01, {bands: ["B4", "B3", "B2"], min:0, max:3000},"True Color Composite Jan 1st 2019");
// Define a list of Sentinel 2 wavelengths for X-axis labels.
var wavelengths = [443.9, 496.6, 560, 664.5, 703.9, 740.2, 782.5, 835.1, 864.8, 945, 1613.7, 2202.4];
//Defining plot options
var plotOptions = {
  title: 'Sentinel-2 Surface reflectance spectra for 1st Jan 2019 Image',
  hAxis: {title: 'Wavelength in Nanometers'},
  vAxis: {title: 'Reflectance'},
  lineWidth: 1,
  pointSize: 4,
  series: {
    1: {color: 'blue'}, 0: {color: 'green'}, 2: {color: 'yellow'}, 3: {color: 'red'}, 4: {color: 'Black'}
  }
};
//Creating an array of pixels
var samples = ee.FeatureCollection([vegetation, Outcrop, Water]);
// Create the chart and set options.
var Chart1 = ui.Chart.image.regions(
  scjan19_01, samples, ee.Reducer.mean(),
  10 //10 m is the spatial resolution,
  'label',wavelengths)
  .setChartType('ScatterChart')
  .setOptions(plotOptions);
// Display the chart.
print(Chart1,"01 Jan 2019"); //the printed chart was downloaded as a CSV file. For time series on spectra, similar code
was used with all the required pixels as samples with 40 images. 40 charts (one for each image) were created with spectra
from required pixels.
```

7.4.3. Band ratios and band ratio statistics

Six band ratios were defined as mentioned in table 2.2. The following script shows the functions used to compute the band ratios. Band ratio statistics of NDVI are shown, similar scripts were used to compute the statistics of other band ratios.

```
// Function to calculate and add an NDVI band
var addNDVI = function(image) {
return image.addBands(image.normalizedDifference(['B8', 'B4']));
};
// Add NDVI band to image collection
var img2019 = img2019.map(addNDVI);
print(img2019,"NDVI added");
//Computing and adding SAVI to image collection
// SAVI = (800nm - 670nm) / (800nm + 670nm + L) * (1 + L)
// where L = soil brightness = 0.5 (as per definition but 0.428 for Sentinel 2 according to ESA)
var addSAVI = function(a){
var L = 0.428;
return a.addBands((a.select("B8").subtract(a.select("B4"))).divide(a.select("B8").add(((a.select("B4")).add(L)).multiply(1.0 + L))).rename('savi'))
};
var img2019 = img2019.map(addSAVI);
print(img2019, "SAVI added");
//Function to calculate and add ironoxide BR as a band, BR1
var addironoxide = function(a) {
return a.addBands(a.select("B4").divide(a.select("B2")).rename('io'));
};
//Adding iron oxide band to all the images in the image collection - img2019
var img2019 = img2019.map(addironoxide);

//Function to calculate Laterite Band Ratio, BR2
var addlaterite = function(a){
return a.addBands(a.select("B4").multiply(a.select("B11").divide(a.select("B12").multiply(a.select("B4")))).rename("lat"));
};
//Adding the laterite band ratio to all the images in the image collection img2019 as a band
var img2019 = img2019.map(addlaterite);
print(img2019, "laterite added");
```

```

//Defining BR3 (B7/B8)
var addbr3 = function(a){
  return a.addBands(a.select("B4").multiply(a.select("B7").divide(a.select("B8").multiply(a.select("B4")))).rename("br3"));
};
//Adding BR3 to all the images in the image collection img2019 as a band
var img2019 = img2019.map(addbr3);
print(img2019, "br3 added");
//Defining and adding BR4 (B8/B8A) to all the images in the image collection img2019 as a band
var addbr4 = function(a){
  return a.addBands(a.select("B4").multiply(a.select("B8").divide(a.select("B8A").multiply(a.select("B4")))).rename("br4"));
};
var img2019 = img2019.map(addbr4);
//Defining and adding BR5 (B8/B4) to all the images in the image collection img2019 as a band
var addbr5 = function(a){
  return a.addBands(a.select("B4").multiply(a.select("B8").divide(a.select("B4").multiply(a.select("B4")))).rename("br5"));
};
var img2019 = img2019.map(addbr5);

//Calculating the mean of value for each pixel for the complete image collection
var ndvi2019 = img2019.select("nd")
var meannndvi = ndvi2019.reduce(ee.Reducer.mean());
//Clipping the NDVI statistics image
var meannndvi = meannndvi.clip(rodalquilar);
//Adding the NDVI statistics image
Map.addLayer(meannndvi, {min:-1,max:1}, 'Mean NDVI');

//Calculating the standard deviation of value for each pixel for the complete image collection
var std = ndvi2019.reduce(ee.Reducer.stdDev());
var std = std.clip(rodalquilar);
Map.addLayer(std, {min:0, max:1}, "Standard Deviation NDVI 2019");
//Similarly the band ratio image statistics were also computed for the other band ratios. The inspector tool in GEE was used to get values of certain pixels.

```

7.4.4. Band ratio time-series charts

The following is an example of the script created to produce band ratio time-series charts. The example produces the NDVI time-series chart of pixels Geo Pixels 1, 2, 3, 4, and 5. Similar to the example, time-series charts were produced for other band ratios and other pixels. Time-series of individual bands can also be produced using the same code by replacing 'nd' with 'band number.'

```
//timeseries of Band Ratios
var samples = ee.FeatureCollection([go1, go2, go3, go4, go5]); //collection of required pixels
var plotOptions = {
  title: 'NDVI Time Series',
  hAxis: {title: 'Date'},
  vAxis: {title: 'NDVI'},
  lineWidth: 1,
  pointSize: 4,
  series: {
    1: {color: 'blue'},
    0: {color: 'green'},
    2: {color: 'yellow'},
    3: {color: 'red'},
    4: {color: 'Black'}
  }
};
//Creating the NDVI time series chart
var plotNDVI = ui.Chart.image.seriesByRegion(img2019, samples, ee.Reducer.mean(), 'nd')
  .setChartType('LineChart').setOptions(plotOptions);
//plotting the NDVI time series chart
print(plotNDVI, "Ndvi");
//Similarly, timeseries charts were produced for other band ratios and other pixels. Time-series of individual bands can
also be produced using the same code by replacing 'nd' with 'band number'.
```

7.4.5. Time-lapse visualizations

The following code creates a time-lapse of true-color composites of all the images in the image collection spatially subset to the study area.

```
//Creating time lapse visualisations of true color composites.  
  
var collection = img2019 // Need to have 3-band imagery for the video.  
  .select(['B4', 'B3', 'B2'])  
  .map(function(image) {  
    return image.visualize({bands:['B4','B3','B2'],min:0, max:3000});  
  });  
  
//Exporting time lapse video, rodalquilar polygon was used as region, the function clips the video to this polygon  
  
Export.video.toDrive({collection: collection, description: 'time_lapse_truecolor_composites', dimensions: 1080,  
framesPerSecond: 1,region: rodalquilar});
```

7.4.6. 3-D Spectra

As mentioned in section 2.6, 3-D spectra were used in data exploration. For creating 3-D spectra, python was used. The spectra were extracted using the scripts mentioned above from GEE and converted into an excel file. The excel file was then imported into python, and 3-D surface curves were produced using the following script.

```
import matplotlib
import pandas as pd
import numpy as np
import copy

#importing excel file with spectra from all months from Geo Pixel 1
df = pd.read_excel('GeoPixel1.xlsx')
print(df)

from mpl_toolkits.mplot3d import Axes3D
import matplotlib.pyplot as plt

month_ticks = copy.deepcopy(df.axes[1][1:].values)

x = np.array([])
y = np.array([])
z = np.array([])
for i in range(len(df.axes[1])-1):
    x = np.append(x, df[df.axes[1][0]].values)
    y = np.append(y, np.full((1,len(df.axes[0])), i+1)[0])
    z = np.append(z, df[df.axes[1][i+1]].values)

print(len(x), len(y), len(z))
fig = plt.figure(figsize=(20,20))
ax = fig.gca(projection='3d')

ax.plot_trisurf(x, y, z, linewidth=0.2, antialiased=True)
ax.set_xlabel('Wavelength',labelpad=10)
ax.set_xlim3d(0, 2500)
ax.set_ylabel('Image Number',labelpad=10)
ax.set_ylim3d(-1, 41) #yaxis start and end
plt.yticks(np.arange(1, 41, 3)) #spacing b/w ticks
#ax.set_yticklabels(list(month_ticks)) #names
ax.set_zlabel('BOA Reflectance',labelpad=10)

plt.show() #prints a 3D surface curve with date of the image as z axis.
```